# Measuring Inflation with CLASS

by

Dominik Gothe

A dissertation submitted to Johns Hopkins University in conformity with the requirements

for the degree of Doctor of Philosophy.

July 2015

Baltimore, Maryland

Abstract

Using the Cosmology Large Angular Scale Surveyor (CLASS), we will measure the polarization of the Cosmic Microwave Background (CMB) to constrain inflationary theory. The gravitational waves generated during the inflationary epoch imprinted specific polarization patterns – quantifiable by tensor-to-scalar ratio $r$ – onto the CMB, which CLASS is designed to detect. Furthermore, we will be able to make assertions about the energy scale during inflation by discovering the features of the polarization power spectrum, providing a probe into physics of energy scales not conceivable in particle-accelerator physics. CLASS is a unique ground based experiment with extensive consideration given to mitigating systematic uncertainties.

A brief introduction into inflationary cosmology and review of current scientific results will be presented in the light of the upcoming measurements with the newly built CLASS detector. I will detail some of my technical contribution to the construction of this telescope. I have conducted my research under the advise of Prof. Bennett. Additionally the thesis was reviewed by Prof. Marriage, Prof. Kamionkowski, Prof. Chuss, and Prof. Strobel.

Acknowledgments

I would like to thank my wife, friends, members of the Johns Hopkins community, my mentors, teachers, supervisors, and dissertation committee.

The CLASS project receives support from the National Science Foundation Division of Astronomical Sciences under Grant Numbers 0959349 and 1429236.

# Contents


**I Physics of the Origin of the Universe 1**

**1 Introduction to the Big Bang Framework . . . . . 2**

1.1 The Big-Bang Theory . . . . . 3

1.2 Cosmic Microwave Background . . . . . 4

1.3 The CMB in Detail . . . . . 5

1.4 The Horizon Problem . . . . . 8

1.5 The Flatness Problem . . . . . 10

**2 The Theory of Inflation . . . . . 14**

2.1 Introduction to the Theory of Inflation . . . . . 15

2.1.1 Solving the Flatness Problem . . . . . 16

2.1.2 Solving the Horizon Problem . . . . . 17

2.2 Physics of Inflation . . . . . 20

2.2.1 Simple Lagrangian Analysis . . . . . 21

2.2.2 Quantum Fluctuations . . . . . 23

2.2.3 Primordial Seeds . . . . . 24

2.2.4 Scalar and Tensor perturbations . . . . . 25

2.2.5 Constraining inflation . . . . . 27

**3 Connecting Theory with Observation . . . . . 30**

3.1 The Power Spectrum of the CMB . . . . . 31

3.1.1 Cosmic Variance and Gaussianity . . . . . 31

3.1.2 Key Features of the Angular Power Spectrum . . . . . 33

3.1.3 Evolution of a Single Component Universe . . . . . 34

3.1.4 Acoustic Oscillations and their Damping Tail . . . . . 35

3.1.5 The Sachs-Wolfe Plateau . . . . . 38

3.2 The Need to Measure . . . . . 38

**4 Observing Inflation through the CMB . . . . . 39**

4.1 Polarization Review . . . . . 39

4.1.1 Scalar . . . . . 41

4.1.2 Tensor . . . . . 42

4.2 The E and B Mode Decomposition . . . . . 42

4.2.1 Planck Data . . . . . 44

**II Measuring Inflation with CLASS** **46**

**5 Review** . . . . . **47**

5.1 Predictions . . . . . 49

5.2 Measuring the Tensor-to-Scalar Ratio . . . . . 49

**6 CLASS Approach** . . . . . **52**

6.1 Designing for Low-$\ell$ Sensitivity . . . . . 52

6.1.1 Location . . . . . 52

6.1.2 Scan Strategy . . . . . 54

6.2 Foregrounds . . . . . 56

**7 Instrument Design** . . . . . **58**

7.0.1 Stokes Parameters . . . . . 59

7.0.2 The Variable Delay Polarization Modulator . . . . . 59

7.1 Modulator Implementation . . . . . 61

7.2 CLASS Optical Design . . . . . 62

**III Instrument Development** **64**

**8 Cryogenics** . . . . . **65**

8.1 The Dilution Refigerator . . . . . 65

8.2 Cryogenic Housekeeping . . . . . 67

8.3 Details of the Cryogenic Signal Path . . . . . 70
8.3.1 **300 K** Interface . . . . . 70
8.3.2 Hermetic Feedthrough . . . . . 70
8.3.3 Cold Breakouts . . . . . 72
8.3.4 SRS Break-Out-Box . . . . . 74
8.4 Custom Diode Circuit . . . . . 88
8.4.1 Hardware . . . . . 90
8.4.2 Consistent Overhead Byte Stuffing Encoding . . . . . 95
8.4.3 Software . . . . . 97
8.4.4 Interface Isolation . . . . . 97
8.5 The G Measurements . . . . . 100
8.5.1 HP6643 Control Code . . . . . 100
8.5.2 60K Load Test . . . . . 102
8.5.3 **4 K** Load Test . . . . . 104
8.5.4 1K Load Test . . . . . 111
8.6 SRS Mainframe . . . . . 114
8.6.1 SRS Temperature Monitoring . . . . . 114
8.6.2 SRS PID . . . . . 115
8.6.3 SRS Voltage Source . . . . . 115
8.6.4 SRS Software . . . . . 115

**9 Site Software . . . . . 118**

9.1 Pyro in the CLASS Infrastructure . . . . . 119
9.2 Network Considerations . . . . . 120
9.2.1 WiFi Link . . . . . 120
9.2.2 Switch Gear . . . . . 122
9.2.3 Overview of the Mount Networks . . . . . 122
9.2.4 Overview of the Control Room Network . . . . . 123
9.3 Beefy Miracle . . . . . 123
9.4 Data Structure . . . . . 126
9.4.1 Overview . . . . . 127
9.4.2 Science Data . . . . . 128
9.4.3 Additional Mount Data . . . . . 129
9.4.4 Cryogenics . . . . . 129
9.5 Data Storage and Handling . . . . . 130
9.5.1 Storage . . . . . 130
9.5.2 Bürgermeister RAID Configuration . . . . . 131
9.6 Low-Level Mount Control . . . . . 132
9.6.1 Start Up . . . . . 133
9.6.2 General Notes . . . . . 134
9.6.3 The Screen Program . . . . . 134
9.6.4 The Telescope Object . . . . . 136
9.6.5 The Sky Object . . . . . 137

9.6.6 The Source Object . . . 139
9.6.7 Axis Objects . . . 140
9.6.8 Sync Box . . . 142
9.6.9 Shut Down . . . 143
9.7 Scan Commanding . . . 143
9.7.1 General Notes . . . 143
9.7.2 FivePoint Scan . . . 144
9.7.3 DriftScan Routine . . . 145
9.7.4 SkyDip Routine . . . 146
9.7.5 AzScan Routine . . . 147
9.7.6 DecScan Routine . . . 148
9.7.7 ProfileScan Routine . . . 149
9.8 Mount Control Scripting Language . . . 150
9.8.1 Submitting Scripts . . . 151
9.8.2 Precise Timing of Execution Function . . . 151
9.8.3 Loops within a Script . . . 153
9.8.4 Closing Thoughts . . . 153

**IV CLASS Simulation 156**

**10 Software Overview . . . 158**

10.1 Beam Shape . . . 159

10.2 Focal Plane Offset . . . . . 160
10.3 Focal Plane Distortion . . . . . 161
10.4 Creating Time Ordered Data . . . . . 162
10.4.1 Sky Coordinates . . . . . 163
10.4.2 Detector Noise . . . . . 163

**11 Analysis . . . . . 164**
11.1 Mathematical Foundation . . . . . 165
11.1.1 Practical Considerations . . . . . 165
11.2 $\chi^2$ Problems . . . . . 166

**12 Results . . . . . 167**
12.1 Recovering Tau A . . . . . 167
12.1.1 Dip Scan . . . . . 168
12.1.2 A $24$ Hour Lissajous Scan . . . . . 168
12.1.3 Drift Scan . . . . . 169
12.2 Monte Carlo Error Estimation . . . . . 170
12.2.1 Monte Carlo $\alpha$ . . . . . 170
12.2.2 Monte Carlo $\beta$ . . . . . 171
12.2.3 Monte Carlo $\gamma$ . . . . . 171
12.2.4 Observing Time . . . . . 172
12.3 Optimizing the Scan strategy . . . . . 173

12.3.1 Extended scan . . . . . 174

12.4 Conclusion . . . . . 174

# List of Tables


1 WMAP Parameter Results . . . . . 30

2 Scale factor evolution in single component universes. . . . . 34

3 Inflationary Measurables . . . . . 48

4 SRS BoB channell mapping. . . . . 74

5 $60\ \mathrm{K}$ Wire Map . . . . . 84

6 $4\ \mathrm{K}$ Wire Map . . . . . 85

7 $1\ \mathrm{K}$ Wire Map . . . . . 86

8 $100\ \mathrm{mK}$ Wire Map . . . . . 87

9 Map of diode locations and Sleipnir's corresponding channels. . . . . 101

10 Fit Coefficients of $4\ \mathrm{K}$ thermometers. . . . . 108

11 Science Data Overview . . . . . 127

12 Monte Carlo Summary . . . . . 173


# List of Figures


1 BigBang Timeline . . . . . 2

2 The Holmdel Horn Antenna . . . . . 4

3 FIRAS Blackbody Measurements . . . . . 6

4 WMAP CMB data projection . . . . . 7

5 Curvature Distortion of Angles . . . . . 11

6 The Soccer Ball analogy. . . . . 16
7 Inflaton Field Sketch . . . . . 20
8 horizon Exit and Re-entry . . . . . 22
9 WMAP CMB TT Powerspectrum . . . . . 32
10 Energy composition of the universe . . . . . 35
11 Thomson Scattering . . . . . 40
12 Scalar Perturbations . . . . . 41
13 Tensor Perturbations . . . . . 42
14 E and B Mode Sketch . . . . . 43
15 B-Modes in Planck Data . . . . . 44
16 Constrains on the Inflationary Potential . . . . . 50
17 Progress Towards Measuring the BB Powerspectrum . . . . . 51
18 A 3D Model of the VPM Assembly . . . . . 53
19 CLASS Scan Strategy . . . . . 55
20 CLASS Observing Bands . . . . . 56
21 CLASS Artist Sketch . . . . . 58
22 Schematic of VPM Action . . . . . 60
23 A 3D Model of the VPM Assembly . . . . . 62
24 Optical Design for CLASS . . . . . 63
25 300K Break Out Assembly . . . . . 71
26 Cryogenic Feed-through details . . . . . 72

27 60 K Break Out Board . . . . . 73
28 300K Break-Out-Schematic . . . . . 76
29 300K Break-Out-Board . . . . . 77
30 60K Break-Out-Schematic . . . . . 78
31 60K Break-Out-Board . . . . . 79
32 4K Break-Out-Schematic . . . . . 80
33 4K Break-Out-Board . . . . . 81
34 1K Break-Out-Schematic . . . . . 82
35 1K Break-Out-Board . . . . . 83
36 The DAQ heart: LTC2449 . . . . . 88
37 3D Render of the Sleipnir Board . . . . . 89
38 Sleipnir Schematic: Master . . . . . 91
39 Sleipnir Schematic: LTC2449 DAQ . . . . . 92
40 Sleipnir: ATMega328 Schematic . . . . . 93
41 Sleipnir Schematic: Current Source . . . . . 94
42 Sleipnir Schematic: Software Overview . . . . . 96
43 Evolution of Sleipnir . . . . . 98
44 UDT670: Sleipnir's Precursor . . . . . 99
45 April 2014 60K Loading . . . . . 105
46 April $10^{th}$ 2014 Temperature Data . . . . . 106
47 December 2013 60K Relative Calibration . . . . . 107

48 April 2014 4K Loading . . . . . 109
49 April $15^{th}$ 2014 Temperature Data . . . . . 110
50 April $15^{th}$ 1K Loading . . . . . 112
51 April $15^{th}$ 2014 Temperature Data . . . . . 113
52 Standford Research System Main Frame . . . . . 114
53 Ruthenium Oxide Schematic Overview . . . . . 117
54 Basic Pyro Principles . . . . . 118
55 CLASS Network Diagram . . . . . 121
56 Software Overview . . . . . 157
57 Software Schematic . . . . . 159
58 Focalplane Distortion . . . . . 162
59 Fiducial Time Ordered Data . . . . . 164
60 WMAP Tau A Data . . . . . 175
61 WMAP Tau A Drift Scan . . . . . 176
62 WMAP Tau A Lissajous Wobble . . . . . 177
63 WMAP Tau A Drift Scan TOD . . . . . 178
64 Monte Carlo Simulation: $\alpha$ . . . . . 179
65 Monte Carlo Simulation: $\beta$ . . . . . 180
66 Monte Carlo Simulation: $\gamma$ . . . . . 181
67 Monte Carlo Simulation: $\alpha$ . . . . . 182
68 Monte Carlo Simulation: $\beta$ . . . . . 183

69 Monte Carlo Simulation: $\gamma$ . . . . . 184

70 Optimized Scan . . . . . 185

71 Optimized Monte Carlo Simulation: $\alpha$ . . . . . 186

72 Optimized Monte Carlo Simulation: $\beta$ . . . . . 187

73 Optimized Monte Carlo Simulation: $\gamma$ . . . . . 188

74 Optimized Monte Carlo Simulation: $\alpha$ . . . . . 189

75 Optimized Monte Carlo Simulation: $\beta$ . . . . . 190

76 Optimized Monte Carlo Simulation: $\gamma$ . . . . . 191

## Part I

# Physics of the Origin of the Universe

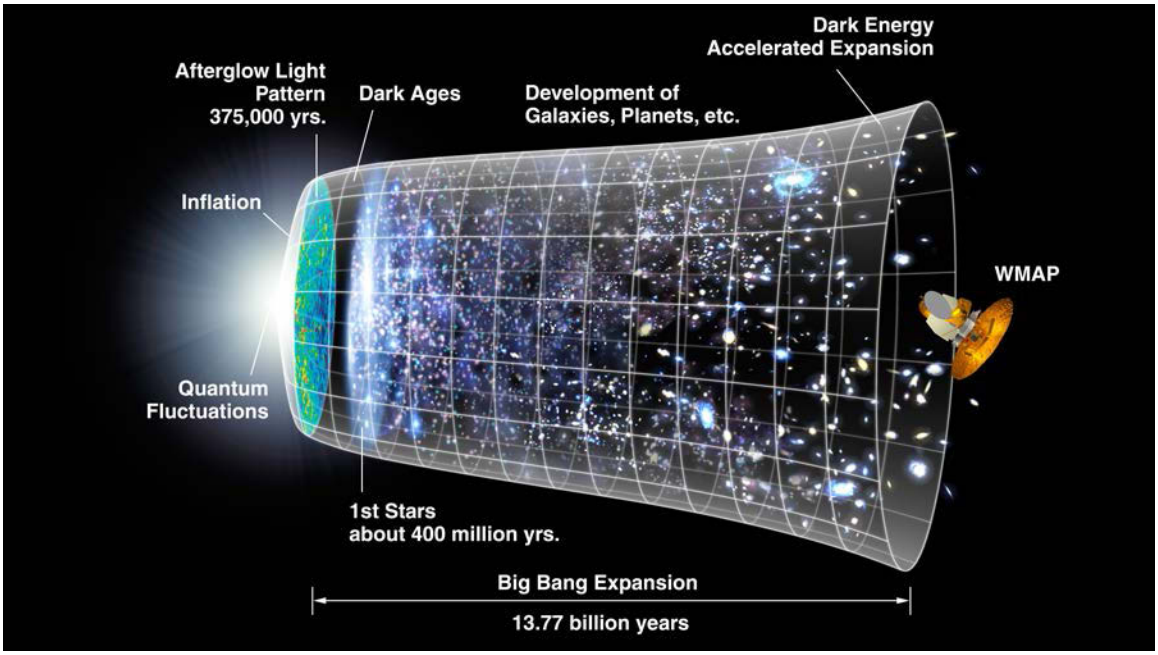


Figure 1: An artists interpretation of the evolution of the universe with values measured by the WMAP science team. [Courtesy of WMAP science team.]

# 1 Introduction to the Big Bang Framework

Humanity has always yearned to know where we come from and what came before us. Seeking to answer this question we have been looking to the stars since recorded history. With the Cosmology Large Angular Scale Surveyor (CLASS) and similar cosmological experiments we finally have an opportunity to study the very beginning of our universe, pushing our knowledge into new territory.

## 1.1 The Big-Bang Theory

The Big Bang theory, not the TV show, is the basis for today's standard model of cosmology. The Big Bang theory proposes a universe that has been expanding and cooling from an initially very dense state for billions of years. In 1927 George Lemaitre first theorized about a homogeneous expanding universe [54]. Alexander Friedman and George Lemaitre both independently found the first dynamic solution to Einstein's equations general relativity, governing the evolution of the universe. This solution is typically referred to as the Friedmann Lemaitre Robertson Walker (FLRW) solution. In the context of this solution the evolution of the scale factor, $a$ is governed by the equation

$$\frac{\ddot{a}}{a} = -\frac{4\pi G}{3}\left(\rho + \frac{3p}{c^2}\right) + \frac{\Lambda c^2}{3}, \tag{1}$$

where $\rho$ is the energy density and $p$ the pressure. This equation also allows for a non-zero cosmological constant, $\Lambda$. Hubble's evidence of an expanding universe was inspired by the observational work of Vesto Slipher, published in 1922. This led to the idea that we can trace the evolution of an expanding universe back to a single point. When we discuss the Big Bang theory we refer to a homogeneous expanding universe governed by Einstein's equations. In 1929 Hubble concluded the isotropic and homogeneous expansion of the universe by combining Slipher's red-shift measurements with distance measurements [43]. In 1948 Ralph Alpher and Robert Herman predicted the the presence of a cosmic microwave background, within the framework of the Big Bang theory. Their prediction would not be verified for another two decades.

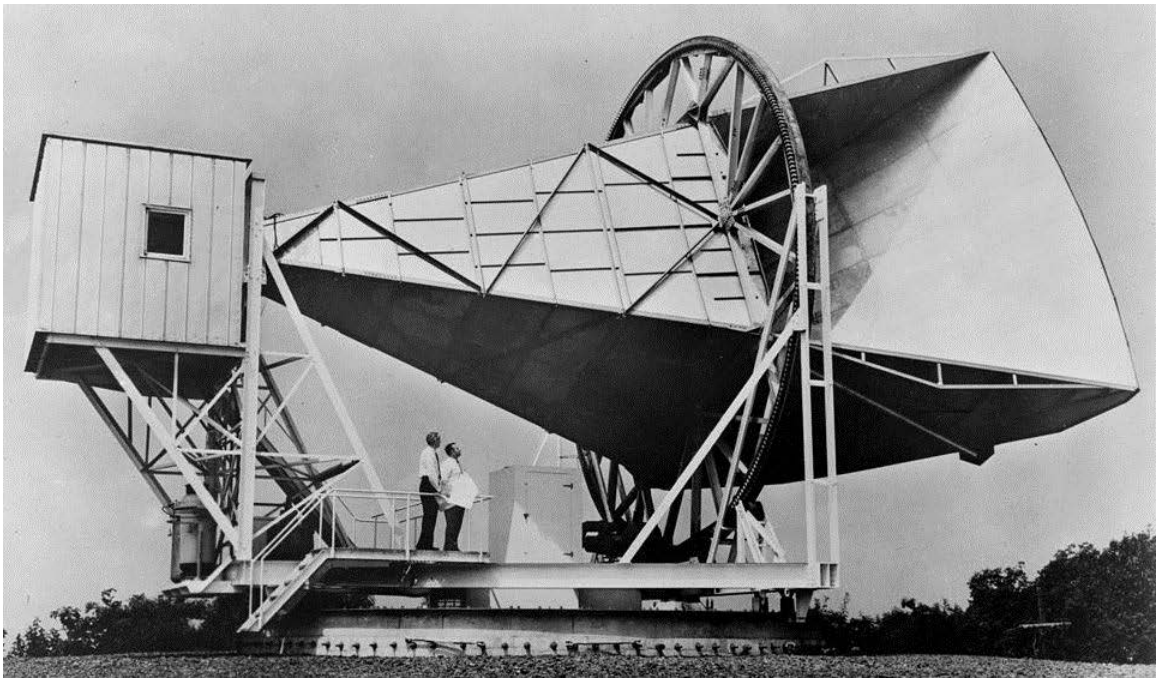

Figure 2: Arno Penzias and Robert Wilson, as seen standing on the platform pointing the Holmdel Horn Antenna, with which they discovered the cosmic microwave background. Located in Holmdel Township, New Jersey, it was designated a National Historic Landmark in 1988 for its fundamental contributions to astronomy. [Courtesy of NASA image library.]

## 1.2 Cosmic Microwave Background

In 1964 Arno Penzias and Robert Wilson, working at Bell Laboratories, made a startling discovery. They measured an isotropic radiation background corresponding to an excess antenna temperature of $3.5 \pm 1$ K at $4.08$ GHz [66]. Without knowing it at that time, Arno Penzias and Robert Wilson discovered what would later become known as the Cosmic Microwave Background (CMB). The CMB was predicted and well described by the Big

Bang theory. In the Big Bang cosmology the universe started in a very hot and dense plasma. The temperature was high enough to ionize the gas, effectively coupling radiation and matter through Thomson Scattering. Roughly $375,000$ years after the birth of the universe the matter density dropped and the temperature cooled enough for the universe to become transparent to the radiation. The radiation released during this epoch of decoupling is what we now observe as the CMB-radiation. The startling fact about the 1964 discovery of the CMB was its existence. This put an end to Einstein's prediction of a steady state universe.

## 1.3 The CMB in Detail

Since the CMB allows us to view early cosmic history, naturally we want to study it in detail. The CMB tells us a great deal about our universe. From it we can deduce the geometry of space, matter and energy densities. In 1992 NASA launched the Cosmic Background Explorer (COBE) to further our knowledge of the universe by studying the CMB. It was the Far Infrared Absolute Spectrophotometer (FIRAS) that confirmed the CMB to have a blackbody spectrum with a temperature of $2.726 \pm .001$ K [61]. As an experimental aside it is important to understand how FIRAS measured the background temperature. FIRAS was designed to compare the background to a precise blackbody. That is, the experimental data, from the CMB, showed a precise match to the onboard blackbody. FIRAS did not directly measure the Planck spectrum as depicted in figure 3, but measured the temperature difference between the CMB and the blackbody load at

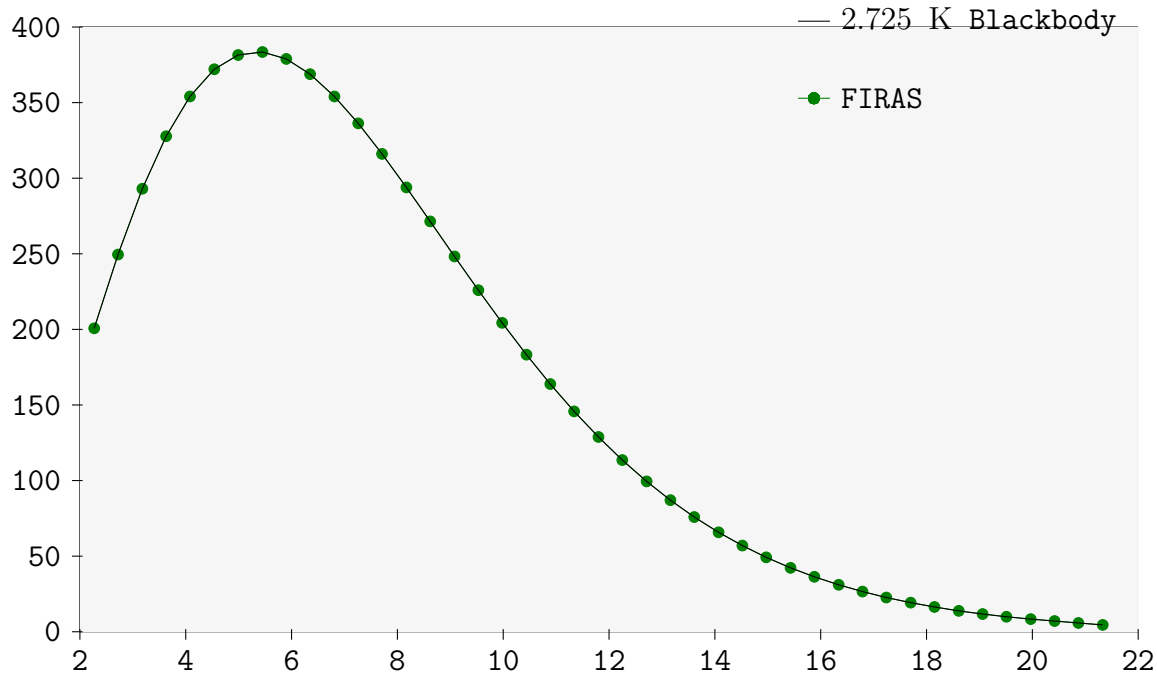


Figure 3: FIRAS measured the spectrum of the CMB to be very exactly that of a $2.726\,\mathrm{K}$ blackbody spectrum. Here the FIRAS data is plotted as the sum of the measured residual and the theoretical blackbody emission. The error on the measurement was so small that the variance is not visible by the naked eye, a remarkably precise measurement. Data taken from [61].

a wide range of frequencies. COBE also carried the Differential Microwave Radiometer (DMR) capable of mapping the CMB with $7^\circ$ resolution. The COBE map is consistent with a smoothed version of the later Wilkinson Microwave Anisotropy Probe (WMAP) map. It clearly showed the microwave emission from our galaxy but most importantly, the DMR discovered the primordial-seeds of structure, an anisotropy of $18.4\,\mu\mathrm{K}$ at angular scales of $l \leq 15$. The formation of structure via gravitational collapse depends on primordial

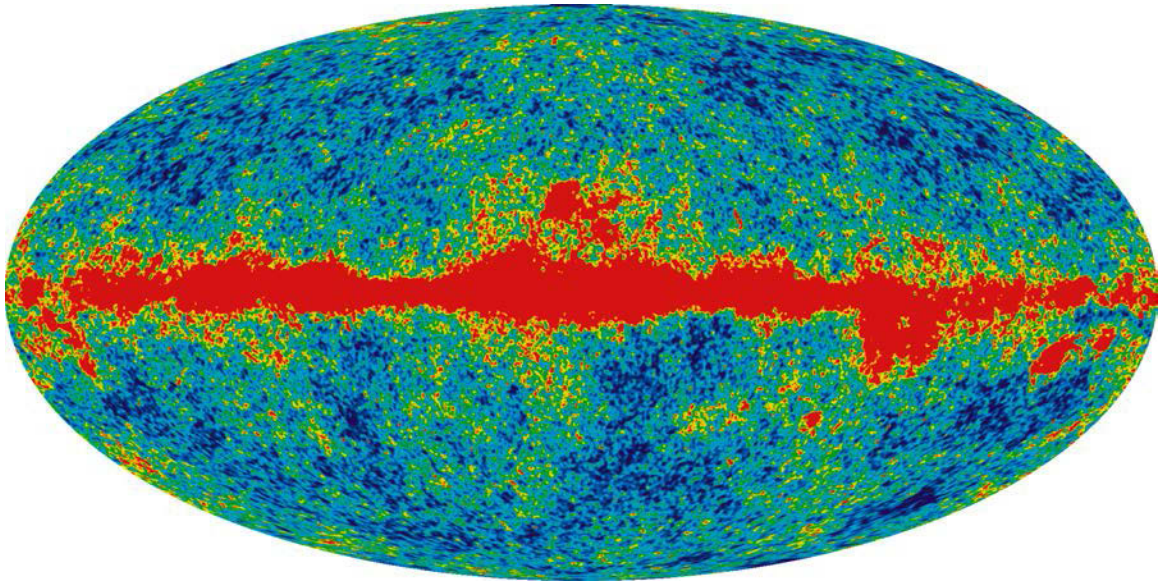

Figure 4: A map projection of the full sky of WMAP temperature data. The data is a product of the Q-band ( $40$ GHz) differencing assembly. Since WMAP is, by design, a differential measurement the monopole is not present in the data. The dipole due to our motion with respect to the CMB has been removed in post-processing. This is essentially a higher resolution and more sensitive version of the maps produced by COBE. [Courtesy of WMAP science team]

overdensities. That is to say, if the CMB were isotropic then structure (galaxies, stars, and life) would not have had the chance to form. In 2001 NASA launched the WMAP to follow up on COBE's measurements with far higher sensitivity and resolution, as seen in figure 4. Among some of WMAP's many achievements is the precise measurement of many important cosmological variables. After analysing WMAP data we now know that most of the universe is made up of stuff we can not see. Specifically only $4.6\%$ of the universe

is filled with baryons. The rest is split between dark matter and dark energy. The former being a type of mass that does not interact with light, taking up $24\%$ of the energy budget. The last $71.4\%$ being a type of energy that is theorized to be responsible for the accelerated expansion of space. As remarkable as these measurements are perhaps the most surprising is the fact that our universe is flat, as discussed in section 1.5.

We now address two challenges to the standard Big Bang Theory, the Horizon Problem and the Flatness Problem (see section 1.4 and 1.5).

## 1.4 The Horizon Problem

The isotropy of the CMB immediately raises what is known as the horizon problem. While the existence of the CMB is well predicted by the standard Big Bang cosmology, it's isotropy is puzzling and unexplainable in the unmodified framework of the Big Bang. A simple thought experiment illuminates the lurking causality violation. Consider two parts of the sky, separated as far as possible, say by looking east and west, they are twice as far apart as as the age of the universe times the speed of light. One correctly concludes that there are parts of the universe that are visible to us but not to each other, that is to say their spheres of causality do not overlap. Since these two areas of the sky are not in causal contact they could not have come to an equilibrium temperature via the mechanisms of thermodynamics. This concept is explored in detail in section 1.4, taking into account the expansion of the universe. Not wanting to invoke fine-tuning, it is the job of a scientist to explain this phenomenon. One solution is to propose a faster-than-light expansion of the

universe during it's infancy. By this mechanism we could separate an area in thermodynamic equilibrium into several causally disconnected spheres. Although these areas can no longer communicate with each other there was a time, before this faster-than-light expansion, where they had enough time to come to an equilibrium temperature. This concept is well accepted in the form inflationary-cosmology.

We can calculate the current proper distance, $d$, to the surface of last scattering, $t_{ls}$ by integrating along a null geodesic as the scale factor, $a$, changes with time. The distance to the surface of last scatter can therefore be calculated by the equation,

$$d_{ls} = c \int_{t_{ls}}^{t_0} \frac{dt}{a(t)} \tag{2}$$

where $t_{ls}$ is the time of last scattering. To properly evaluate this integral we have to know how the scale factor $a$ evolved with time. This depends on the curvature and energy composition of the universe. The latest measurements from WMAP define a Benchmark Model that includes dark energy, cold dark matter, as well as baryonic matter in a flat universe. In the context of the Benchmark Model, we numerically evaluate the distance to the surface of last scattering to be equal to $.98$ of the horizon distance [73]. The horizon distance, $d_h$, is the distance to the edge of the observable universe. It is the furthest distance that two objects can be separated and still be in causal contact. We find that two points in the sky, separated by $180^\circ$ are separated by a proper distance of $1.96\ \mathrm{d_h}$. These two points could not be causally connected as they are farther apart than the horizon distance. If they are not in causal contact then they have not had time to exchange information about their respective temperatures and therefore could not have come to equilibrium via any physical

mechanism, under the constraints of the standard Big Bang evolution.

Although the above analysis is correct, it is incomplete. We recall that the temperature fluctuations in the CMB are a direct result of the density perturbations before decoupling occurred. So we should examine the horizon distance at the time of decoupling. Assuming a radiation dominated cosmology the distance can be calculated simply. According to the standard Big Bang, the equation

$$d_{ls} = 2\frac{c}{H(t_{ls})} \tag{3}$$

is a then conservative over estimation of the actual distance to the surface of last scattering. At the time of decoupling the Hubble constant was approximately given by $H \approx .2\,\mathrm{Mpc}/c$. So at the time of decoupling the causal horizon was only $.4\ \mathrm{Mpc}$. We can now calculate the angular separation, as seen on today's sky, of these causal spheres:

$$\theta = \frac{.4\ \mathrm{Mpc}}{14\ \mathrm{Mpc}} \approx 2^{\circ} \tag{4}$$

Since there are approximately $41253$ square degrees on the surface of a sphere we conclude that there are over $10,000$ casually disconnected patches on the sky. The Big Bang theory fails to explain this phenomenon.

## 1.5 The Flatness Problem

As the universe expands, gravitation works against this expansion. We can describe the universe by its energy density. Specifically we can compare this energy density to the critical density, below which the expansion of the universe will finally be overcome by

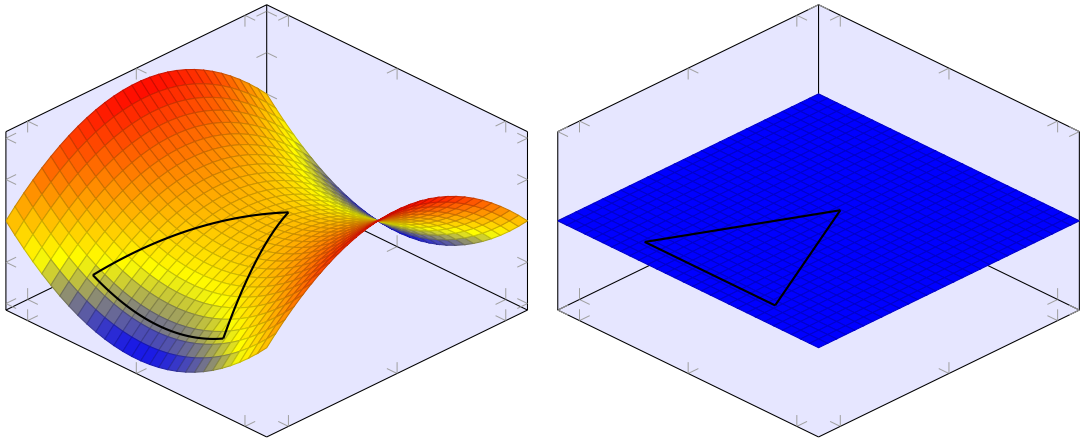

Figure 5: Although we can not easily visualize 3-D curved space we can visualize 2-D curvature by embedding it in three dimensions. The left cartoon shows a hyperbolic plane, this is what the universe would look like if it had negative curvature. On the right it depicts Euclidean geometry, a flat universe, one without curvature. We can now see how curvature distorts angles. As a matter of fact, negative curvatures will make apparent angles appear smaller. Positive curvature will make the angles appear larger.

the gravitational attraction and come to a halt. This universe collapses back onto itself. A universe with an energy density less than the critical density will continue to expand forever. What is remarkable is that the universe's energy density is exactly, or to within $.4\%$, equal to the critical density [8]. In a geometric sense this describes a flat Euclidian geometry. The Big Bang cosmology fails to explain this phenomenon without requiring tremendous fine tuning of initial conditions. Let us now explore this problem in detail.

The idea of a curved three dimensional space is difficult to visualize. Luckily we can

understand the concept of curved space by picturing two-dimensional surfaces embedded in three-dimensional space. The curvature of the underlying space changes the geometry. For example, the sum of all angles in a triangle add up to $180^\circ$ in Euclidian space. Euclidian space is space with zero curvature. The introduction of positive or negative curvature will distort angles. The result is that the angles of a triangle no longer add up to $180^\circ$. Figure 5 shows a hyperplane, or negatively curved space on the left and Euclidian, or flat space on the right. Triangles are drawn on both surfaces to illustrate the distortion of the triangle due to the underlying geometry. The curvature of the universe can be constrained by measuring angles using so-called "standard rulers" [38].

In Einstein's General Relativity we can also relate the spatial curvature of the universe to the energy density of the universe, through the use of the Friedmann-Lamitre solution (equation 1) as

$$\Omega_k = 1 - \Omega(t) = -\frac{\kappa c^2}{R_0^2 a(t)^2 H(t)^2} \, . \tag{5}$$

$\Omega_k$ is the curvature energy density, defined as the deviations of the total energy density, $\Omega$ from one. $R_0$ is the curvature radius at the present time, and $\kappa$ is the curvature parameter. WMAP data alone suggests an insignificant deviation from $\Omega_k = 0$ of roughly $.037^{+0.044}_{-0.042}$ [8]. When combined with other data sets the constraints are tightened around to $0.001 \pm 0.0012$ [8]. This is remarkable as the curvature density, $\Omega_k$, was constantly growing, during the radiation and matter dominated phase of our universe, as follows:

$$\Omega_k(t) = \frac{\Omega_{k,0} a^2}{\Omega_{r,0} + a\Omega_{m,0}} \, . \tag{6}$$

Specifically the curvature was growing proportional to $t^{1/2}$ and $t^{2/3}$ during the radiation-dominated phase and the matter-dominated phase, respectively. Although the WMAP data is consistent with $\Omega_k = 0$, we take an upper limit of $|\Omega_k| \leq .1$, and extrapolate the curvature parameter as far back as the Planck time at $t_P \approx 5 \times 10^{-44}\,\mathrm{s}$. We find that curvature parameter was extraordinarily close to zero [73],

$$\Omega_k \leq 1 \times 10^{-60}\,. \tag{7}$$

This would require an unacceptable degree of fine-tuning of the initial conditions.

# 2 The Theory of Inflation

The theory of inflation [35] is, currently, the leading explanation of the phenomena the Big Bang cosmology fails to explain. Inflation is characterized by an early-time exponential expansion. From the observed isotropy of the sky and flatness of space we can estimate the order of magnitude by which the universe must have expanded. We find that the universe multiplied in size by at least a factor of $e^{60}$. Although we do not know yet, inflation could be the result of a symmetry breaking that occurs at roughly $10^{16}\ \mathrm{GeV}$.

Quantum fluctuations are transmuted into particles through the process of re-heating as the inflaton field stops driving the expansion of the universe. While the exact mechanism of inflation is not yet known, what is important is to note that the theory of inflation makes key predictions. The theory states that such an expansion of space would generate gravitational waves. It is this hypothesis that modern CMB experiments are trying to test. Observing primordial gravitational waves, or the remnants thereof, would constitute a strong test of inflation. In the following section I will cover the fundamentals of the theory of inflation and how the theory explains currently observed phenomena.

This section is meant to provide the necessary background for understanding the requirements of CMB experiments aimed for exploring the inflationary period of the universe. The details are explored in the literature (see [24, 63, 78]).

## 2.1 Introduction to the Theory of Inflation

Space undergoes an accelerated expansion during inflationary cosmology. It is this acceleration of the expansion, $\ddot{a} > 0$ that solves the Flatness and Horizon problems if the acceleration has a sufficent duration. This type of accelerated expansion occurs when the universe is dominated by an energy density with $w < -1/3$, where $w$ is the constant relating energy density to pressure in the equation of state,

$$\rho = w\epsilon. \tag{8}$$

Einstein's equations allowed the inclusion of a cosmological constant with $w = -1$. Thus the most simple assumption for inflation is that the energy density of the universe was dominated by positive cosmological constant, $\Lambda_i$. Here the subscript identifies the cosmological constant during inflation. This cosmological constant would then drive an exponential expansion. We also note that in such a cosmology the Hubble constant, $H_i$ is constant and equal to $\sqrt{\Lambda_i/3}$. Since this type of expansion is exponential it is convenient to quantify the factor by which space expanded in terms of $e$. That is, we refer to the number, $N$ of $e$-foldings, describing an expansion by a factor of $e^N$, as:

$$\frac{a_f}{a_i} = e^{H_i \times (t_f - t_i)} \quad \Rightarrow \quad N \equiv H_i(t_f - t_i)\,, \tag{9}$$

where $t_f$ is the time when inflation stops and $t_i$ is the time inflation starts. A reasonable assumption might be that inflation started around the GUT time, $t_i \approx 10^{-36}$ and lasted roughly $100$ Hubble times. The universe would have undergone $100$ e-foldings, or the

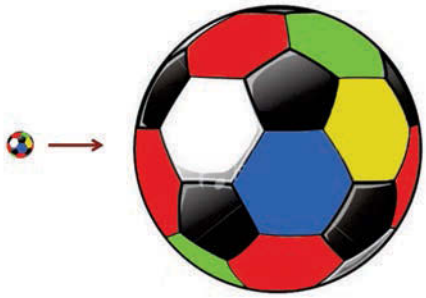

Figure 6: What inflation does to an inhomogeneous curved space can be visualized by drawing an analogy to a small multi-colored soccer ball. In this analogy the different colors represent inhomogeneities of space. Inflation has the effect of increasing the radius of curvature of the soccer ball by such a huge amount that our entire universe is tiny compared to a patch on the soccer-ball. Sufficient inflation has the effect of making the curvature of space to appear locally small compared to the entire observable universe. In this analogy we would observe a nearly flat homogeneous space, not because the universe is globally flat and homogeneous, but because our observable universe is nearly flat and homogeneous. Analogy and figure taken from [58].

scale factor increased by $10^{43}$. This is sufficient to solve the problems of the Big Bang theory.

### 2.1.1 Solving the Flatness Problem

The flatness problem is easily solved. Conceptually this can be understood with a soccer ball analogy, see figure 6. Take the initial universe as a curved, inhomogeneous space-time

geometry, or analogously a small multi-colored soccer ball. Sufficient expansion of space would have the effect of our universe being a tiny piece of one of these squares. Since our observable universe is now much smaller then the inhomogeneities and curvature, we are no longer sensitive to them and observe a flat homogeneous space. This expansion of space stretches out any curvature to imperceptible limits. We use equation 5 to find that the curvature density shrinks during the inflationary period as

$$\Omega_k(t) \propto e^{-2H_i t} \,. \tag{10}$$

Specifically the curvature density decreased by $2N$ e-foldings. Even if we assume a maximally curved universe with curvature density equal to one, the aforementioned inflationary scenario (with $N = 100$) would reduce the curvature density to $10^{-87}$, well within the measured limits given in section 1.5.

### 2.1.2 Solving the Horizon Problem

As discussed earlier, a solution to the flatness problem requires us to find a way to separate causally connected patches of the sky so far that they appear to be no longer causally connected. That is we must take two coordinates that are within each others particle horizon and move them outside of each others sphere of causality. Since the particle horizon is defined by the distance light has had to travel since the beginning of the universe, intuitively one would expect this horizon to grow over time. To discover that this is not the case we need to invoke general relativity. We write down the horizon size, $r$ in co-moving

coordinates as

$$r(t) = c \int_0^t \frac{dt}{a(t)} \, . \tag{11}$$

We adopt the scale factor for a radiation-dominated universe. Here $a_0$ is the scale factor at $t = 0$ with $a_i = a_0 t^{1/2}$. Finally, we remember that $H = t/2$ during a radiation dominated cosmology. The comoving and physical horizon are calculated as follows:

$$d_c(t_i) = c \int_0^{t_i} \frac{dt}{a_0 t^{1/2}} = 2c \frac{t_i^{1/2}}{a_0} = 2c \frac{t_i}{a_i} \quad \Rightarrow \quad d_p(t_i) = 2ct_i = \frac{c}{H_{t_i}} \, . \tag{12}$$

We note that the co-moving particle horizon is expanding at the same rate that space is expanding. The result of which is that during a radiation dominated cosmology the particle horizon is equal to the Hubble horizon. Noting that during inflation the Hubble time is equal to the conformal time at the start of inflation, $2t_i = H_i^{-1}$, we can expand this calculation to find the horizon distance at the end of inflation, $r_f$, as

$$\frac{d_c(t_f) - d_c(t_i)}{c} = \int_{t_i}^{t_f} \frac{dt}{a_i e^{H_i(t-t_i)}} = \frac{1}{a_i e^{-H_i t_i} H_i} \left( \frac{1}{e^{H_i t_i}} - \frac{1}{e^{H_i t_f}} \right) = 2 \frac{t_i}{a_i} \left( 1 - \frac{1}{e^N} \right) \, . \tag{13}$$

We can see that the co-moving particle horizon saturates at a constant value during inflation. Given a sufficient number of e-foldings the final form of the co-moving particle horizon at the end of inflation takes a simplified form expressed in terms of the scale factor, and time, at the start of inflation,

$$d_c(t_f) = 4c \frac{t_i}{a_i} \quad \Rightarrow \quad d_p(t_f) = 4ct_i e^N \, . \tag{14}$$

Equation 14 shows that the particle-horizon is increased by a factor of $2e^N$ while $H$ remains constant, thus breaking the one-to-one correspondence between the Hubble horizon and

the causal horizon. This massive expansion of the particle horizon provides a large enough horizon, at the time of last scattering, to satisfy causality while solving the horizon problem. Concretely, we calculate the horizon size after inflation given that inflation started around the GUT time,

$$d_p(t_f) \approx 1 \text{ pc} \,. \tag{15}$$

We can now evolve this forward in time to estimate the particle horizon at the time of last scattering, $t_s$. We arrive at a lower limit by assuming a radiation dominated cosmology.

$$d_p(t_s) = a_s \left(d_c(t_f) + d_c(t_s)\right) = a_i * e^N * (t_s - t_f)^{1/2} \left(d_c(t_f) + d_c(t_s)\right) \tag{16}$$

We simplify the above by noting that the time of last scattering is much larger than the time at which inflation ended, $t_s \gg t_f$. Since the co-moving particle horizon stagnates during inflation the right hand sum is dominated by the co-moving particle horizon at the time of last scattering. We also substitute the co-moving particle horizon, $d_c(t_s)$ according to equation 12, to get

$$d_p(t_s) \approx 2ct_s \times e^N \quad \text{and} \quad d_p(t_s) \approx \frac{e^N}{H(t_s)} \,. \tag{17}$$

Here we substituted the inverse Hubble constant at the time of last scattering for the time of last scattering. We can do this as the inflationary period has no appreciable affect on the Hubble constant. Now it is easy to see that inflation has the effect of increasing the particle horizon by a factor of $e^N$ over what it would have been without inflation. Given a hundred e-foldings this would make the physical particle horizon roughly $10^{43}$ Mpc, during the time of last scattering. This is vastly more than required to solve the horizon problem.

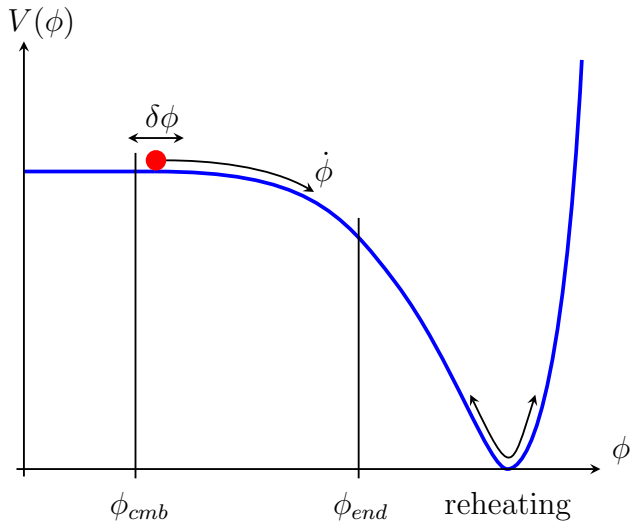


Figure 7: A sketch of a sample inflaton field. The key features of this inflaton field, as discussed in the text, include the quantum oscillations of the field, $\delta\phi$, and it's roll, $\dot{\phi}$. The points in the evolution of the field, during which CMB-probed anisotropy is created and when inflation ends are also marked with $\phi_{CMB}$ and $\phi_{end}$.

## 2.2 Physics of Inflation

In this section I will give an overview of the physics of inflationary cosmology. I will show that quantum oscillations of the inflaton field are converted to classical perturbations [28]. Finally, a decomposition of the perturbation as scalar, vector and tensor perturbations will follow.

### 2.2.1 Simple Lagrangian Analysis

The Lagrangian of a homogeneous scalar field, is

$$\mathcal{L} = a^3(t)\left(\frac{\dot{\phi}^2}{2} - V(\phi)\right) . \tag{18}$$

From this we derive the evolution of the field,

$$\ddot{\phi} + 3H\dot{\phi} + \frac{\partial V}{\partial \phi} = 0 . \tag{19}$$

This is the equation for motion of an object falling through a viscous medium. The viscous drag term, $3H\dot{\phi}$ is referred to as "Hubble friction". This makes the field energy decay to the minimum, as well as providing a mechanism to slow down the evolution of the scalar field.

To make inflation last long enough we impose a slow-roll approximation, which effectively results in $w \approx -1$. We noted earlier that a cosmological term with $w = -1$ will produce exponential expansion of space with a constant Hubble parameter, the condition for this type of accelerated expansion is $w < -1/3$.

To connect the Hubble parameter with the inflaton potential we examine the FRW equation again. Here we make a flat space approximation and substitute the energy density from the Lagrangian to get

$$H^2 = \left(\frac{\dot{a}^2}{a}\right) = \frac{8\pi G}{3}\left(\frac{\dot{\phi}}{2} + V(\phi)\right) . \tag{20}$$

If we make the assumption that the potential is much larger then the time derivative of $\phi$ this is called the slow roll approximation then we can relate the Hubble parameter to the

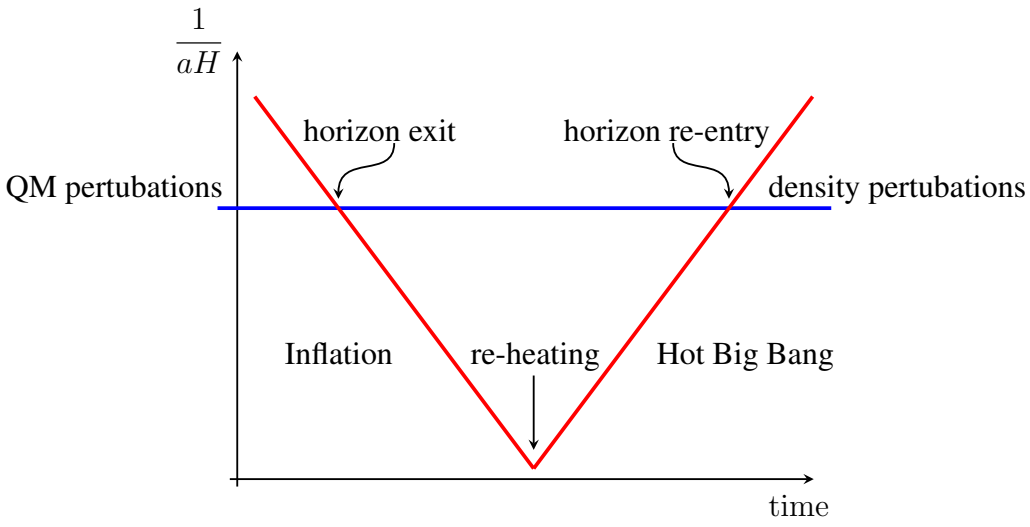


Figure 8: A sketch of the Hubble horizon plotted in co-moving coordinates against logarithmic time. During inflation the size of the of the Hubble radius, $\frac{1}{aH}$ is shrinking and after inflation the horizon begins to grow again. Re-heating sets the stage for the hot Big Bang theory to take over after inflation. We also see that earlier perturbations re-enter the horizon as classical perturbations at a later time.

potential

$$H = \frac{8\pi G}{3} V(\phi) \, . \tag{21}$$

It makes $V(\phi)$ nearly constant resulting in an accelerated expansion of the form discussed earlier. In section 2.2.4, we will use this to make predictions about the statistical properties of the CMB.

### 2.2.2 Quantum Fluctuations

The inflaton field, $\phi$ will fluctuate around its mean state, as demanded by quantum mechanics. In understanding how these quantum fluctuations are converted to classical, or density perturbations the Hubble radius plays a crucial role. (It is important to not confuse the Hubble horizon with the particle horizon.) Only accelerated expansion results in a shrinking Hubble horizon as discussed in section 1.4.

To best understand why the Hubble radius is an important distance measure we consider the Klei-Gordon equations for a scalar field. This can be derived by varying the action of a free scalar field, $\phi$, in an expanding universe. We write this equation in Fourier space as

$$\ddot{\psi} + 3H\dot{\psi} + k_p^2\psi = 0 \tag{22}$$

so that we may make a statement about the Fourier modes. Here $k_p$ is the physical wave number [28]. We note that this equation is that of a classical damped harmonic oscillator. So we write the damping factor in co-moving coordinates as

$$\zeta = \frac{3aH}{k} \, . \tag{23}$$

This system is critically damped when $3aH = k$, under-damped for $3aH < k$, and over-damped for $3aH > k$. Thus we conclude that for sub-Hubble scales, $k > aH$, the damping term is negligible leading to oscillations of the field. For the super-Hubble scales, $k < aH$, the left most term is negligible, freezing the perturbations.

We now have the tools to understand how inflation creates perturbations. Large scale modes leave the horizon earlier and re-enter later than smaller-scale modes. Thus we can

place a lower bound on when inflation must have started. Specifically inflation could not have started later than the particle horizon distance at the time the CMB was created. In figure 7 this state is denoted as $\phi_{CMB}$.

### 2.2.3 Primordial Seeds

Inflation will effectively erase all traces of initial conditions. The rapid expansion of space will redshift any classical perturbations that may have been present before inflation. inflation insures the end result of a homogeneous universe. inflation also dilutes any relic, pre-inflation, particles to undetectable density limits. This is the reason we do not see topological defects such as the magnetic monopole.

inflation produces a super-cooled and empty universe. Then, the conversion of potential energy to kinectic energy produces particles and re-heats the universe. The process by which re-heating occurs is not fully understood, but it occurs when the inflaton field decays and enters an oscillatory state at the end of inflation. Re-heating is when the universe transitions from $w \approx -1$, to a radiation dominated $w = 1/3$ [6].

It is now believed that processes similar to quantum squeezing occur outside of the Hubble horizon [16, 64]. This combined with the decoherence of the quantum states causes the classicalization of super Hubble horizon modes [48, 60]. The reentry of these states causes violent particle production of a non thermal spectrum, which then thermalizes through scattering [74].

### 2.2.4 Scalar and Tensor perturbations

The quantum perturbations of the inflaton field and the space-time metric are defined as

$$\phi(t,\vec{x}) = \bar{\phi}(t) + \delta\phi(t,\vec{x}) \quad \text{and} \quad g_{\mu\nu}(t,\vec{x}) = \bar{g}_{\mu\nu}(t) + \delta g_{\mu\nu}(t,\vec{x})\ . \tag{24}$$

Perturbations are decomposed into scalar, vector and tensor components [10]. Translation invariance of the evolution of the perturbations allow us to describe these perturbations in Fourier space,

$$Q_{\vec{k}}(t) = \int d^3\vec{x} Q(t,\vec{x}) e^{i\vec{k}\cdot\vec{x}} \quad \text{with} \quad Q = \delta\phi, \delta g_{\mu\nu} \tag{25}$$

so the Fourier modes do not interact [57]. Scalar, vector and tensor perturbations are distinguished by their rotational invariance. These have helicity, $m$ equal to $0$, $\pm 1$, and $\pm 2$, respectively. That is, their amplitude is multiplied by $e^{im\Psi}$ when the coordinate system is rotated by $\Psi$.

$$Q_{\vec{k}} \to e^{im\Psi} Q_{\vec{k}} \tag{26}$$

This decomposition is used because each of these classes of perturbations evolve separately [7].

Scalar perturbations are perturbations in the energy density or mass density. These can be described by a perturbation $\zeta(t,x)$ of the metric,

$$g_{\mu\nu} = a^2(t)\left[1 + 2\zeta\right]\delta_{\mu\nu}\ . \tag{27}$$

Geometrically this represents curvature fluctuations on constant-density hypersurfaces. Envoking the slow-roll assumption it can be shown that this scalar perturbation arises from

the fact that inflation ends at slightly different times for the perturbed inflaton field. That is, the scalar perturbations arise due to a time-delay $\delta t(\vec{x})$ at the end of inflation [36]. The scale dependence of the scalar perturbation power spectrum, $P_s$ is defined by a power law and quantified by the scalar spectral index, or primordial tilt, $n_s$, as

$$n_s - 1 \equiv \frac{d \ln P_s}{d \ln k}. \tag{28}$$

Scale invariance, or $n_s = 1$ means equal gravitational potential fluctuations on all scale sizes. Inflation slows and stops, putting a slight tilt into the spectrum, as discovered by WMAP [8]. A deviation from a pure power law, with a constant value of $n_s$, is defined by the scalar running,

$$\alpha_s \equiv \frac{dn_s}{d \ln k} \, . \tag{29}$$

The power spectrum of the scalar perturbations depends on the scalar amplitude, $A_s$, at a arbitrary pivot scale, $k_\star$, and the scalar index [12], with

$$P_s(k) = A_s(k_\star) \left( \frac{k}{k_\star} \right)^{n_s - 1} \, . \tag{30}$$

Single-field slow-roll inflation models predict nearly gaussian scalar perturbations, however, substantial non-gaussianity is predicted by many other inflationary models [2,59]. The non-gaussianity of these perturbations have already been limited by WMAP and Planck, (see section 4.2.1 for a review of this topic), but future galaxy redshift surveys should improve upon these limits.

Vector perturbations are special, unlike scalar and tensor perturbations they are divergence free. In the absence of conformal invariance breaking couplings these vector per-

turbations are red-shifted by inflation and instead of being amplified, decay in the super-horizon. One of the significant predictions of inflation is the absence of large-scale vector perturbations [25, 72]. For this reason I will not discuss this further.

Tensor perturbations can be uniquely described by a gauge-invariant metric perturbation $h_{\mu\nu}$. The Friedmann-Robertson-Walker equation is modified similar to equation 27 as

$$g_{\mu\nu} = a^2(t)\left[\delta_{\mu\nu} + h_{\mu\nu}\right] \quad \text{with} \quad \delta_\nu h_{\mu\nu} = h^\mu_\mu = 0\,. \tag{31}$$

Physically this perturbation corresponds to gravitational wave fluctuations with two polarization states, $h^+$ and $h^\times$ [77]. As with the scalar modes, the tensor power spectrum is an approximate power law quantifed with the tensor index, $n_t$, as

$$n_t \equiv \frac{d\ln P_t}{d\ln k}\,. \tag{32}$$

Without the inclusion of tensor running the tensor power spectrum takes on the form

$$P_t(k) = A_t(k_\star)\left(\frac{k}{k_\star}\right)^{n_t(k_\star)}\,. \tag{33}$$

CMB experiments are sensitive to the ratio of the tensor to scalar power spectra. This tensor-to-scalar ratio is

$$r \equiv \frac{P_t}{P_s}\,, \tag{34}$$

defined at a fiducial scale.

### 2.2.5 Constraining inflation

The scalar and tensor power spectra can be used to make predictions about fundamental constants during inflation. As mentioned before, the scalar perturbation can be though of

as a time-delay,

$$\zeta \equiv -H\delta t \, . \tag{35}$$

The relation between the Hubble parameter and the scalar and tensor power spectra, written in Planck units [76], is

$$P_s(k) = \left(\frac{H}{\dot{\phi}}\right)^2 \left(\frac{H}{2\pi}\right)^2 \, . \tag{36}$$

The right hand side should be evaluated at $k = aH$ for both the scalar and tensor power spectrum,

$$P_t(k) = \frac{8}{M_{pl}^2} \left(\frac{H}{2\pi}\right)^2 \, . \tag{37}$$

The tensor-to-scalar ratio depends only on the time evolution of the inflaton field, $\dot{\phi}$, so

$$r = \frac{8}{M_{pl}^2} \left(\frac{\dot{\phi}}{H}\right)^2 \, . \tag{38}$$

We generally assume that inflation satisfies the slow-roll conditions [56], so we introduce the slow-roll paramaters $\epsilon$ and $\nu$:

$$\dot{\phi} = -\frac{V'}{3H} \tag{39}$$

$$\epsilon \equiv \frac{m_{pl}^2}{16\pi} \left(\frac{V'}{V}\right)^2 \approx -\frac{\dot{H}}{H^2} \ll 1 \tag{40}$$

$$|\nu| \equiv \left|\frac{m_{pl}^2}{8\pi} \frac{V''}{V}\right| \ll 1 \, , \tag{41}$$

where these slow-roll parameters relate to the first and second derivative of the potential, respectively.

With these definitions, the slow-roll parameters express the shape of the inflation field [56] as

$$P_s(k) = \frac{1}{24\pi^2 M_{pl}^4}\frac{V}{\epsilon} \quad \text{and} \quad n_s - 1 = 2\nu - 6\epsilon \tag{42}$$

$$P_t(k) = \frac{2}{3\pi^2}\frac{V}{M_{pl}^4}\ . \tag{43}$$

As before, these are evaluated at $k = aH$. This leads us to the slow-roll consistency relation governing the lowest order relation between the scale factor and the tensor index,

$$r = -8n_t\ . \tag{44}$$

In summary we find that a measurement of the tensor power spectrum conveys information about the potential amplitude ($V$), the scalar power spectrum probes the first derivative of the potential ($V'$), the scalar index measuring the second derivative ($V''$), and finally the scalar running gives the fourth order correction ($V'''$) of the inflation field. These parameters can be used to reconstruct the shape of the potential as a Taylor series around the CMB scales [51, 52, 55, 65].

| | | |
|---|---|---|
| Physical baryon density | $\Omega_b h^2$ | $.02264 \pm 0.00050$ |
| Physical cold dark matter density | $\Omega_c h^2$ | $.1138 \pm 0.0045$ |
| Dark energy density | $\Omega_\Lambda$ | $.721 \pm 0.025$ |
| Curvature pertubations $k_0 = .002\mathrm{Mpc}^{-1}$ | $10^9 \Delta_R^2$ | $2.41 \pm 0.10$ |
| Scalar spectral index | $n_s$ | $0.972 \pm 0.013$ |
| Reionization optical depth | $\tau$ | $.089 \pm 0.014$ |

Table 1: Maximum likelihood $\Lambda\mathrm{CDM}$ Parameters as determined by the WMAP science team. Results taken from [8].

# 3 Connecting Theory with Observation

To connect theory with observation we must consider the statistics of the CMB isotropy. One key statistic is the CMB power spectrum. In the following sections I will introduce the power spectrum of the CMB. Although Planck data presents improved measurements, my discussion will focus around WMAP data for chronological reasons [67]. Studying these statistical properties of the fluctuations allow us to constrain the parameters governing the evolution of our universe.

## 3.1 The Power Spectrum of the CMB

We begin by expanding the observed temperature across the sky, $T(\theta, \phi)$, using spherical harmonics:

$$T(\theta, \phi) = \sum_{lm} a_{lm} Y_{lm}(\theta, \phi). \tag{45}$$

This is similar to a Fourier analysis, however, it is using spherical harmonics as the most appropriate basis function for a sphere (the sky). Averaging over $m$ leads us to the convenient measure of power in any specific multipole

$$C_l^{TT} = \langle a_{lm}^T a_{lm}^{T*} \rangle \ . \tag{46}$$

As we will discuss later there are also the E-mode, and B-mode spectra of polarization. This presents the three power spectra, $C_l^{TT}$, $C_l^{EE}$, and $C_l^{BB}$, along side of three cross-spectra, $C_l^{TE}$, $C_l^{TB}$, and $C_l^{EB}$. It is the temperature power spectrum that I will focus on now, before introducing polarization in section 4.1.

### 3.1.1 Cosmic Variance and Gaussianity

Cosmic variance can be pedagogically understood as the expected variations in measured values as sampling a statistical distribution of multipole moments. Small angular scale multipoles can measured repeatedly across the sky, while there is only one measurement of the monopole temperature. With statistics of small sample size (in this case at large-angular scales) it is difficult to draw conclusions about the precise average.

To understand this concept in detail we have to recall that our measured sample statistics

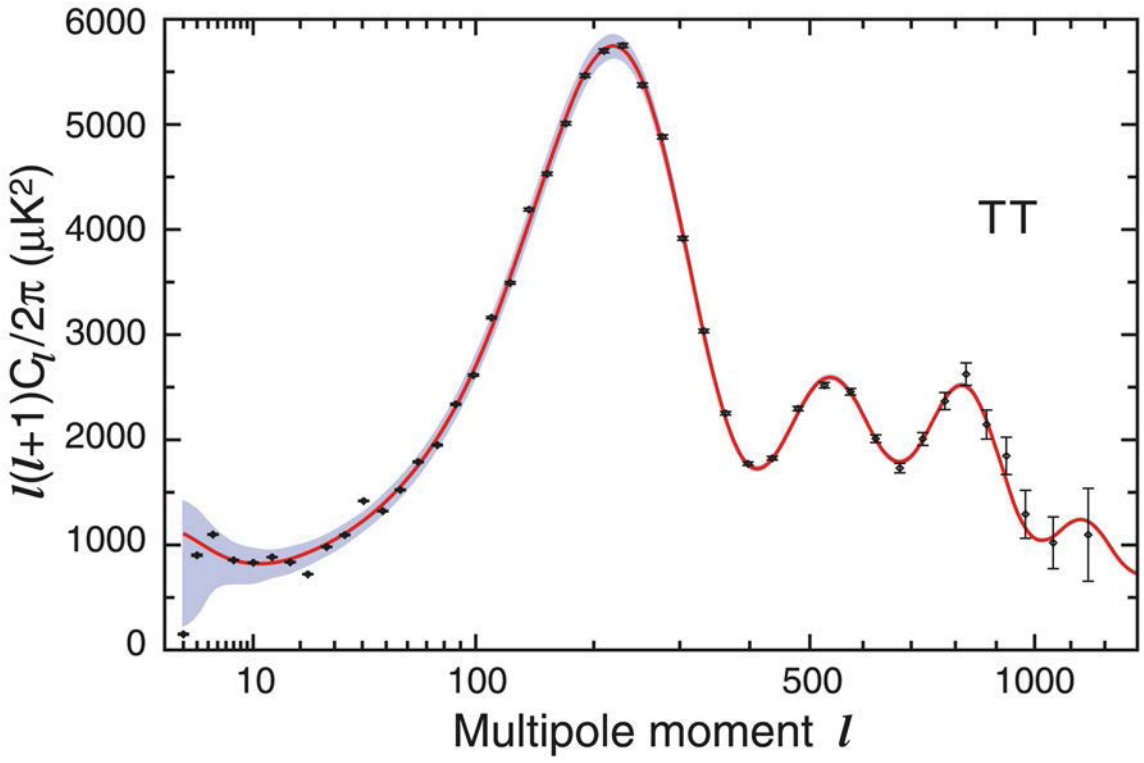


Figure 9: The TT power spectrum of the WMAP temperature data. A theoretical fit is plotted in red. The grey shading shows the cosmic variance limit. We note that the low-$l$ measurement of WMAP is within the cosmic-variance limit. This means we could not make a more accurate low-$l$ temperature measurement. [Courtesy of WMAP science team.]

are only an estimator for the given variable. That is the measured $\widehat{C}_l$ are an estimator of the true $C_l$ such that they are equal in the limit of $l$ approaching infinity

$$\lim_{l\to\infty} \widehat{C}_l = C_l \, . \tag{47}$$

Under the assumption that the perturbations are generated by random gaussian processes it

can easily be shown that these estimators are unbiased estimators, are distributed like a chi-squared random variable with $2l+1$ degrees of freedom, and have variance proportional to $2/(2l+1)$

$$\mathrm{var}(\widehat{C}_l) = \frac{2}{2l+1} C_l^2 \ . \tag{48}$$

Since this does not couple different multipoles it is an optimal estimator [1]. The variance of the $C_l$ is referred to as cosmic variance. Once measurements are limited by cosmic variance (cosmic noise) improved instrumental sensitivity does not help.

The fact that modes of different $l$ are statistically independent follows from the assumption that the anisotropy is statistically generated by gaussian random variables. Gaussianity is not a phenomenological fact and therefore deserves further investigation. Many theories from primordial magnetic fields to inflationary models predict deviations from gaussianity [9, 18, 29, 34, 46]

### 3.1.2 Key Features of the Angular Power Spectrum

The power-spectrum as defined in equation 46 provides the fluctuation power as a function of angular scale. The angular scale corresponds very roughly with the multipole moment, $l$, as $\theta \approx 180^\circ/l$. As discussed in section 1.4 the angular size of the horizon at decoupling was roughly $1^\circ$ or $l = 200$. This is our first important benchmark scale, as only features smaller then this had time to evolve after the Big Bang. Thus, features appreciably larger (roughly $l \leq 20$) are features that are a direct probe of the initial conditions prescribing the evolution of the universe, we refer to these features as "primordial". The features smaller

| | | | |
|---|---|---|---|
| Nonrelativistic Matter | $\rho_m = ka^{-3}$ | $a \sim t^{2/3}$ | $w = 0$ |
| Relativistic Particles | $\rho_r = ka^{-4}$ | $a \sim t^{1/2}$ | $w = 1/3$ |
| Vacuum | $\rho_\Lambda = \rho_0$ | $a \sim e^{\sqrt{\Lambda/3}t}$ | $w = -1$ |

Table 2: Scale factor evolution in single component universes.

than the horizon at decoupling are acoustic oscillations of the plasma from which the CMB decoupled. The acoustic peaks give further insight with their high $l$ behavior, known as the damping tail. In the temperature power spectrum the ISW Rise and the Sachs-Wolfe Plateau dominate the large scale anisotropy [40].

### 3.1.3 Evolution of a Single Component Universe

It is often useful to consider a single component universe. That is a universe that is dominated either by radiation, matter, or dark energy. The pressure, $P$, is related to the density, $\rho$, by the paramater $w$:

$$P = w\rho c. \tag{49}$$

Using the equation of state we can determine the relationship between density and the scale factor, $a$, up to a constant, $k$, as follows:

$$\rho = \frac{k}{a^{3w+3}}. \tag{50}$$

This allows us to solve FRW solution and note the time dependence of the evolution of the universe. We find that the universe expands at a rate proportional to $t^{2/3}$ during a

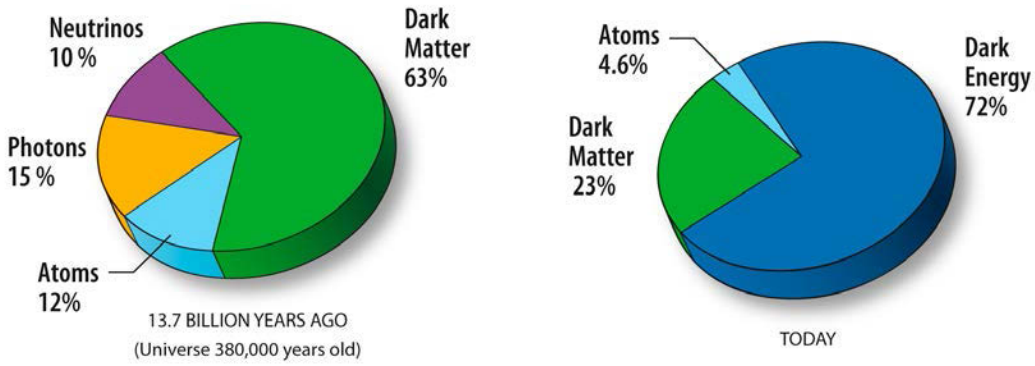


Figure 10: A summary of the energy composition of the universe, both today and at decoupling. [Courtesy of the WMAP science team]

matter dominated epoch, $t^{1/2}$ during a radiation dominated epoch, and $e^{\sqrt{\Lambda/3}t}$ during a vacuum dominated area [19, 24]. Here, $\Lambda$, is the cosmological constant. These results are summarized in table 2. This type of analysis combined with CMB data allows us to describe the energy composition of the universe at various times, see figure **??**

### 3.1.4 Acoustic Oscillations and their Damping Tail

Before the light decoupled from the ordinary matter in the universe, the existing plasma supported the propagation of sound waves [27]. To calculate the speed of sound in this primordial medium, we recall that the speed of sound, $c_s$, is the partial derivative of pressure, $P$, with respect ot density, $\rho$, at constant entropy, $s$

$$c_s^2 = c\sqrt{\left(\frac{\partial P}{\partial \rho}\right)_s}. \tag{51}$$

Note that for $w = -1$ we have $P = -\rho c^2$ and $\partial P/\partial \rho < 0$, therefore, $c_s$ is undefined. This implies that sound cannot propagate. In the density term we have to consider only contributions from ordinary matter and radiation as dark matter does not interact with radiation

$$\rho = \rho_b + \rho_r. \tag{52}$$

The pressure, $P$, is related to the the density, $\rho$, via the equation of state:

$$P = w\rho c^2. \tag{53}$$

Where $w$ is $0$ for non-relativistic particles, $1/3$ for relativistic particles including radiation, and $-1$ for a cosmological constant or dark energy. Since the dark energy component is negligible before decoupling, we find that pressure is only due to the radiation pressure

$$P = \frac{1}{3}\rho_r. \tag{54}$$

We recall from section 3.1.3 that $\rho$ can be expressed in terms of the scale factor, $a$ allowing us to express the speed of sound in terms of derivatives with respect to $a$,

$$\frac{\partial P}{\partial \rho} = \frac{\partial P}{\partial a}\frac{\partial a}{\partial \rho}. \tag{55}$$

We now have the tools needed to solve for the speed of sound in the plasma before decoupling:

$$c_s^2 = \frac{-4}{3}\frac{\rho_r}{a}\left(\frac{1}{-3\rho_b/a - 4\rho_r/a}\right) \Rightarrow c_s = \frac{c}{\sqrt{3}}\left(1 + \frac{3\rho_b}{4\rho_r}\right)^{-\frac{1}{2}}. \tag{56}$$

Since the energy density of photons dominated that of nonrelativistic baryonic matter we find that the speed of sound in the early universe was very nearly $1/\sqrt{3}$ of the speed of

light. As the universe evolves towards the matter dominated cosmology of decoupling, the speed of sound slows down as it approaches a value of $2/\sqrt{21}$ times the speed of light at the time of radiation-matter equivalence. Just like the fundamental tone in an open pipe manifests itself at $L = \lambda/2$ we find that the fundamental note of the acoustic oscillations in the primordial plasma manifest itself at a wavelength equal to half the sound horizon. Given the speed of sound, as calculated above, and the causal horizon as calculated in equation 4 we can conclude the location of the fundamental tone, or the first peak in the CMB power spectrum, as

$$\frac{2^\circ}{2} \approx 1^\circ. \tag{57}$$

With a sensitive measurement of the location of the first acoustic peak we can deduce the sound horizon. As we have seen the sound horizon depends on the ratio of the baryonic energy density to that of the radiation density. Since this is inherently an angular measurement it also depends on the curvature of the universe, and above we have assumed a flat geometry. We have just encountered the first of many cosmological degeneracies. To break this degeneracy we need to acquire more data. As the radiation dominated universe transitions into a matter dominated universe the oscillations are amplified. When this gravitational driving occurs depends on the ratio of radiation energy to that of matter. The fact that the third peak appears amplified with respect to the second, is a strong cosmological indicator that dark matter dominates baryonic matter [39].

### 3.1.5 The Sachs-Wolfe Plateau

Through gravitational redshifting, perturbations in the gravitational field, $\delta\phi$, cause temperature perturbations in the observed CMB. This is referred to as the Sachs-Wolfe effect [80] and expressed as follows:

$$\frac{\Delta T}{T} \approx \frac{1}{3}\frac{\delta_\phi}{c^2}. \tag{58}$$

We can learn about the initial conditions by studying the CMB power spectrum at scales much larger than the sound horizon, $l \ll 100$. These features did not have time to evolve and are therefore direct probes of initial conditions. The low-$l$ primordial signal is, however, in the $TT$ power spectrum dominated by the Sachs-Wolfe effect. Luckily we can find these gravitational waves, or tensor modes, by studying polarization.

## 3.2 The Need to Measure

Theories describing our universe must be tested by experiments. Having reviewed the fundamental concepts of inflation and CMB science, the following section will focus on the requirements of this generation's CMB experiments with a heavy emphasis on how CLASS rises to the challenge of testing inflation.

# 4 Observing Inflation through the CMB

To validate and guide the theory of inflation we need experiments to test its claims. This comes down to measuring the scalar and tensor power spectra. These are, however, not intrinsic quantities measured by CMB experiments. Fundamentally a CMB experiment can measure two quantities, temperature and polarization. Polarization has two degrees of freedom. In any given decomposition there will be two orthogonal polarization states. In cosmology we use a decomposition of polarization into E-modes and B-modes, two orthogonal bases for polarization. CMB experiments measure four primary power spectra, TT, EE, BB, and TE. The TB and EB power spectra are equal to zero. Details of the following discussions are from the literature [14, 39–42, 47, 49].

## 4.1 Polarization Review

To understand the impact of inflation on CMB anisotropy we have to understand how polarization anisotropy arises. A plane wave scattering off an electron creates polarized light. Specifically the cross section is polarization dependent [20], as

$$\frac{d\sigma_t}{d\Omega} \propto \left|\hat{\epsilon} \cdot \hat{\epsilon}'\right|^2 . \tag{59}$$

Where $\hat{\epsilon}$ and $\hat{\epsilon}'$ are the incident and scattered polarization directions. The electron oscillates in the plane defined by the incident plane wave. Unpolarized light will produce polarized light as seen by the observer, only if the incident light is not isotropic, see figure 11. If the incident light is isotropic all polarization states are equally distributed thus the observer

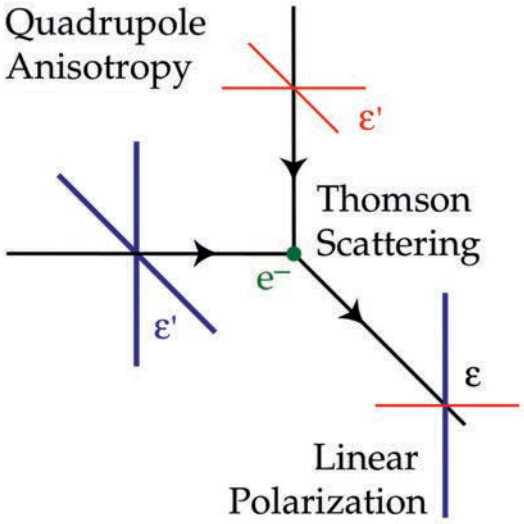


Figure 11: A quadrupole anisotropy in the temperature background produces polarized light via Thomson Scattering. The difference in intensity results in a net linear polarization. Image taken from [42].

would measure unpolarized light.

With this we note that a quadrupole temperature anisotropy is necessary to produce a net-polarized scattered light emission. The polarization created before decoupling underwent many successive scatterings, thus re-randomizing the polarization vector. Therefore the polarization we observe reflects the quadrupolar temperature fluctuations at the surface of last scattering [42].

In the following sections we will derive the scalar and tensor perturbations by considering an ensemble of Thomson scattering events. Note we skip over vector perturbations as these are predicted to be negligible, see section 2.2. We find it consistent with our treatment

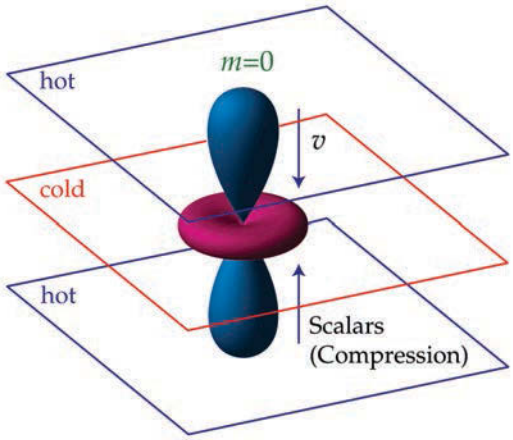


Figure 12: Scalar perturbations arise from over, and under-dense regions. Image taken from [42].

in section 2.2 while showing consistency with the helicity relations for the various modes.

### 4.1.1 Scalar

The density perturbations, those responsible for structure formation via gravitational instability, are scalar perturbations of the metric. Since the early universe was filled with a relativistic plasma both pressure and gravity source the "force" term in the equations of motions. Initially the plasma flows from over-dense to under-dense regions. Or more precisely the plasma always moves from hotter effective temperature to lower effective temperature. The photons that reach us from these potential troughs are red shifted as they climb out of the gravitational well. This effect is depicted in figure 12. The temperature perturbation that is created in this manner takes the form of a quadrupole with helicity $m = 0$. Of course the polarization sense depends on the angle at which the quadrupole is observed.

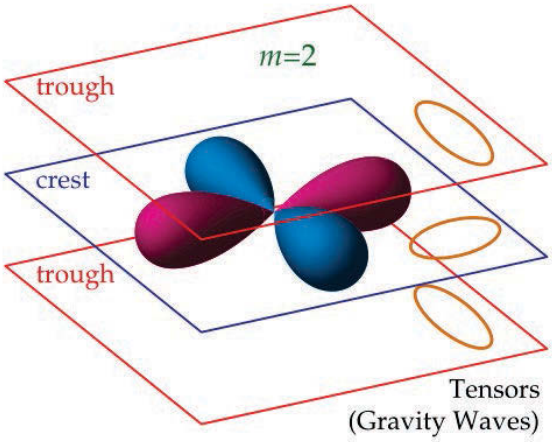


Figure 13: Gravitational waves create quadrupolar anisotropy as the gravitational wave alternatively red and blue-shifts the photons. Image taken from [42].

### 4.1.2 Tensor

Gravitational waves are tensor perturbations. Gravitational waves stretch space in perpendicular directions at a trough and crest of the wave. Geometrically a circle would be squeezed into an ellipse. This has the effect of red-shifting the component being stretched and blue shifting the perpendicular axis, being compressed. The resulting patterning is again a quadrupole anisotropy with helicity $m = \pm 2$.

## 4.2 The E and B Mode Decomposition

Previously we discussed the polarization patterns for a single plane wave perturbation. The polarization patterns on the sky do not cleanly break into $m = 0, \pm 1, \pm 2$ due to the fact that a spectrum of fluctuations each with a different wave vector will exist. It is important

to note, however, that the parity and correlation with temperature fluctuations survive the superposition [42]. These global polarization patterns can be separated into E and B-modes

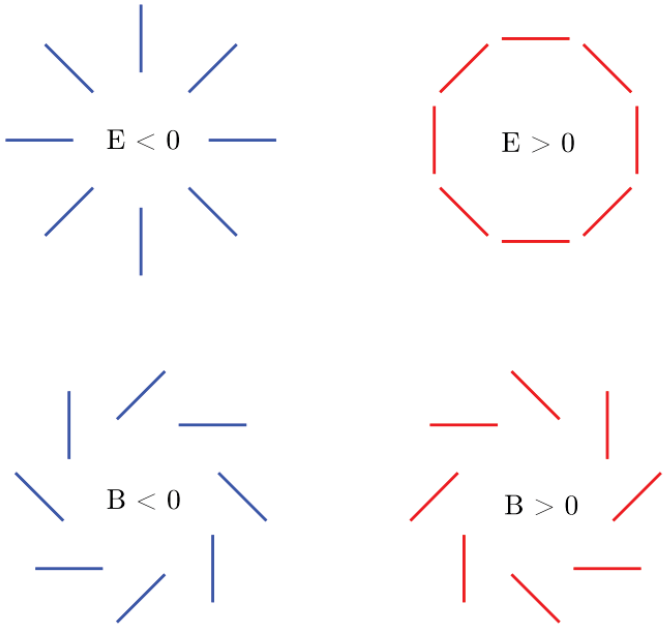


Figure 14: Any polarization field can be described by E and B-modes. Their distinguishing characteristic is that B-modes are divergence-free while E-modes are curl-free [49].

where an E-mode has $(-1)^l$ parity and a B-mode has $(-1)^{l+1}$ parity. Since the spherical harmonics that describe the temperature anisotropies have $(-1)^l$ parity, Thomson scattering can only produce E-modes locally. To understand the source of B-modes on the sky we consider a plane wave modulation of the surface of last scattering. This modulation generates a B-mode from a superposition of local quadrupole anisotropies.

Both scalar and tensor perturbations can generate E-modes, but only tensor perturba-

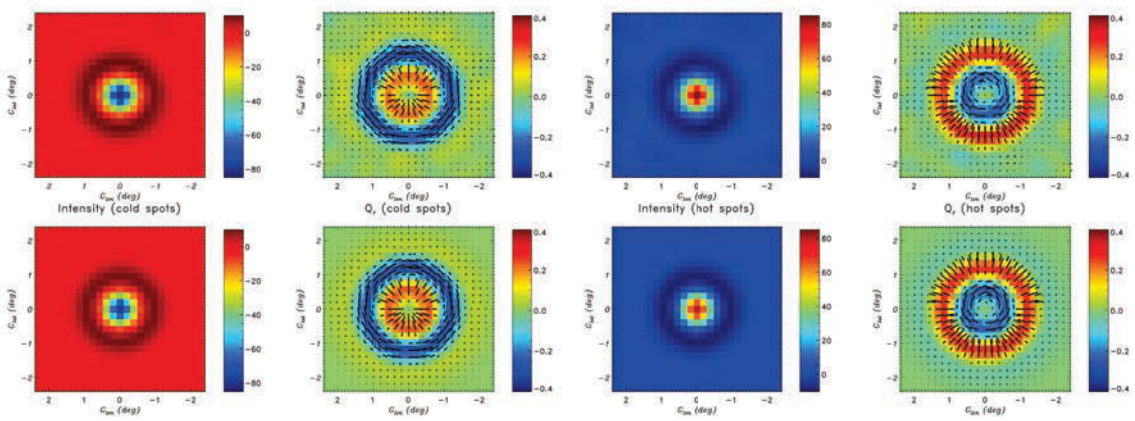


Figure 15: Stacked maps of degree sized cold (left) and hot (right) spots from the Planck Data. The first row shows observations while the second shows simulations. [69]

tions can generate B-modes. We expect similar contribution to the E-mode and B-mode power spectra from tensor perturbations at low-$l$, and finally we also expect the E-Modes to be correlated with the temperature power spectrum.

### 4.2.1 Planck Data

The Planck spaceborne-experiment was launched in May 2009 by the European Space Agency. It is a higher resolution follow-up to WMAP. Planck also achieves significantly higher signal to noise than does WMAP. Figure 15 shows hot and cold spots of one degree size from the Planck data. The high level of signal to noise was achieved by stacking independent hot and cold spots on top of each other. The $E$-mode polarization pattern is clearly visible, we also see that the polarization perturbations occur at twice the frequency,

in Fourier space, compared to the temperature fluctuations, and they are anti-correlated.

Planck has provided high resolution full sky maps of polarized foregrounds such as dust and synchrotron emission [68]. These foreground maps can and are used by other experiments to clean their CMB observations. Planck has also provided an improved test of gaussianity. The latest analysis by Planck is still consistent adiabatic, gaussian, primordial seeds [70]. The best limits on $r$ from B-mode measurements currently come from the joint analysis of BICEP2 and Planck data, in the form of an upper limit, $r < 0.09$ [11].

# Part II

# Measuring Inflation with CLASS

# 5 Review

In section 2.2 we learned that understanding inflation boils down to understanding the mechanism, or inflaton field, driving inflation. Given the current experimental constraints the possible theoretical models are endless[1]. Thankfully we have learned that we can characterize inflation via the scalar and tensor amplitude, the scalar and tensor index, and the scalar running. These parameters all relate to various derivatives of the inflaton field. By calculating these derivatives we can then reconstruct the shape of the inflaton field via a Taylor expansion. A summary of the standard variables is presented in table 3. I have chosen to leave out other variables such as curvature and non-gaussianity. Let us now explore what measurements a modern polarization experiment can be designed to be sensitive to.

[1] "Examples of some inflationary models are: eternal inflation, hybrid inflation, chaotic, Ghost inflation, Tilted Ghost inflation, DBI inflation, brane inflation, N-flation, bubble inflation, extended inflation, false vacuum inflation, power law inflation, k-inflation, hyperextended inflation, supersymmetric inflation, Quintessential inflation, Natural inflation, Super inflation, Supernatural inflation, D-term inflation, B -inflation, Thermal inflation, discrete inflation, Assisted inflation, Polar cap inflation, Open inflation, Topological inflation, Double inflation, Multiple inflation, Induced-gravity inflation, Warm inflation, stochastic inflation, Generalized assisted inflation, self-sustained inflation, Graduated inflation, Local inflation, Singular inflation, Slinky inflation, locked inflation, Elastic inflation, Mixed inflation, Phantom inflation, Boundary inflation, Non-commutative inflation, Tachyonic inflation, Tsunami inflation, Lambda inflation, Steep inflation, Oscillating inflation, Mutated Hybrid inflation, intermediate inflation, Inhomogeneous inflation" [81]. The need to constrain theory is immediate.

| Label | Definition | Physical Origin |
|---|---|---|
| $A_s$ | Scalar Amplitude | $V$, $V'$ |
| $n_s$ | Scalar Index | $V'$, $V''$ |
| $\alpha_s$ | Scalar Running | $V'$, $V''$, $V'''$ |
| $A_t$ | Tensor Amplitude | $V$ |
| $n_t$ | Tensor Index | $V'$ |
| $r$ | Tensor-to-Scalar Ratio | $V'$ |

Table 3: A summary of the parameters of inflation and how they relate to the physical properties of the Inflaton field. $V'$, $V''$, and $V'''$ refer to the first, second, and third derivative of the potential. This summary is taken from [7].

## 5.1 Predictions

Since the scalar power spectrum is known, the energy at which inflation occurred is dependent only on the tensor-to-scalar ratio, under the slow-roll approximation

$$V = \frac{3}{2}\pi^2 A_s r M_{Pl}^4 = (1.94 \times 10^{16}\ \mathrm{GeV})^4 \frac{r}{0.12}\ . \tag{60}$$

F Figure 16 shows the current constrains on $r$ and $n_s$ with predictions of various chaotic inflationary potentials, including the $R^2$ potential. The current data supports the predictions of minimal inflation, that is single-field slow-roll Inflation predicts $n_s < 1$, undetectable spectral running, and undetectable non-Gaussianity [15]. While this is a great step forward we have not been able to signficantly constrain the inflaton field since WMAP. While the current data has positively excluded the simple $\phi^4$ potential and the Harrison-Zel'dovich scale invariant inflation, much work is needed to better understand inflation. Planck decreased the upper bound on $r$ only slightly relative to WMAP, since the temperature measurements were already largely cosmic variance limited. This shows that a modern polarization experiment expressly focused on measuring $r$ is needed to make significant head-way in understanding inflation.

## 5.2 Measuring the Tensor-to-Scalar Ratio

The strongest probe of the tensor-to-scalar ratio is the $BB$ power spectrum. As shown in figure 17 many experiments have made upper limit constrains on $r$ [8, 11, 13, 17, 53, 62, 71]. Most of the experiments, BICEP2 included, did not have surveys with enough sky coverage

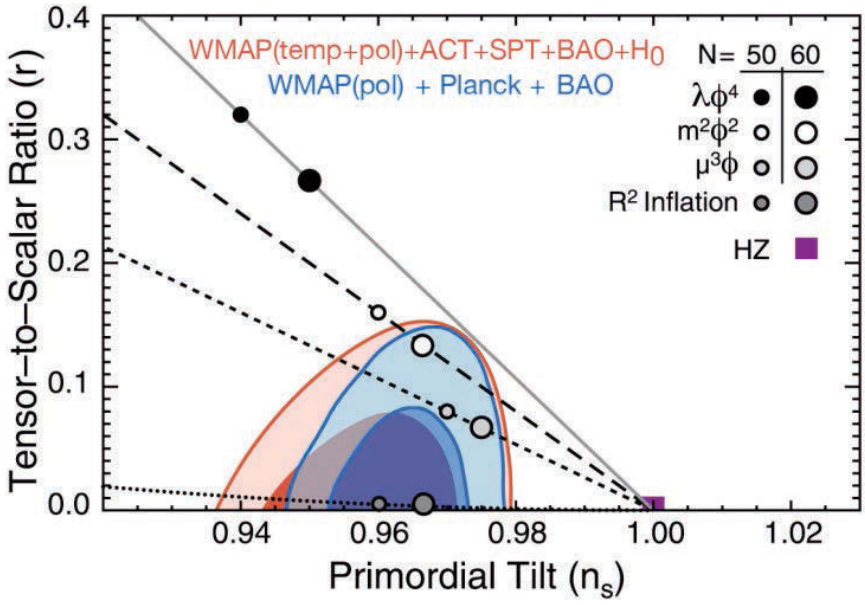


Figure 16: The WMAP (red) and Planck (blue) likelihood contours are show at $68\%$ and $95\%$ confidence level. The predictions of several minimal inflationary models is plotted for inflation lasting for $50$ to $60$ $e$-foldings. The simple $\phi^4$ potential is clearly excluded by this data, however, to make further significant progress $r$ has to be more strongly constrained. [Image courtesy of the WMAP science team.]

to capture the re-ionization bump. It is, however, precisely the low-$l$ which offer the highest signal-to-noise per multipole. Therefore, low-$l$ detections of primordial gravitational waves are more promising than partial sky surveys such as BICEP2. Although BICEP2 did not measure $r$ it's data combined with Planck data still presents the lowest upper limit on the tensor-to-scalar ratio measured by polarization of $r < 0.09$.

To measure $r$ the ideal experiment will be designed to include low-$l$ polarization sensitivity. This low-$l$ sensitivity implies a need for a nearly full sky survey. And the necessary

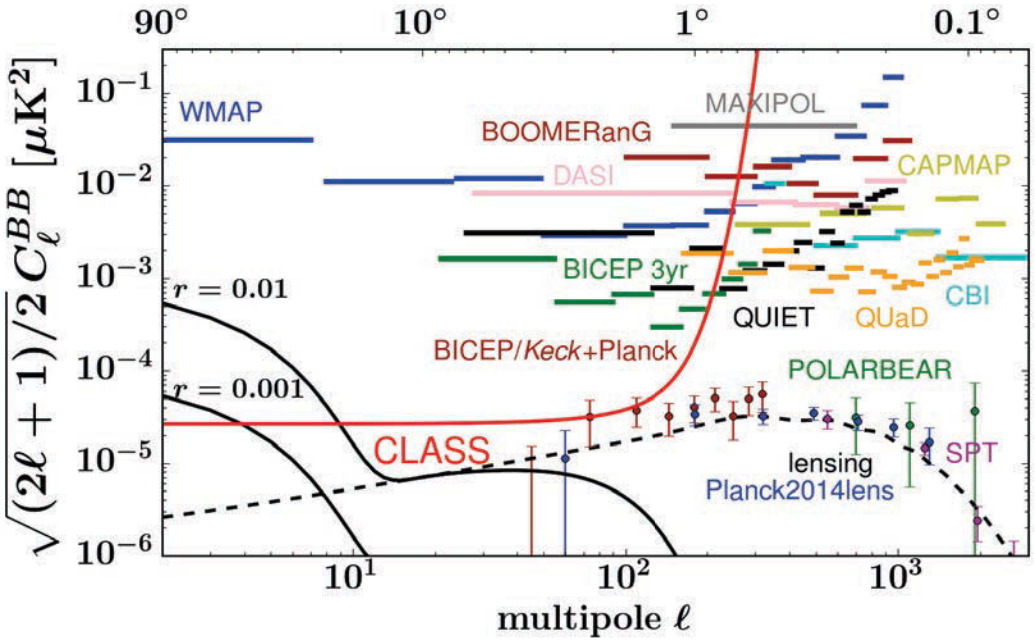


Figure 17: The B-mode power spectrum is plotted for $r = .01$ and $r = .001$. The re-ionization bump is evident at $l < 10$. So far experiments have only been able to place upper limits on the B-mode amplitude. [Courtesy of Prof. Bennett and Prof. Marriage.]

detector sensitivity requires state of the art cryogenic detectors. These are significant challenges. A ground based experiment will pick up the additional responsibility of correcting for atmospheric variations. A telescope with near full sky coverage, unprecedented sensitivity, immunity to the atmosphere, and ability to constrain foregrounds will be necessary to make a measurement of $r$ in the near future.

# 6 CLASS Approach

CLASS is designed to place an upper limit of $r < 0.008$ if $r = 0$ and detect $r = 0.01$ with $95\%$ confidence. CLASS is designed for low-$ell$ sensitivity and the ability to discern foregrounds from primordial gravitational wave signals. CLASS is designed using a modulation technique to reject systematics and atmospheric drifts, see section 7.0.2 for details. CLASS is able to constrain foregrounds (i.e. polarized dust and synchrotron) using four independent frequency bands, $40$ GHz, $90$ GHz, and $150$ GHz and $220$ GHz. This will allow CLASS to detect $r \approx 0.01$ within roughly three to five years of integrated observations [30].

## 6.1 Designing for Low-$\ell$ Sensitivity

Low-$\ell$ sensitivity requires maximum sky-coverage. This places a fundamental limit on the location of the experiment. I will briefly explore the topics of choosing a site location and an optimal scan strategy with the goal of optimizing low-$\ell$ sensitivity.

### 6.1.1 Location

After Penzias and Wilson's discovery of the CMB, the slew of experiments attempting to measure the anisotropy soon learned that the atmosphere would pose a significant challenge. Just as clouds interfere with our view of the stars, they interfere with CMB experiments of all kinds. More precisely it is the water vapor in the atmosphere that causes the most problem. COBE, WMAP, and Planck short-circuit this problem entirely by launching into space. CLASS, not having the luxury of outer space has to find a location that has low

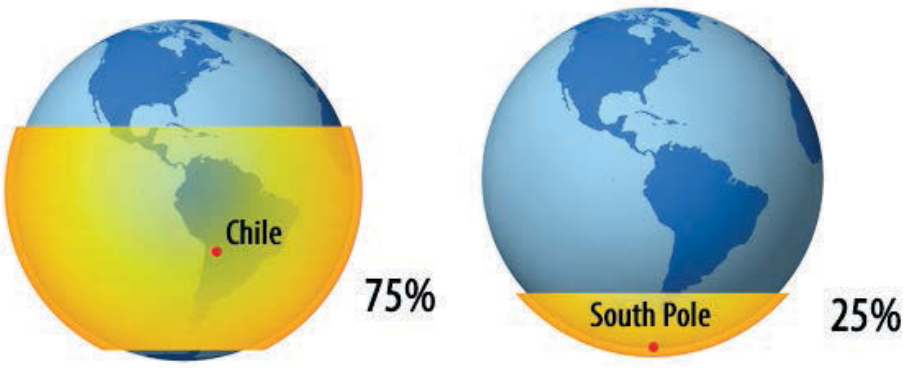


Figure 18: Two classical locations for astronomical observatories are the Atacama desert in Chile and the South Pole. Both of these locations satisfy the requirement of having very low water vapor in the atmosphere, thus providing a very clear view of the sky. They differ, however, drastically in the fraction of the sky that can be observed. An observatory in Chile can cover $75\%$ of the sky versus only $25\%$ at the South Pole. An experiment optimized for low-$ell$ sensitivity will choose to maximize sky-coverage and locate in Chile. Figure take from [45]

levels of water vapor in the atmosphere. Very cold places are typically an ideal location as the water in the atmosphere freezes out. Additionally very high places also offer the added benefit of a less dense atmosphere. The two most popular locations for ground based CMB experiments are the Chilean Atacama desert and the South Pole. Although the atmospheric fluctuations are roughly three times lower at the South Pole, this is not major consideration for CLASS. Since CLASS is a polarized experiment, and the atmosphere is not polarized, an improvement in atmospheric conditions is not as valuable as increased sky coverage.

We can calculate the sky coverage, $f_{sky}$ as a fraction of the total sky. This is a relatively

simply calculation based on the latitude, $\phi$ the experiment is located

$$f_{sky} = \frac{\cos(\alpha + \phi) + 1}{2} \,. \tag{61}$$

With $\alpha$, we also take into account the fact that experiments can not point all the way down to the horizon. In this notation $\alpha$ is a positive angle measured from the horizon and $\phi$ is the latitude with respect to the South Pole. Typically telescopes do not point less then $30^\circ$ above the horizon. The sky coverage at the south pole, $f_{sky}^{sp}$ is equal to $25\%$ and the sky covered in Chile, $f_{sky}^{c}$ is $75\%$.

$$f_{sky}^{sp} = \frac{\cos(30^\circ + 90^\circ) + 1}{2} = .25 \qquad \text{and} \qquad f_{sky}^{c} = \frac{\cos(30^\circ + 30^\circ) + 1}{2} = 75\% \tag{62}$$

The low-$ell$ sensitivity scales as the root of the inverse sky coverage, $1/\sqrt{f_{sky}}$. For these reason, the Atacama desert in Chile, at an altitude of $5200$ m, makes an acceptable location for CLASS.

### 6.1.2 Scan Strategy

The CLASS scan strategy is a simple constant elevation scan. The elevation axis is nominally set to $45^\circ$ above the horizon. This angle is necessary to avoid ground pickup and minimize the observed path length through the atmosphere. Holding the elevation constant, the telescope simply scans $360^\circ$ back and forth on an azimuthal axis. The effect of this scan is to draw out a circle on the sky. CLASS will observe the entire sky by simply allowing the sky to move through these scans. A Mollweide projection, in equatorial coordinates, is shown in figure 19 to illustrate this concept.

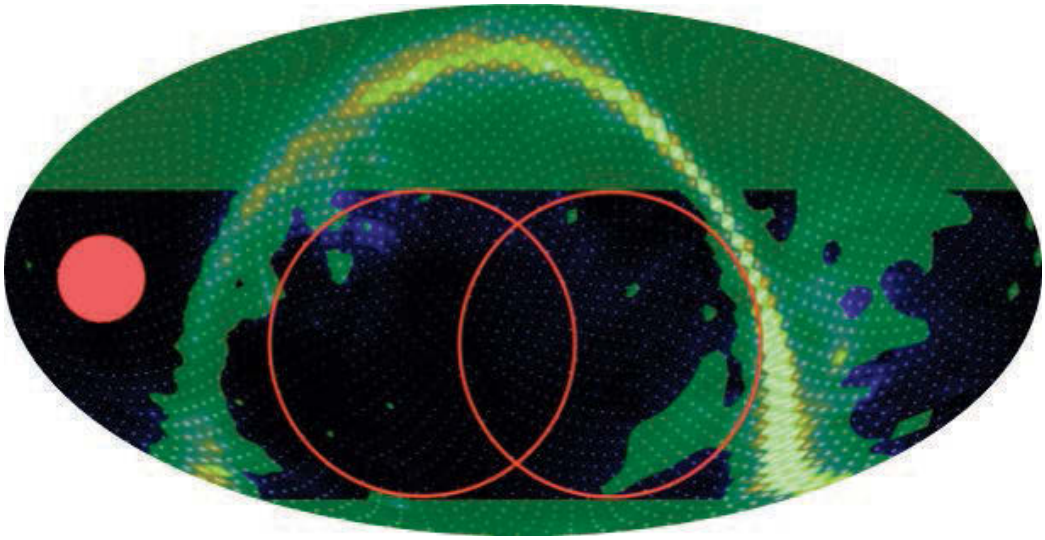

Figure 19: The CLASS scan strategy traces out a circle in the sky. Several hours later that circle will have moved due to the rotation of the earth. The filled red circle to the left shows the size of the $40$ GHz field of view. Image taken from [30].

If we were to simply scan at a fixed velocity, we would place more weight on areas around the celestial poles then the celestial equator. To maximize sensitivity we would like to scan at a constant rate $\mathrm{deg}^2/\mathrm{sec}$, to ensure every sky pixel is integrated for an equal amount of time. To do that we have to compensate for the distortion of the coordinate grid on the sky, see section 10.3 and section 9.7.6 for more information. Therefore we scan at a constant $\mathrm{DecRate}$,

$$\mathrm{DecRate} = \cos(\mathrm{dec}) * \frac{d\,\mathrm{dec}}{dt}, \tag{63}$$

where $\mathrm{dec}$ is the declination.

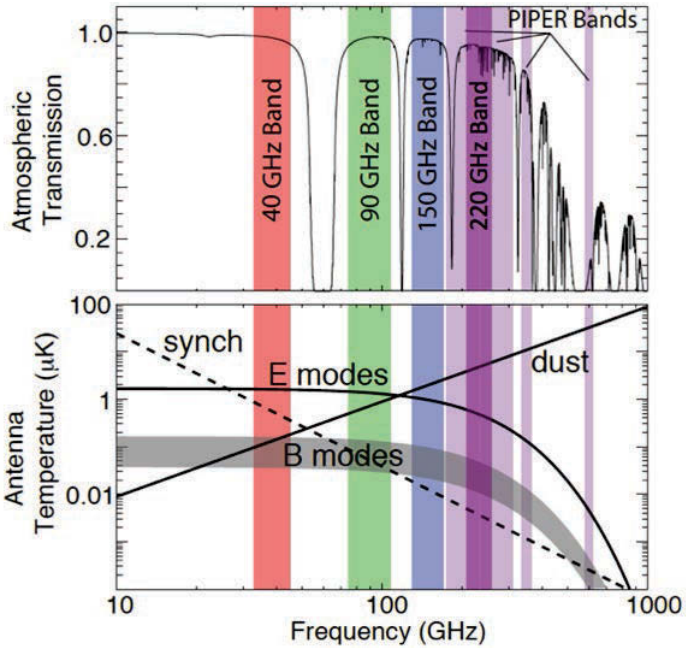


Figure 20: The top image shows the four CLASS observing bands, 40 GHz, 90 GHz, 150 GHz, and 220 GHz superimposed on a plot of the atmospheric transmission spectrum. CLASS is designed to take advantage of the transmission windows of the atmosphere. The bottom image shows the same bands with power spectra of $E$ and $B$ modes as well as those of the predominant foregrounds, synchrotron radiation and dust. [Image courtesy of Dr. Chuss and Dr. Larson.]

## 6.2 Foregrounds

The primordial B-modes are obscured by foregrounds, i.e. synchrotron radiation and thermal dust in our Milky Way galaxy. Cosmic dust produces polarization because the oblong dust particles align perpendicular with cosmic magnetic fields. This process is well understood, and reviews can be found in the literature [50]. Synchrotron radiation, arising from

helical motion of relativistic electrons about magnetic fields is also well understood and known to produce polarized signals [32, 33, 79]. As to not confuse these signals with the primordial CMB signal their contribution has to be removed. If several independent maps, at different frequencies are produced then we can take a linear combination of these maps to extract the CMB and discard the dust and synchrotron foregrounds. This is possible because the CMB will be a common signal between the thermodynamic temperature maps, while the foregrounds will be different. In the simplest method we take the maps, $X$ to be in CMB units. That is, we compute them in units where the CMB is independent of frequency. We then consider a linear composition of these maps as

$$X_{cl} = \sum_i \alpha_i X_i, \tag{64}$$

where $X_{cl}$ represents the cleaned map and $\alpha_i$ the factors in the linear combination. By requiring that the $\alpha_i$'s add up to one we ensure that the CMB is unchanged. If we now minimize this sum while fixing

$$\sum_i \alpha_i = 1 \tag{65}$$

we produce a map cleaned of foregrounds. For details for this and other foreground cleaning methods see [44].

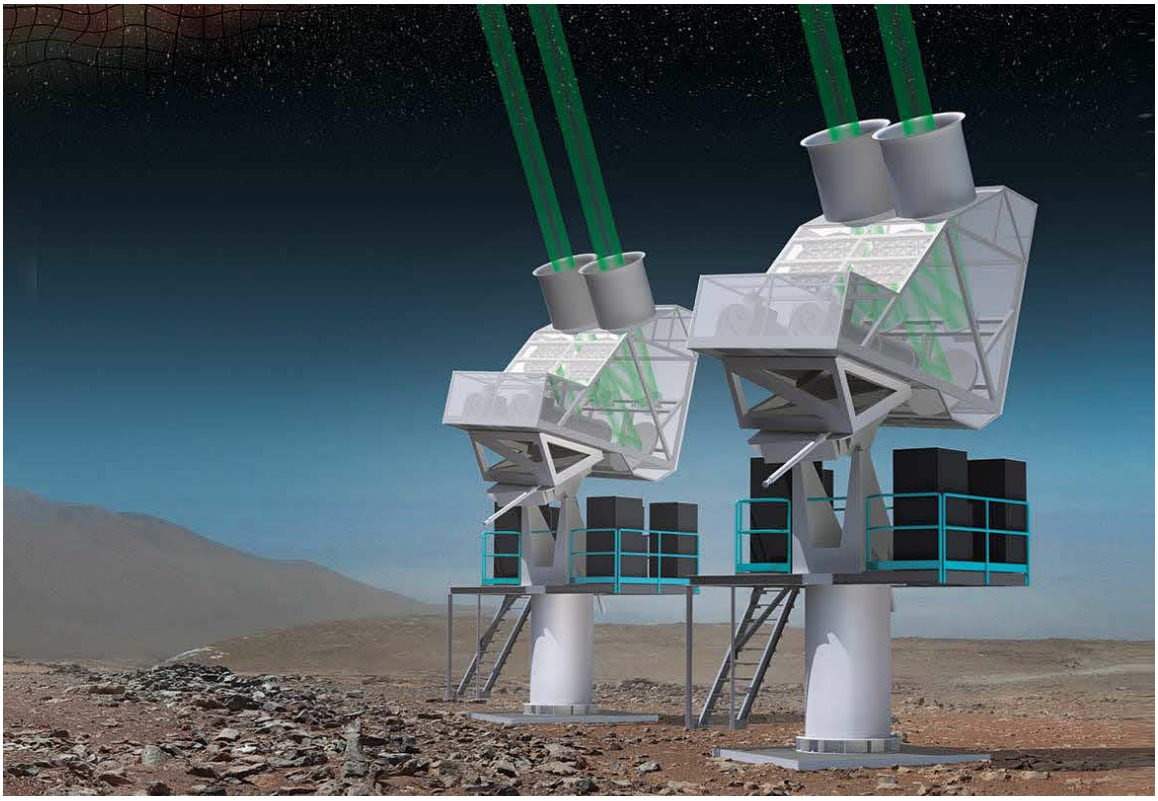

Figure 21: An artist concept of the deployed telescope. The mount, cryostat, cage, and optical elements are drawn from accurate 3D models. For visualization the optic path is shaded in green. Figure is taken from [45].

# 7 Instrument Design

In this section I will give a quick introduction into the class optical design. Starting with the CLASS modulation scheme and ending with an introduction to the CLASS detectors. To do this I will first introduce the Stokes parameters used in the analysis of our modulator, then describing the concept of the modulator before describe it's implementation. At the end of this section I will briefly discuss the entire optical path.

### 7.0.1 Stokes Parameters

For the purpose of discussing modulation in the CLASS context, describing light using the Stokes parameters, $I$, $Q$, $U$, and $V$ is a convenient parameterization. In this description $I$ represents the total intensity of the light. $Q$ and $U$ represent the linear polarized intensity of the light, where $Q$ and $U$ are $45^\circ$ rotated. Finally, $V$ represents the circularly polarized intensity. To more rigorously define this, in the context of modulation, let us recall the plane wave solution, $\Psi$ to the wave equation.

$$\Psi = E_x e^{i(kz-\omega t+\alpha_x)}\hat{x} + E_y e^{i(kz-\omega t+\alpha_y)}\hat{y} \tag{66}$$

I now use this solution to identify the Stokes parameters in terms of this plane wave.

$$\begin{aligned} I &= |E_x|^2 + |E_y|^2 \\ Q &= |E_x|^2 - |E_y|^2 \\ U &= +2\mathcal{R}(E_x E_y^*) \\ V &= -2\mathcal{I}(E_x E_y^*) \end{aligned} \tag{67}$$

### 7.0.2 The Variable Delay Polarization Modulator

The Variable delay Polarization Modulator (VPM) works on the principle of inserting a phase delay between two orthogonal linear polarization states. Light which is polarized parallel to the polarizing grid will be reflected off the grid, while light polarized perpendicular to the grid will be reflected off the mirror. We immediately see that linearly polarized light, either parallel or perpendicular to the grid is not effected by the VPM. For this rea-

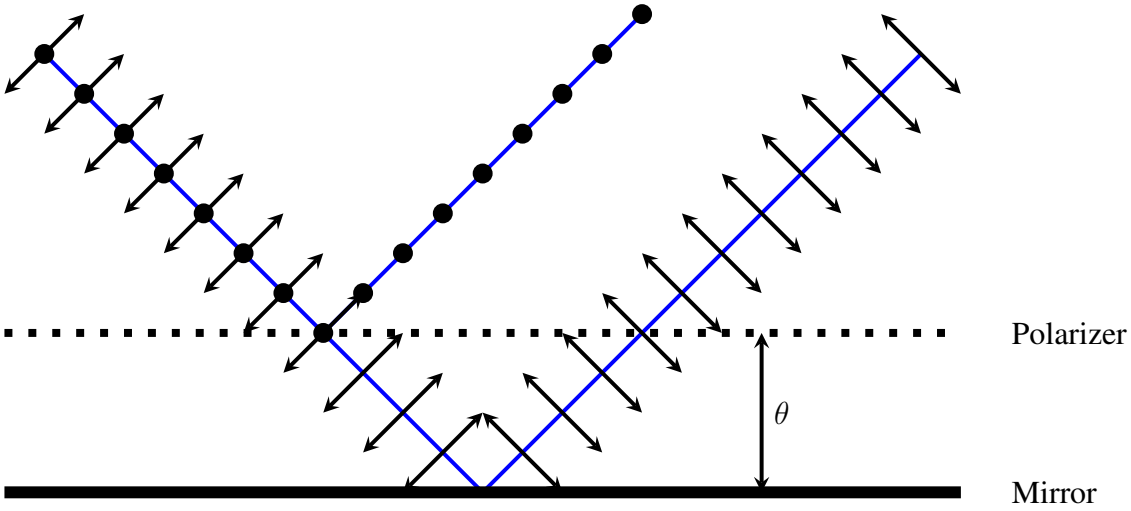


Figure 22: The VPM consists of a stationary polarizer and a movable mirror. Polarization out of the page, parallel to the polarizer axis is represented by circles, while polarization in the plane of the page, perpendicular to the polarizer is represented by arrows. The perpendicularly polarized light passes through the polarizer and picks up a phase difference of $\theta$. The phase difference is changeable by altering the position of the mirror.

son the VPM is aligned $45^\circ$ with respect to the detector axis. In this way the VPM will modulate $U$ type polarization into $V$ and vice-versa.

To understand how the VPM modulates the detector time-stream we recall the Stokes parameters and note that the $\hat{x}$ and $\hat{y}$ axis are defined by the two perpendicular antennas of the detector, and the natural VPM axis is rotated by $45^\circ$. For a more general description of interferometric polarization control see [21, 22]. We evaluate equation 67 and introduce

the phase difference, $\theta = \alpha_x - \alpha_y$

$$\begin{aligned} U &= +\sqrt{|E_x|^2|E_y|^2}\cos\theta \\ V &= -\sqrt{|E_x|^2|E_y|^2}\sin\theta\ . \end{aligned} \tag{68}$$

We see that the $I$ and $Q$ parameters remain unaffected. While both $U$ and $V$ are modulated with by the phase difference introduced by the VPM. The effect is that $U$ polarization is mapped into $V$, and $V$ into $U$. This property of the VPM makes CLASS the first experiment that will be able to map the expected circular-polarization of the atmosphere[2]. This is an important measurement as there is an expected $V$ to linear leakage in any polarimeter experiment. Thus far the circular-polarization of the atmosphere has been assumed to be negligible, however some believe it could have a significant impact on B-Mode search [31].

## 7.1 Modulator Implementation

As discussed the first optic element in the CLASS experiment is a modulator. This modulator is called the VPM (see figure 24). The VPM works on the basis of modulating the incoming light. The location, or throw, of the VPM is precisely measured by glass-slide encoders which are sample synchronously with the detectors. Later the timestreams are de-modulated. This technique is equivalent, in concept, to a lock-in amplifier. Knowing the exact frequency of the modulation we can reject $1/f$ noise. Examples of $1/f$ noise, in the CLASS context include but are not limited to atmospheric drifts and detector gain drifts.

[2]For details of how this circular-polarization arises and effects ground based CMB experiments see [37,75]

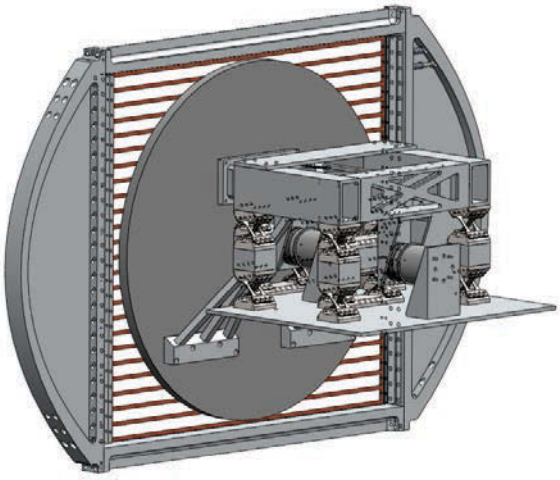

Figure 23: A 3D Model of the VPM assembly. The polarizing gird is modeled by the brown lines. It is actually the mirror that is being moved and not the polarizing grid. The mirror position is driven via a voice coil and suspended by a flexure to guarantee the mirror does not rotate out of its plane. [Courtesy of Dr. Eimer.]

## 7.2 CLASS Optical Design

The CLASS optical structure uses a primary and secondary mirror to guide the light into the a $65\ \mathrm{cm}$ HD30[3] window, for details see [26]. The cold optics consist of two HDPE lenses designed to focus on the light onto the focal plane, which uses unique smooth walled feedhorns to collect the light (see [82] for details) and couple to Transition Edge Sensor (TES) detectors (see [4] for details). The cryogenic system is covered in detail in section 8.

The detectors couple linearly polarized light, in the $x$ and $y$ direction to a pairs of Transition Edge Sensors (TES). These TESs are suspended on thermally isolated supports.

[3] A nitrogen-charged cross linked polyethylene foam.

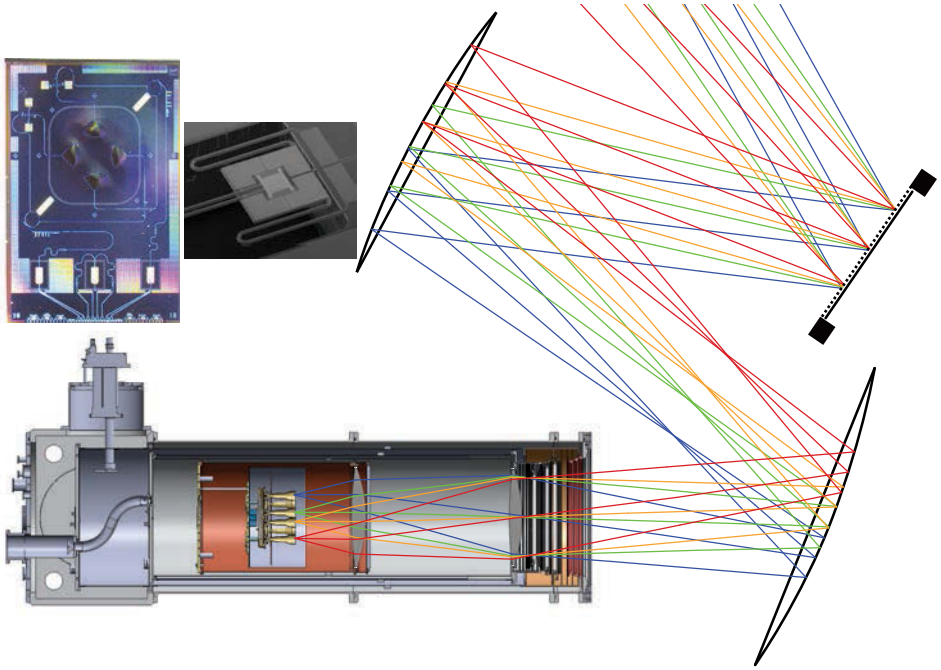

Figure 24: A 3D Model of the cryostat, the secondary and primary mirror, as well as the VPM. Additionally a microscopic view of the detectors is shown in the top left corner.. [Image courtesy of Dr. Eimer.]

When optical power couples to these detectors their nominal resistance rises. Keeping these superconducting detectors on the transition between normal and superconductivity makes their resistance highly sensitive to temperature changes, thus enabling precise measurements of incident power. These detectors are read out by applying a voltage bias and measuring the change in current through the detector via coupled superconducting quantum interference devices (SQUID).

## Part III

# Instrument Development

# 8 Cryogenics

In general low temperatures decrease the thermal noise inherent in electronics, thus increasing signal-to-noise ratios. In the case of CLASS the functioning principle of the Transition Edge Sensors relies on ultra-cold temperature. The CLASS TES sensors have to be kept at a bath temperature of $100\ \mathrm{mK}$. Traditional adiabatic demagnetization refrigerators can only maintain cryogenic temperatures for a finite time, this time is referred to as the hold-time. The Helium dilution refrigerator technology chosen for CLASS has, in principle, an unlimited hold-time. This makes the DR fridge an excellent choice for experiments needing continuous observation. I will detail the construction and modification of the cryostats used by CLASS.

## 8.1 The Dilution Refigerator

The CLASS cryogenic system employs a dilution refrigerator to achieve the $100\ \mathrm{mK}$ bath temperatures required by the detectors. The dilution refrigerator is backed by a standard Cryomech two stage pulse tube cooler. Pulse tube coolers work on the principle of compression, similar to that of a standard refrigerator, to achieve low temperatures. The working fluid in these systems is helium. Since they are closed cycle machines a supply of working fluid is not necessary. To achieve the $4.2\ \mathrm{K}$ base temperature necessary for the Dilution refrigerator to take over, a two stage pulse tube cooler is employed. The first creates a $60\ \mathrm{K}$ stage that is used by the second stage pulse tube cooler as the hot-side. The com-

bined system can achieve a base temperature of $2.8$ K and maintain a $4.2$ K temperature with up to $1.5$ W of loading.

The dilution refrigerator can operate once $4.2$ K backing temperatures are reached. A helium mixture of $^3\mathrm{He}$ and $^4\mathrm{He}$ is pre-cooled to less then $1$ K through a series of evaporative coolers. The lowest temperature is achieved by the mixing chamber, where the dilute phase and the pure phase are in equilibrium with a phase boundary separating the two. The pure phase is pure $^3\mathrm{He}$ while the dilute phase is a mixture of $^3\mathrm{He}$ and $^4\mathrm{He}$. The heat needed for the $^3\mathrm{He}$ to cross the phase boundary into the dilute phase is the source of a dilution refrigerator's cooling power. The dilute phase is pumped out of the mixing chamber by the still. The still boils off $^3\mathrm{He}$, closing the loop and recycling the $^3\mathrm{He}$. Such a system is capable of reaching temperatures as low as $2$ mK.

In practice the BlueFors[4] system, purchased for CLASS, is able to achieve a $26.0$ mK base temperature. At a $100$ mK the refrigerator achieves a $330$ $\mu$W cooling power. This is a tremendous achievement when compared with traditional adiabatic demagnetization refrigerators. The dilution refrigerator also allows CLASS to operate indefinitely long scans as there is no limit to the total cooling energy a DR can supply over time. This is an important consideration for CLASS given our scanning strategy.

[4]BlueFors Cryogenics. Copyright ©2011-2014 BlueFors Cryogenics Ltd.

## 8.2 Cryogenic Housekeeping

The CLASS experiment uses two cryogenic thermometer technologies, diodes and ruthenium oxide (ROX) resistors. Diodes make excellent temperature sensors as they offer a nearly linear temperature response. In general the voltage drop across a diode is independent, to first order, of the excitation current. The voltage drop is, however, sensitive to temperature change. This allows the diodes to exhibit robustness against variations in excitation currents. In practice, cryogenic diodes are excited at $10\ \mu\mathrm{A}$. This is in contrast to the typical $1\ \mathrm{mA}$ or $10\ \mathrm{mA}$ of room temperature sensors. The lower excitation current is necessary to present a low thermal load to the cryogenic system. The small thermal load allows diodes to be easily used on a $4\ \mathrm{K}$ stage, and possibly on a $1\ \mathrm{K}$ stage. For reference, the Lakeshore DT-670 Silicon Diode will dissipate roughly $15.8\ \mu\mathrm{W}$ of power at $4\ \mathrm{K}$. For load estimates it is convenient to use an upper limit of $20\ \mu\mathrm{W}$ per diode, this will be valid even at $1\ \mathrm{K}$.

The CLASS cryostats are able to accept ten silicon diodes on the $60\ \mathrm{K}$ stage and $14$ diodes on the $4\ \mathrm{K}$ stage. The diodes are read out over a two-wire system, instead of the more exact four-wire system. This decision was made to decrease the number of cryogenic wires, while allowing a higher number of diodes. The roughly $100\ \Omega$ round-trip resistance of the cryogenic wiring causes a $1\ \mathrm{mV}$ error. For the DT-670 diode this translates to between $30\ \mathrm{mK}$ and $50\ \mathrm{mK}$ offset error at cryogenic temperatures. This error is far lower then the calibration tolerance of industrial sensor, which is typically $500\ \mathrm{mK}$. In summary the CLASS cryostats can except $24$ single ended diode thermometers spread over the $60\ \mathrm{K}$ and

$4\ \mathrm{K}$ stage.

The lower temperature stages, $1\ \mathrm{K}$ and $100\ \mathrm{mK}$ are outfitted with more precise ruthenium oxide thermometers. The resistive element of these thermometers is a thick-film of vapor deposited ruthenium oxide. They exhibit very stable temperature behavior at room temperature. With temperature coefficients as measured in $\mathrm{ppm}$. While this makes them one of the poorest choices for room-temperature measurements, their resistance increases exponentially with low temperature. Take the Lakeshore 102A ROX as an example. At $40\ \mathrm{K}$ they begin to exhibit a temperature coefficient of roughly $1\ \Omega/\ \mathrm{K}$. By the time they reach $100\ \mathrm{mK}$ the temperature coefficient is on the order of $250\ \mathrm{k}\Omega/\ \mathrm{K}$. This behavior allows the ROX thermometers to take over operation when the diodes would no longer be an ideal choice, at $1\ \mathrm{K}$. Their properties also make them an excellent choice for very precise steering of the focal plane temperature. Relative changes of $\mu\mathrm{K}$ are detectable with high precision bridges. Typical unmatched interchangeability is specified at roughly $20\ \mathrm{mK}$ for bath temperatures relevant to CLASS $(100\ \mathrm{mK}.)$ We use a Lakeshore RX-102B-CD ROX thermometer, which has been calibrated against a NIST standard to $\pm 5\ \mathrm{mK}$ at CLASS's bath temperature to calibrate all ROX thermometers used on the focal plane. Thus we achieve consistent temperature measurements across the focal plane and across cryostats while having absolute measurements with an error as small as $\pm 5\ \mathrm{mK}$.

These types of thermometers are read out via more complicated AC excitation bridges. The AC excitation, combined with a lock-in techniques is necessary to escape the high $1/f$ and thermal noise of the resistors. Allowing precise measurement of resistance with

only $\mathrm{nA}$ bias currents. In practice the focal plane thermometers can be excited with as little as $233\,\mathrm{fW}$ of power. These AC bridges rely on Kelvin (four-wire) measurements to produce accurate and repeatable results. The CLASS cryostats are designed to accept five ruthenium oxide thermometers on the $1\ \mathrm{K}$ stage and nine ruthenium oxide thermometers on the $100\ \mathrm{mK}$ stage. These thermometers are used to measure the lens and filter temperatures as well as the focal plane temperature with built-in redundancy.

## 8.3 Details of the Cryogenic Signal Path

In this section I will give an overview of the housekeeping wiring of the CLASS cryostats. Each relevant sub-section will include a short description and detailed schematics and pinouts. This will allow the user to trace the signal path all the way from the instrument to the thermometer or other cryogenic device.

### 8.3.1 300 K Interface

The warm interface, at $300$ K, routes three $50$ pin standard density D-sub connectors and one $25$ pin standard density D-sub connectors to the a $100$ pin micro miniature D-sub and a $69$ pin micro miniature D-sub connector. These connections are established on a six layer printed circuit board (PCB) with excessive ground screening of individual signal lines. This PCB is is mounted to the lid of the Hammond 1590K box. This enclosure mounts securely to the hermetic feed through and thus the cryostat. It protects this interface from blunt force trauma. The D-sub connectors used are solid-body Conec connectors rated against IP67 intrusion of water. This combined with an IP67 seal for the 1590K box makes this interface impervious to acts of god. Figure 25 shows details of this assembly, please refer to page 76 and 77 for the schematic and PCB layout art for the $300$ K break out PCB.

### 8.3.2 Hermetic Feedthrough

The hermetic feed through was manufactured by TekData from England according to my designs. They modified a KF64 flange and potted woven copper cables through this flange.

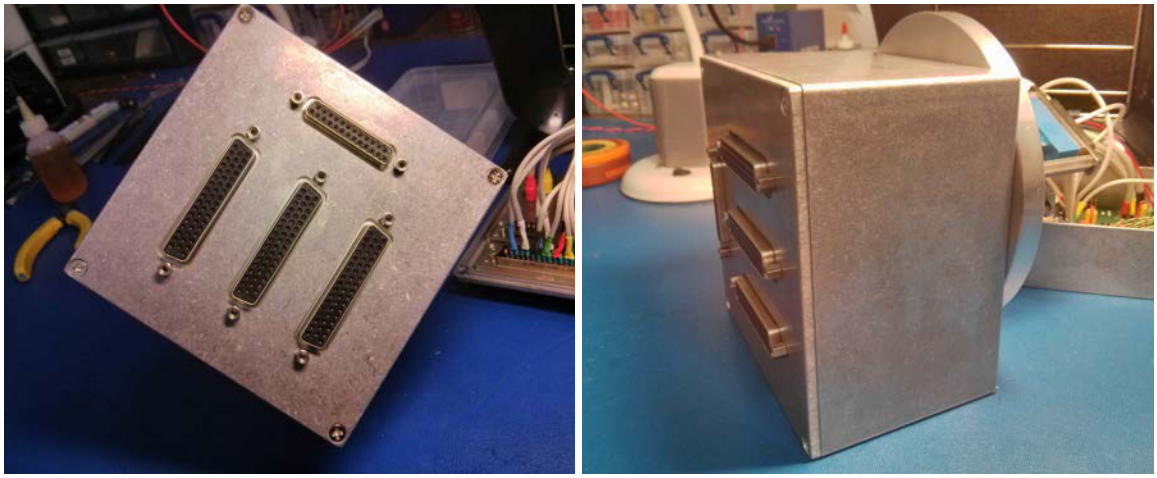

Figure 25: The left picture shows the front face of the $300$ K thermometry break out box. The $25$ pin D-sub connector, on the top-right, carries all heater signals. The first $50$ pin connector, on the top-left, carries all of the $24$ diode signals, this interfaces directly with Sleipnir. The second $50$ pin D-sub connector carries general purpose, and extra thermometry lines. This is typically not used in operation and should be covered with a shield. The last $50$ pin D-sub connector carries most of the ruthenium oxide lines, this is typically connected to the Stanford-Research-Systems[5] (SRS) breakout. The right picture shows the warm break-out-box (BOB) mated to the cryogenic feed-through.

The potting of cables through an interface provides a cheap and reliable method of manufacturing hermetic feed throughs. This flange mates with the cryostat as any KF flange would. Additionally the flange is mated to a Hammond 1590K box. The flange is now secured to the cryostat through the Hammond box. Thus, removal of the flange requires removal of the Hammond box's lid. The cryogenic MDMs are mounted to standoffs so that

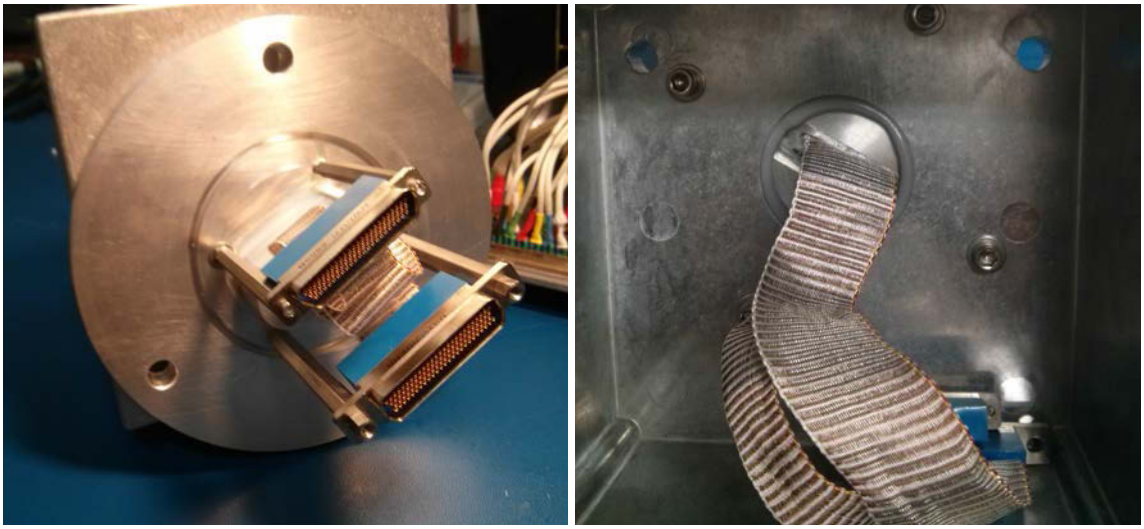

Figure 26: The left picture shows the cryogenic side of the feedthrough and how the MDMs are mounted on posts. The right picture shows details of how the Hammond box is mated to the KF flange. The weatherproofing silicone is visible at the interface.

the cryogenic connectors can be securely mounted without the weight of the connectors being suspended from the wire harnesses. A silicone sealant is used to fill the gaps between the flange and the box, to prevent intrusion of water and thus corrosion. Figure 27 shows details of this construction.

### 8.3.3 Cold Breakouts

The cold stages interconnect via TekData woven cable. The break out at each stage is accomplished via simple single inline connectors (SIP). The PCBs that were designed to accomplish this task are light tight and well heat-sunk to their respective stages, hence

Figure 27: The 60 K cold break out board. The left picture shows the side facing the 4 K stage. Signals to the colder stages continue on MDM wire harnesses while the 60 K signals are broken out on SIP connectors. The right image shows the connectors bridging the 60 K shield. When the shield is removed for service these connections have to be broken. To facilitate easy reconnection the connectors are color coded and the polarity is marked.

providing a heatsink for the cable harnesses.

- All 60 K connections are mapped through the cryostat to the warm break out on page 84.
- All 4 K connections are mapped through the cryostat to the warm break out on page 85.
- All 1 K connections are mapped through the cryostat to the warm break out on page

86.

- All $100\ \mathrm{mK}$ connections are mapped through the cryostat to the warm break out on page 87.

### 8.3.4 SRS Break-Out-Box

| Thermometer | SRS Chann |
|---|---|
| 1K ROX 1 | Chann 1 |
| 1K ROX 2 | Chann 2 |
| 1K ROX 3 | Chann 3 |
| 1K ROX 4 | Chann 4 |
| .1K ROX 1 | Chann 5 |
| .1K ROX 2 | Chann 6 |
| .1K ROX 3 | Chann 7 |
| .1K ROX 4 | Chann 8 |

Table 4: SRS BoB channell mapping.

The SRS BoB breaks out ten ruthenium oxides to interface with SRS equipment. Four thermometers from both the $1\mathrm{K}$ an $100\mathrm{mK}$ stages are broken out to the SRS Octacl Four Wire Multiplexer (SIM925) according to table 4. Additionally, the $100\ \mathrm{mK}$ ROX located on lines five and six are broken out onto separate nine-pin D-subs, PID1 and PID2 respectively.

This is intended to interface directly with the SRS AC Resistance Bridge (SIM921), used for fast control with the SRS Analog PID Controller (SIM960). PID2 is meant as a backup thermometer in case Thermometer 5 should fail. In the case of a failure one must manually switch the cable to the other connector. This prevents one from having to open the cryostat.

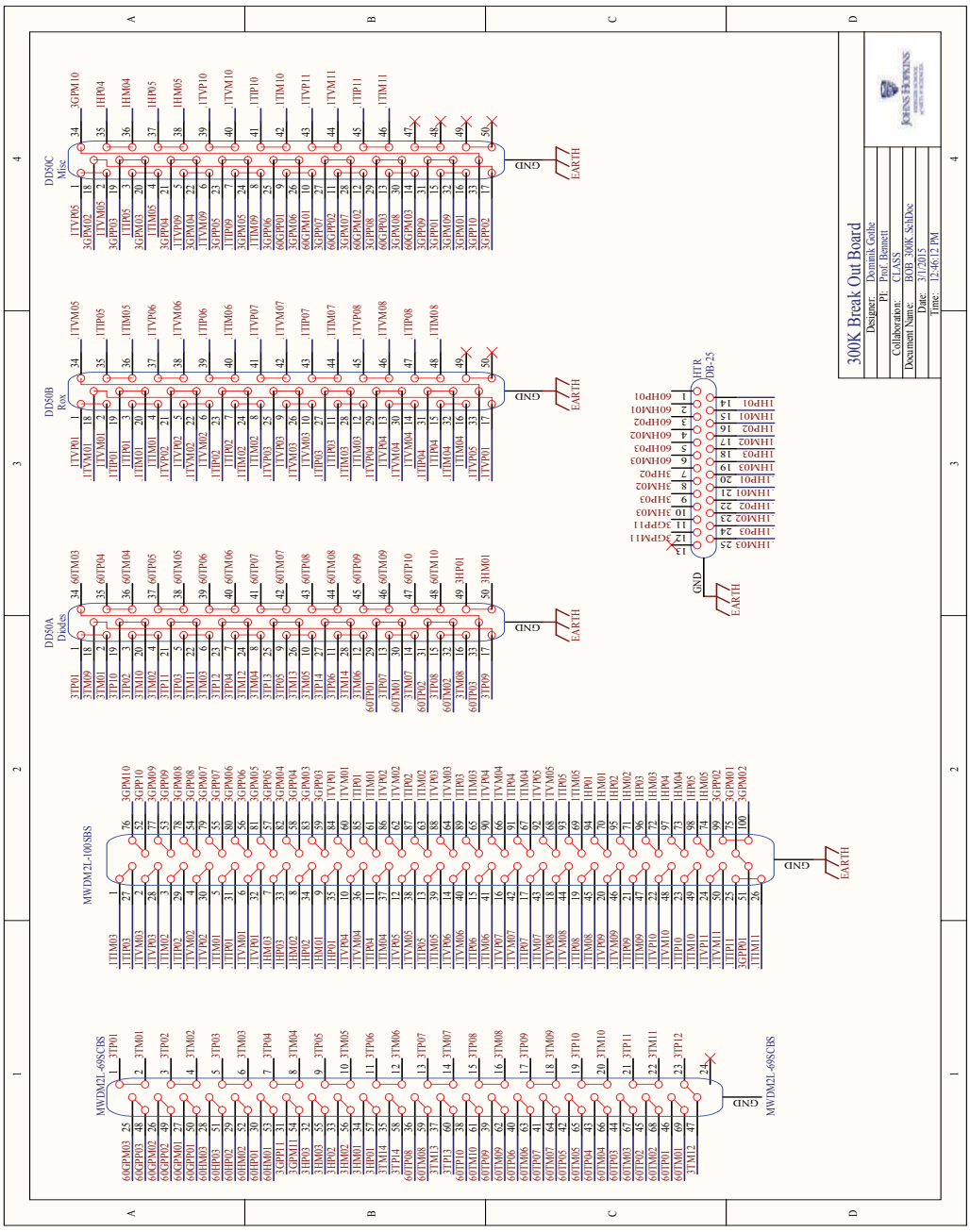


Figure 28: A schematic representation of the 300K break-out-board wiring.

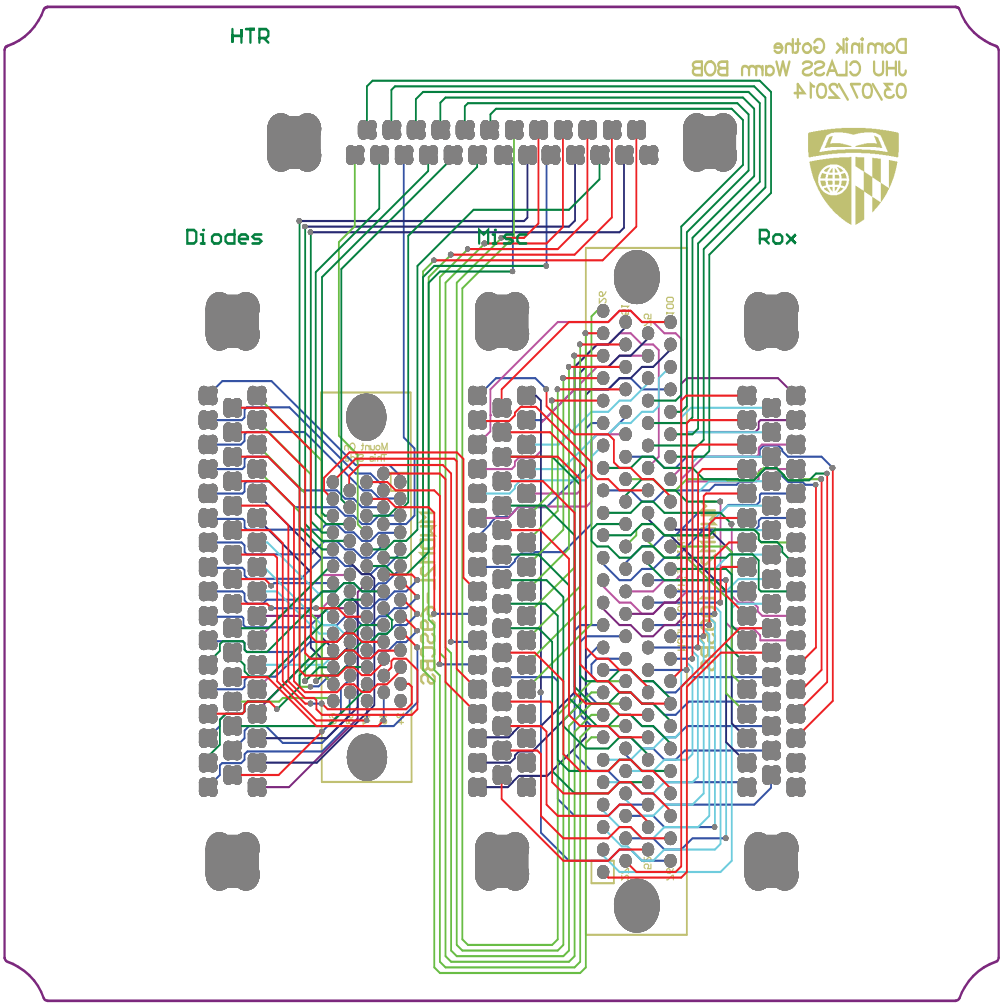


Figure 29: A flattened view of the 300K break-out-board PCB-layout.

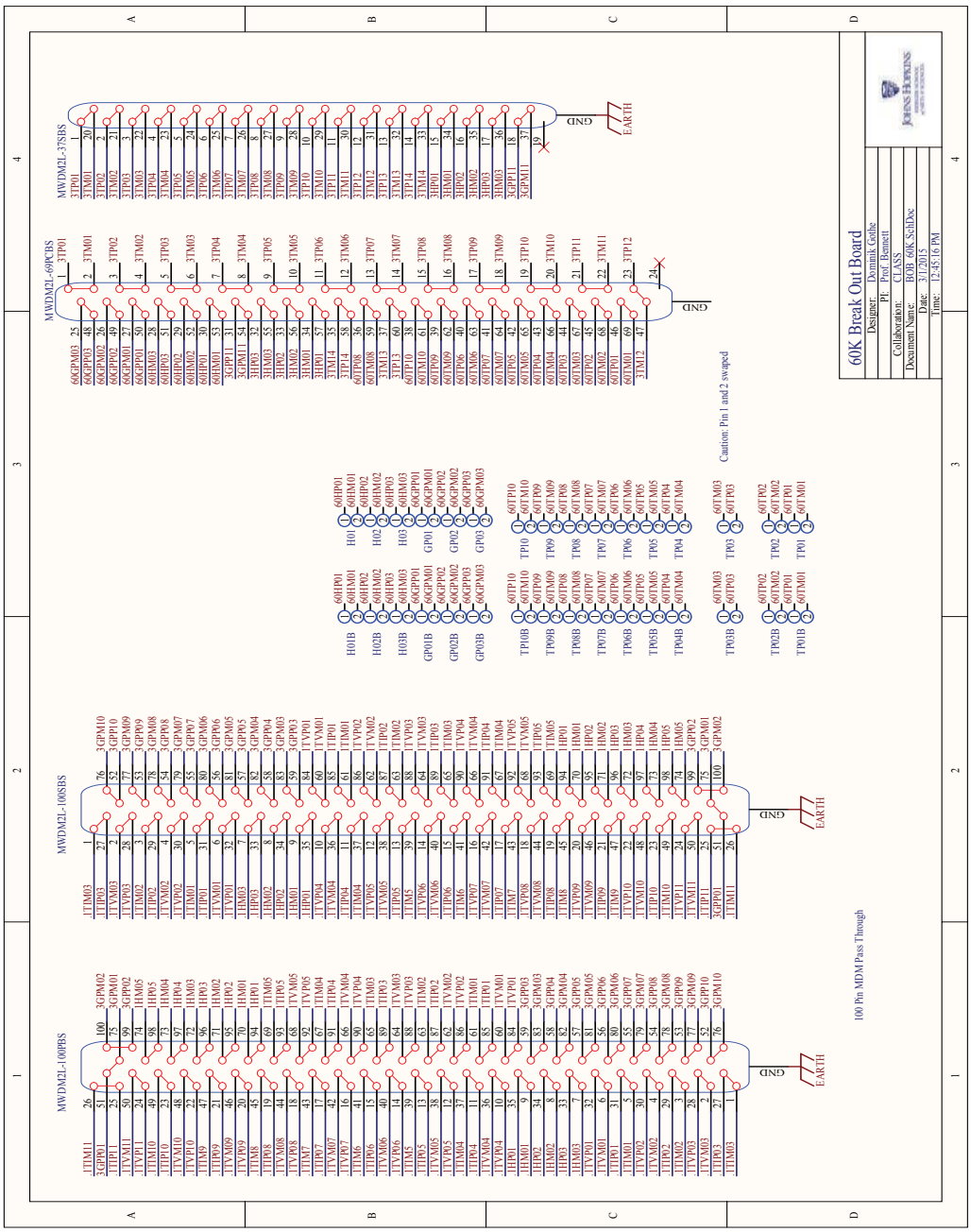


Figure 30: A schematic representation of the 60K break-out-board wiring.

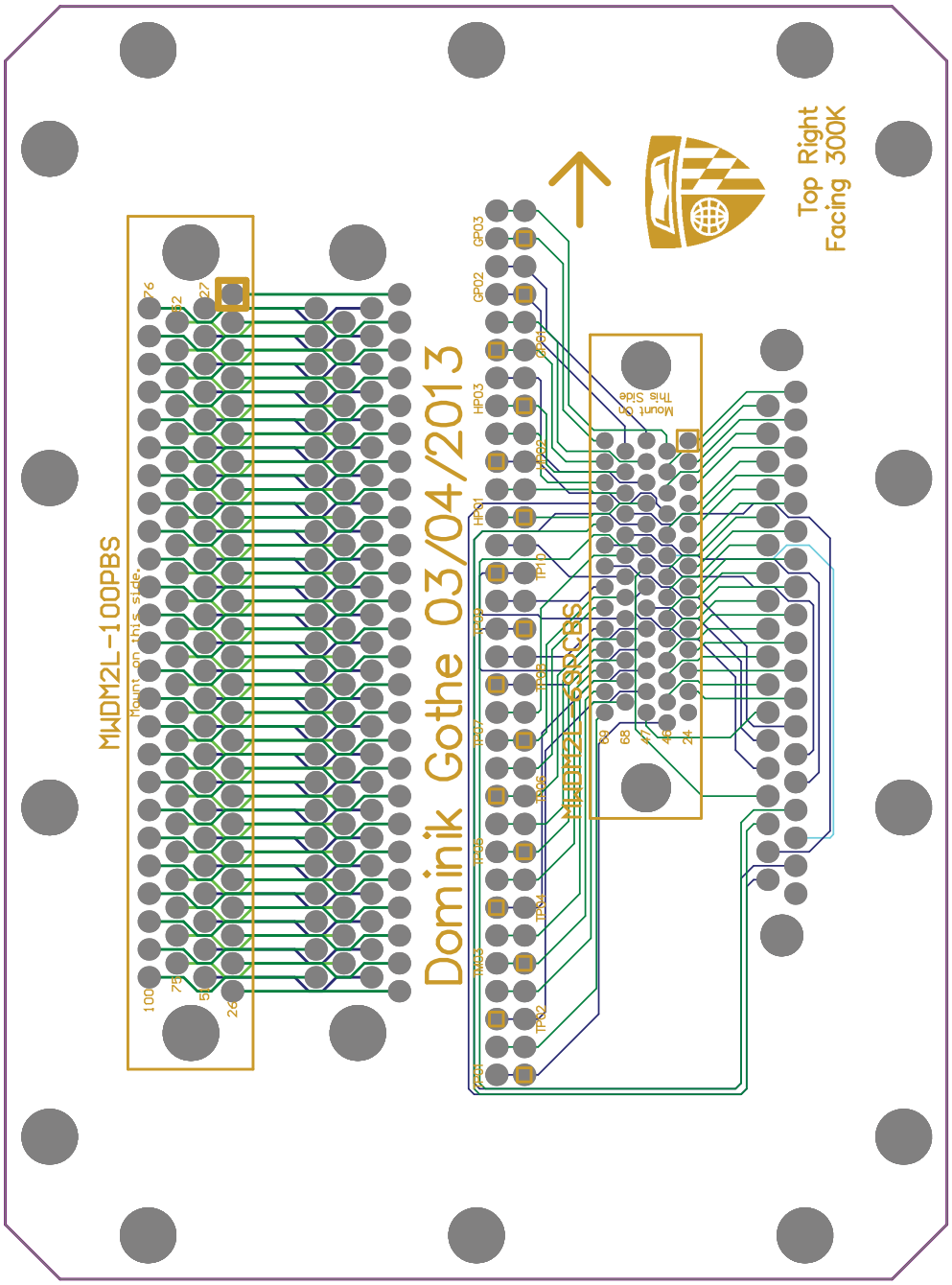


Figure 31: A flattened view of the 60K break-out-board PCB-layout.

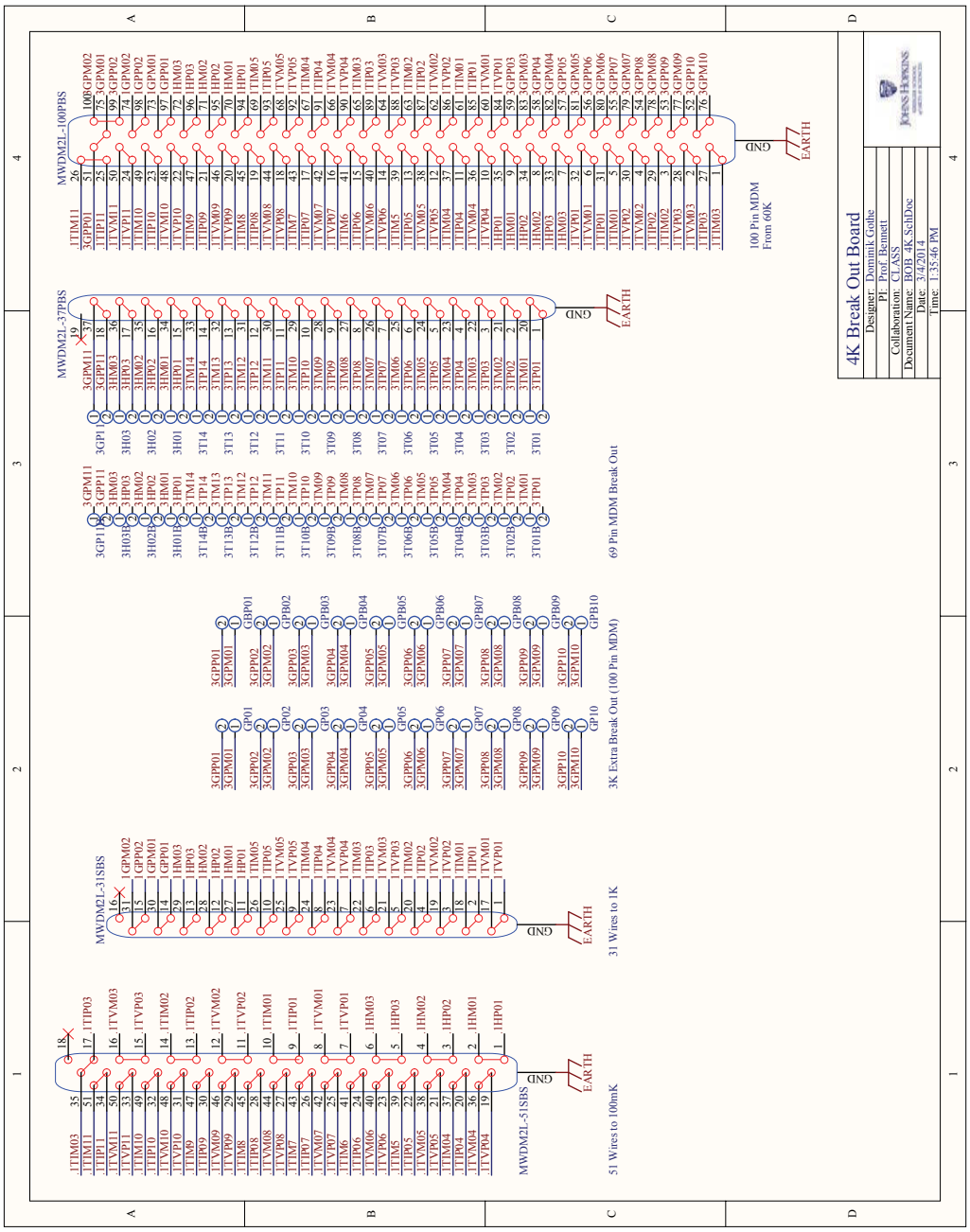


Figure 32: A schematic representation of the 4K break-out-board wiring.

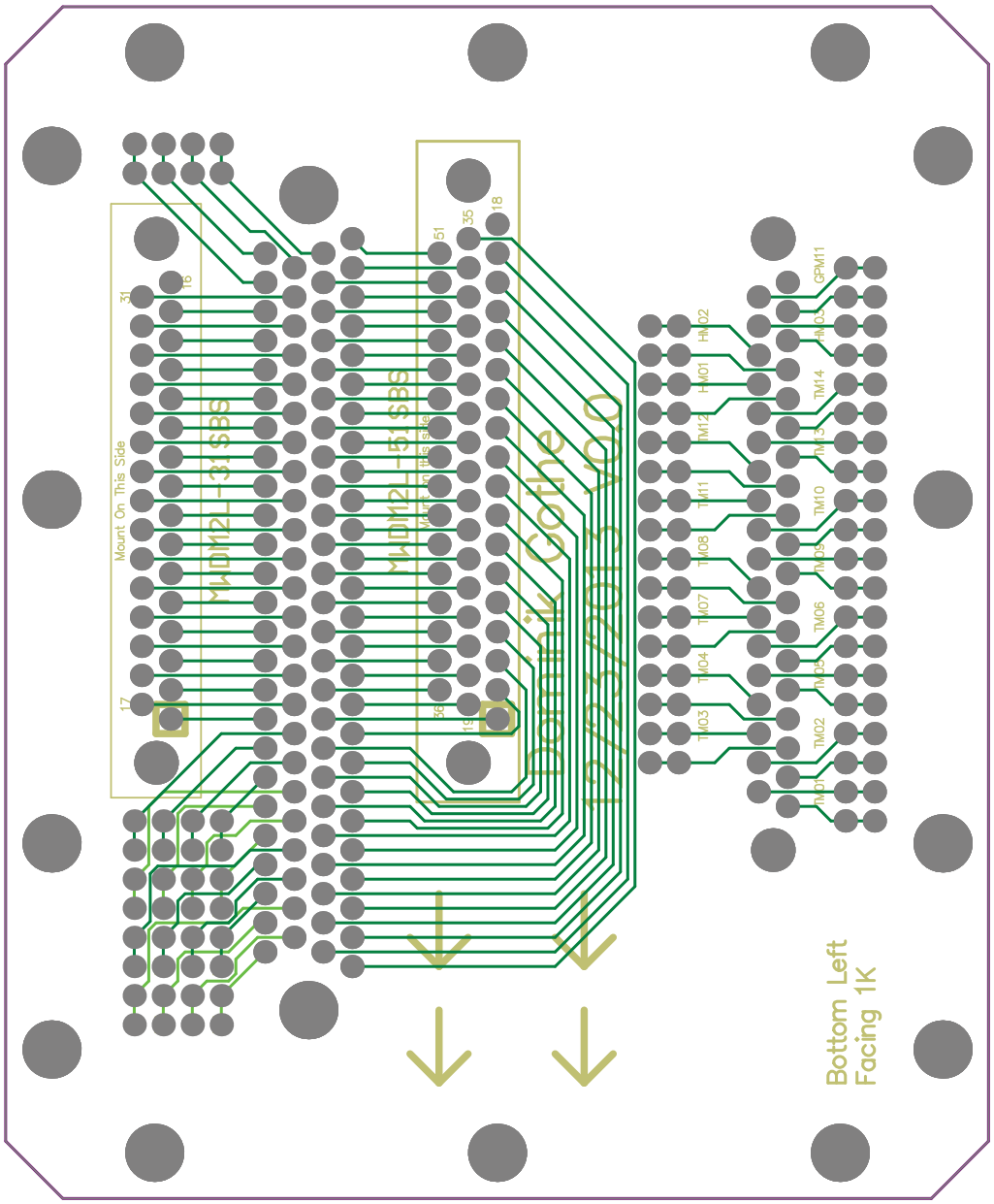


Figure 33: A flattened view of the 4K break-out-board PCB-layout.

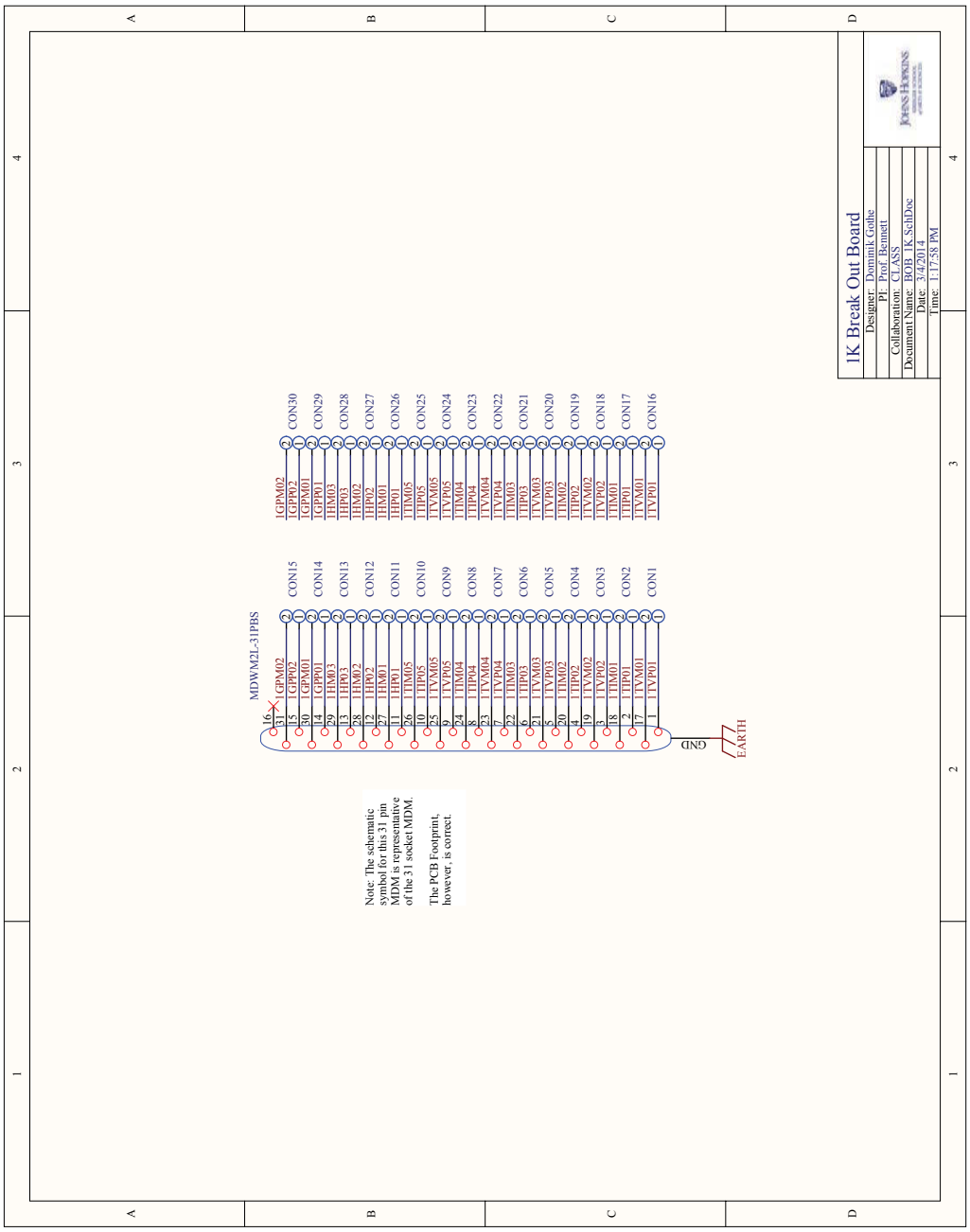


Figure 34: A schematic representation of the 4K break-out-board wiring.

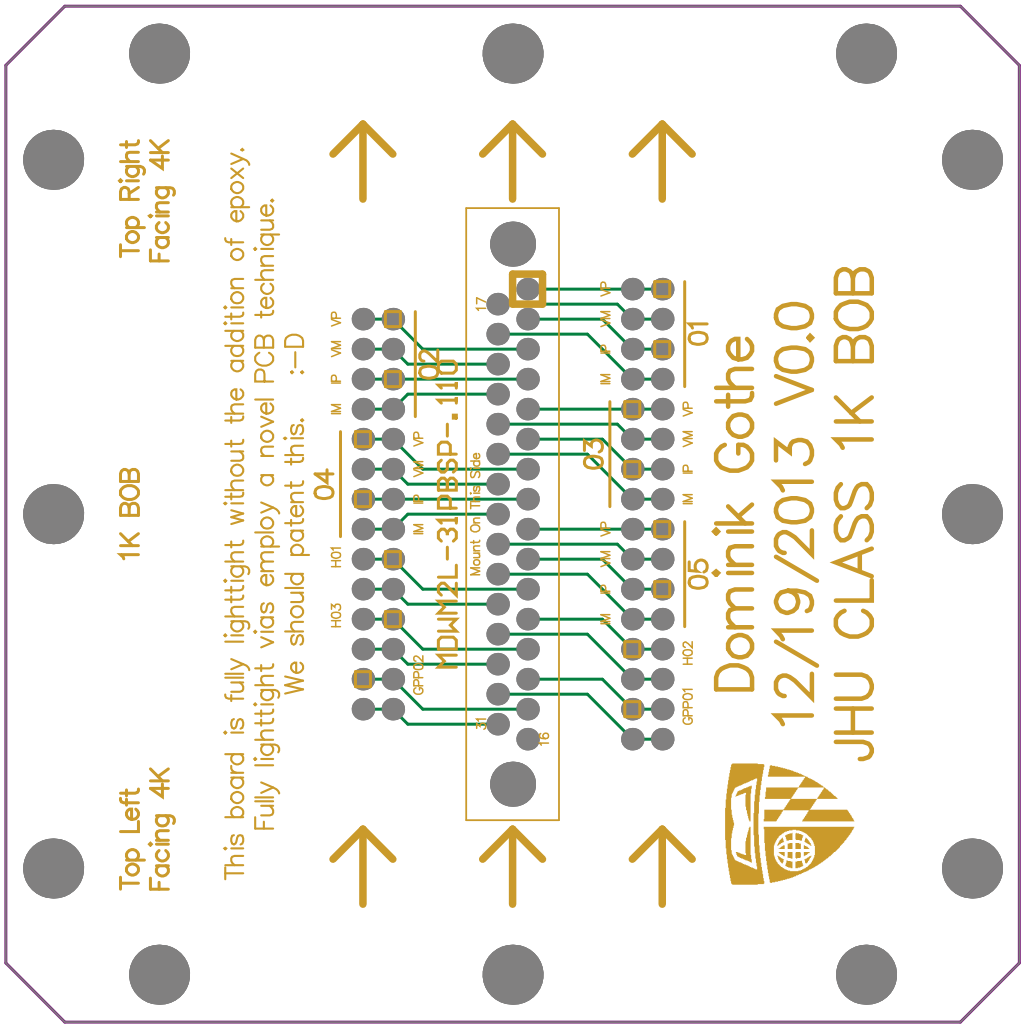


Figure 35: A flattened view of the 4K break-out-board PCB-layout.

| | | 300K Stage | 60K Stage | 4K Stage | | 1K Stage | | 100 mK Stage | |
|---|---|---|---|---|---|---|---|---|---|
| | | Conn Pin | Conn Pin | Conn | **Pin** | Conn | Pin | Conn | Pin |
| 60K GP 03 | 60GPP03 | DD-50C : 13 | 69 MDM : **48** | | | | | | |
| | 60GPM03 | DD-50C : 14 | 69 MDM : **25** | | | | | | |
| 60K GP 02 | 60GPP02 | DD-50C : 11 | 69 MDM : **49** | | | | | | |
| | 60GPM02 | DD-50C : 12 | 69 MDM : **26** | | | | | | |
| 60K GP 01 | 60GPP01 | DD-50C : 9 | 69 MDM : **50** | | | | | | |
| | 60GPM01 | DD-50C : 10 | 69 MDM : **27** | | | | | | |
| 60K HTR 03 | 60HP03 | DB-25 : 5 | 69 MDM : **51** | | | | | | |
| | 60HM03 | DB-25 : 6 | 69 MDM : **28** | | | | | | |
| 60K HTR 02 | 60HP02 | DB-25 : 3 | 69 MDM : **29** | | | | | | |
| | 60HM02 | DB-25 : 4 | 69 MDM : **52** | | | | | | |
| 60K HTR 01 | 60HP01 | DB-25 : 1 | 69 MDM : **30** | | | | | | |
| | 60HM01 | DB-25 : 2 | 69 MDM : **53** | | | | | | |
| 60K DT 07 | 60TP07 | DD-50A : 43 | 69 MDM : **36** | | | | | | |
| | 60TM07 | DD-50A : 44 | 69 MDM : **59** | | | | | | |
| 60K DT 10 | 60TP10 | DD-50A : 47 | 69 MDM : **38** | | | | | | |
| | 60TM10 | DD-50A : 48 | 69 MDM : **61** | | | | | | |
| 60K DT 09 | 60TP09 | DD-50A : 45 | 69 MDM : **39** | | | | | | |
| | 60TM09 | DD-50A : 46 | 69 MDM : **62** | | | | | | |
| 60K DT 06 | 60TP06 | DD-50A : 39 | 69 MDM : **40** | | | | | | |
| | 60TM06 | DD-50A : 40 | 69 MDM : **63** | | | | | | |
| 60K DT 08 | 60TP08 | DD-50A : 41 | 69 MDM : **41** | | | | | | |
| | 60TM08 | DD-50A : 42 | 69 MDM : **64** | | | | | | |
| 60K DT 05 | 60TP05 | DD-50A : 37 | 69 MDM : **42** | | | | | | |
| | 60TM05 | DD-50A : 38 | 69 MDM : **65** | | | | | | |
| 60K DT 04 | 60TP04 | DD-50A : 35 | 69 MDM : **43** | | | | | | |
| | 60TM04 | DD-50A : 36 | 69 MDM : **66** | | | | | | |
| 60K DT 03 | 60TP03 | DD-50A : 33 | 69 MDM : **44** | | | | | | |
| | 60TM03 | DD-50A : 34 | 69 MDM : **67** | | | | | | |
| 60K DT 02 | 60TP02 | DD-50A : 31 | 69 MDM : **45** | | | | | | |
| | 60TM02 | DD-50A : 32 | 69 MDM : **68** | | | | | | |
| 60K DT 01 | 60TP01 | DD-50A : 29 | 69 MDM : **46** | | | | | | |
| | 60TM01 | DD-50A : 30 | 69 MDM : **69** | | | | | | |

Table 5: A map of all 60 K housekeeping lines.

| | | 300K Stage | 60K Stage | 4K Stage | 1K Stage | 100 mK Stage |
|---|---|---|---|---|---|---|
| | | Conn Pin | Conn Pin | Conn **Pin** | Conn Pin | Conn Pin |
| 4K DT 01 | 4TP01 | DD-50A : 1 | 69 MDM : 01 | 37 MDM : **01** | | |
| | 4TM01 | DD-50A : 2 | 69 MDM : 02 | 37 MDM : **20** | | |
| 4K DT 02 | 4TP02 | DD-50A : 3 | 69 MDM : 03 | 37 MDM : **02** | | |
| | 4TM02 | DD-50A : 4 | 69 MDM : 04 | 37 MDM : **21** | | |
| 4K DT 03 | 4TP03 | DD-50A : 5 | 69 MDM : 05 | 37 MDM : **03** | | |
| | 4TM03 | DD-50A : 6 | 69 MDM : 06 | 37 MDM : **22** | | |
| 4K DT 04 | 4TP04 | DD-50A : 7 | 69 MDM : 07 | 37 MDM : **04** | | |
| | 4TM04 | DD-50A : 8 | 69 MDM : 08 | 37 MDM : **23** | | |
| 4K DT 05 | 4TP05 | DD-50A : 9 | 69 MDM : 09 | 37 MDM : **05** | | |
| | 4TM05 | DD-50A : 10 | 69 MDM : 10 | 37 MDM : **24** | | |
| 4K DT 06 | 4TP06 | DD-50A : 11 | 69 MDM : 11 | 37 MDM : **06** | | |
| | 4TM06 | DD-50A : 12 | 69 MDM : 12 | 37 MDM : **25** | | |
| 4K DT 07 | 4TP07 | DD-50A : 13 | 69 MDM : 13 | 37 MDM : **07** | | |
| | 4TM07 | DD-50A : 14 | 69 MDM : 14 | 37 MDM : **26** | | |
| 4K DT 08 | 4TP08 | DD-50A : 15 | 69 MDM : 15 | 37 MDM : **08** | | |
| | 4TM08 | DD-50A : 16 | 69 MDM : 16 | 37 MDM : **27** | | |
| 4K DT 09 | 4TP09 | DD-50A : 17 | 69 MDM : 17 | 37 MDM : **09** | | |
| | 4TM09 | DD-50A : 18 | 69 MDM : 18 | 37 MDM : **28** | | |
| 4K DT 10 | 4TP10 | DD-50A : 19 | 69 MDM : 19 | 37 MDM : **10** | | |
| | 4TM10 | DD-50A : 20 | 69 MDM : 20 | 37 MDM : **29** | | |
| 4K DT 11 | 4TP11 | DD-50A : 21 | 69 MDM : 21 | 37 MDM : **11** | | |
| | 4TM11 | DD-50A : 22 | 69 MDM : 22 | 37 MDM : **30** | | |
| 4K DT 12 | 4TP12 | DD-50A : 23 | 69 MDM : 23 | 37 MDM : **12** | | |
| | 4TM12 | DD-50A : 24 | 69 MDM : 47 | 37 MDM : **31** | | |
| 4K DT 13 | 4TP13 | DD-50A : 25 | 69 MDM : 60 | 37 MDM : **13** | | |
| | 4TM13 | DD-50A : 26 | 69 MDM : 37 | 37 MDM : **32** | | |
| 4K DT 14 | 4TP14 | DD-50A : 27 | 69 MDM : 58 | 37 MDM : **14** | | |
| | 4TM14 | DD-50A : 28 | 69 MDM : 35 | 37 MDM : **33** | | |
| *LordKelvin* | 4HP01 | DD-50A : 49 | 69 MDM : 57 | 37 MDM : **15** | | |
| | 4HM01 | DD-50A : 50 | 69 MDM : 34 | 37 MDM : **34** | | |
| 4K HTR 02 | 4HP02 | DB-25 : 7 | 69 MDM : 33 | 37 MDM : **16** | | |
| | 4HM02 | DB-25 : 8 | 69 MDM : 56 | 37 MDM : **35** | | |
| 4K HTR 03 | 4HP03 | DB-25 : 9 | 69 MDM : 32 | 37 MDM : **17** | | |
| | 4HM03 | DB-25 : 10 | 69 MDM : 55 | 37 MDM : **36** | | |
| 4K GP 11 | 4GPP11 | DB-25 : 11 | 69 MDM : 31 | 37 MDM : **18** | | |
| | 4GPM11 | DB-25 : 12 | 69 MDM : 54 | 37 MDM : **37** | | |
| 4K GP 01 | 4GPP01 | DD-50C : 15 | 100 MDM : 051 | 100 MDM : **051** | | |
| | 4GPM01 | DD-50C : 16 | 100 MDM : 075 | 100 MDM : **075** | | |
| 4K GP 02 | 4GPP02 | DD-50C : 17 | 100 MDM : 099 | 100 MDM : **099** | | |
| | 4GPM02 | DD-50C : 18 | 100 MDM : 100 | 100 MDM : **100** | | |
| 4K GP 03 | 4GPP03 | DD-50C : 19 | 100 MDM : 059 | 100 MDM : **059** | | |
| | 4GPM03 | DD-50C : 20 | 100 MDM : 083 | 100 MDM : **083** | | |
| 4K GP 04 | 4GPP04 | DD-50C : 21 | 100 MDM : 058 | 100 MDM : **058** | | |
| | 4GPM04 | DD-50C : 22 | 100 MDM : 082 | 100 MDM : **082** | | |
| 4K GP 05 | 4GPP05 | DD-50C : 23 | 100 MDM : 057 | 100 MDM : **057** | | |
| | 4GPM05 | DD-50C : 24 | 100 MDM : 081 | 100 MDM : **081** | | |
| 4K GP 06 | 4GPP06 | DD-50C : 25 | 100 MDM : 056 | 100 MDM : **056** | | |
| | 4GPM06 | DD-50C : 26 | 100 MDM : 080 | 100 MDM : **080** | | |
| 4K GP 07 | 4GPP07 | DD-50C : 27 | 100 MDM : 055 | 100 MDM : **055** | | |
| | 4GPM07 | DD-50C : 28 | 100 MDM : 079 | 100 MDM : **079** | | |
| 4K GP 08 | 4GPP08 | DD-50C : 29 | 100 MDM : 054 | 100 MDM : **054** | | |
| | 4GPM08 | DD-50C : 30 | 100 MDM : 078 | 100 MDM : **078** | | |
| 4K GP 09 | 4GPP09 | DD-50C : 31 | 100 MDM : 053 | 100 MDM : **053** | | |
| | 4GPM09 | DD-50C : 32 | 100 MDM : 077 | 100 MDM : **077** | | |
| 4K GP 10 | 4GPP10 | DD-50C : 33 | 100 MDM : 052 | 100 MDM : **052** | | |
| | 4GPM10 | DD-50C : 34 | 100 MDM : 076 | 100 MDM : **076** | | |

Table 6: A map of all 4 K housekeeping lines.

| | | 300K Stage | 60K Stage | 4K Stage | 1K Stage | 100 mK Stage |
|---|---|---|---|---|---|---|
| | | Conn Pin | Conn Pin | Conn **Pin** | Conn Pin | Conn Pin |
| 1K ROX 01 | 1TVP01 | DD-50B : 1 | 100 MDM : 084 | 100 MDM : 084 | 31 MDM : **01** | |
| | 1TVM01 | DD-50B : 2 | 100 MDM : 060 | 100 MDM : 060 | 31 MDM : **17** | |
| | 1TIP01 | DD-50B : 3 | 100 MDM : 085 | 100 MDM : 085 | 31 MDM : **02** | |
| | 1TIM01 | DD-50B : 4 | 100 MDM : 061 | 100 MDM : 061 | 31 MDM : **18** | |
| 1K ROX 02 | 1TVP02 | DD-50B : 5 | 100 MDM : 086 | 100 MDM : 086 | 31 MDM : **03** | |
| | 1TVM02 | DD-50B : 6 | 100 MDM : 062 | 100 MDM : 062 | 31 MDM : **19** | |
| | 1TIP02 | DD-50B : 7 | 100 MDM : 087 | 100 MDM : 087 | 31 MDM : **04** | |
| | 1TIM02 | DD-50B : 8 | 100 MDM : 063 | 100 MDM : 063 | 31 MDM : **20** | |
| 1K ROX 03 | 1TVP03 | DD-50B : 9 | 100 MDM : 088 | 100 MDM : 088 | 31 MDM : **05** | |
| | 1TVM03 | DD-50B : 10 | 100 MDM : 064 | 100 MDM : 064 | 31 MDM : **21** | |
| | 1TIP03 | DD-50B : 11 | 100 MDM : 089 | 100 MDM : 089 | 31 MDM : **06** | |
| | 1TIM03 | DD-50B : 12 | 100 MDM : 065 | 100 MDM : 065 | 31 MDM : **22** | |
| 1K ROX 04 | 1TVP04 | DD-50B : 13 | 100 MDM : 090 | 100 MDM : 090 | 31 MDM : **07** | |
| | 1TVM04 | DD-50B : 14 | 100 MDM : 066 | 100 MDM : 066 | 31 MDM : **23** | |
| | 1TIP04 | DD-50B : 15 | 100 MDM : 091 | 100 MDM : 091 | 31 MDM : **08** | |
| | 1TIM04 | DD-50B : 16 | 100 MDM : 067 | 100 MDM : 067 | 31 MDM : **24** | |
| 1K ROX 05 | 1TVP05 | DD-50C : 1 | 100 MDM : 092 | 100 MDM : 092 | 31 MDM : **09** | |
| | 1TVM05 | DD-50C : 2 | 100 MDM : 068 | 100 MDM : 068 | 31 MDM : **25** | |
| | 1TIP05 | DD-50C : 3 | 100 MDM : 093 | 100 MDM : 093 | 31 MDM : **10** | |
| | 1TIM05 | DD-50C : 4 | 100 MDM : 069 | 100 MDM : 069 | 31 MDM : **26** | |
| 1K HTR 01 | 1HP01 | DB-25 : 14 | 100 MDM : 094 | 100 MDM : 094 | 31 MDM : **11** | |
| | 1HM01 | DB-25 : 15 | 100 MDM : 070 | 100 MDM : 070 | 31 MDM : **27** | |
| 1K HTR 02 | 1HP02 | DB-25 : 16 | 100 MDM : 095 | 100 MDM : 095 | 31 MDM : **12** | |
| | 1HM02 | DB-25 : 17 | 100 MDM : 071 | 100 MDM : 071 | 31 MDM : **28** | |
| 1K HTR 03 | 1HP03 | DB-25 : 18 | 100 MDM : 096 | 100 MDM : 096 | 31 MDM : **13** | |
| | 1HM03 | DB-25 : 19 | 100 MDM : 072 | 100 MDM : 072 | 31 MDM : **29** | |
| 1K GP 01 | 1HP04 | DD-50C : 35 | 100 MDM : 097 | 100 MDM : 097 | 31 MDM : **14** | |
| | 1HM04 | DD-50C : 36 | 100 MDM : 073 | 100 MDM : 073 | 31 MDM : **30** | |
| 1K GP 02 | 1HP05 | DD-50C : 37 | 100 MDM : 098 | 100 MDM : 098 | 31 MDM : **15** | |
| | 1HM05 | DD-50C : 38 | 100 MDM : 074 | 100 MDM : 074 | 31 MDM : **31** | |

Table 7: A map of all 1 K housekeeping lines.

| | | 300K Stage | 60K Stage | 4K Stage | 1K Stage | 100 mK Stage |
|---|---|---|---|---|---|---|
| | | Conn Pin | Conn Pin | Conn **Pin** | Conn Pin | Conn Pin |
| .1 HTR 01 | .1HP01 | DB-25 : 20 | 100 MDM : 035 | 100 MDM : 035 | | 51 MDM : **01** |
| | .1HM01 | DB-25 : 21 | 100 MDM : 009 | 100 MDM : 009 | | 51 MDM : **02** |
| .1 HTR 02 | .1HP02 | DB-25 : 22 | 100 MDM : 034 | 100 MDM : 034 | | 51 MDM : **03** |
| | .1HM02 | DB-25 : 23 | 100 MDM : 008 | 100 MDM : 008 | | 51 MDM : **04** |
| .1 HTR 03 | .1HP03 | DB-25 : 24 | 100 MDM : 033 | 100 MDM : 033 | | 51 MDM : **05** |
| | .1HM03 | DB-25 : 25 | 100 MDM : 007 | 100 MDM : 007 | | 51 MDM : **06** |
| .1 ROX 01 | .1TVP01 | DD-50B : 17 | 100 MDM : 032 | 100 MDM : 032 | | 51 MDM : **07** |
| | .1TVM01 | DD-50B : 18 | 100 MDM : 006 | 100 MDM : 006 | | 51 MDM : **08** |
| | .1TIP01 | DD-50B : 19 | 100 MDM : 031 | 100 MDM : 031 | | 51 MDM : **09** |
| | .1TIM01 | DD-50B : 20 | 100 MDM : 005 | 100 MDM : 005 | | 51 MDM : **10** |
| .1 ROX 02 | .1TVP02 | DD-50B : 21 | 100 MDM : 030 | 100 MDM : 030 | | 51 MDM : **11** |
| | .1TVM02 | DD-50B : 22 | 100 MDM : 004 | 100 MDM : 004 | | 51 MDM : **12** |
| | .1TIP02 | DD-50B : 23 | 100 MDM : 029 | 100 MDM : 029 | | 51 MDM : **13** |
| | .1TIM02 | DD-50B : 24 | 100 MDM : 003 | 100 MDM : 003 | | 51 MDM : **14** |
| .1 ROX 03 | .1TVP03 | DD-50B : 25 | 100 MDM : 028 | 100 MDM : 028 | | 51 MDM : **15** |
| | .1TVM03 | DD-50B : 26 | 100 MDM : 002 | 100 MDM : 002 | | 51 MDM : **16** |
| | .1TIP03 | DD-50B : 27 | 100 MDM : 027 | 100 MDM : 027 | | 51 MDM : **17** |
| | .1TIM03 | DD-50B : 28 | 100 MDM : 001 | 100 MDM : 001 | | 51 MDM : **35** |
| .1 ROX 04 | .1TVP04 | DD-50B : 29 | 100 MDM : 010 | 100 MDM : 010 | | 51 MDM : **19** |
| | .1TVM04 | DD-50B : 30 | 100 MDM : 036 | 100 MDM : 036 | | 51 MDM : **36** |
| | .1TIP04 | DD-50B : 31 | 100 MDM : 011 | 100 MDM : 011 | | 51 MDM : **20** |
| | .1TIM04 | DD-50B : 32 | 100 MDM : 037 | 100 MDM : 037 | | 51 MDM : **37** |
| .1 ROX 05 | .1TVP05 | DD-50B : 33 | 100 MDM : 012 | 100 MDM : 012 | | 51 MDM : **21** |
| | .1TVM05 | DD-50B : 34 | 100 MDM : 038 | 100 MDM : 038 | | 51 MDM : **38** |
| | .1TIP05 | DD-50B : 35 | 100 MDM : 013 | 100 MDM : 013 | | 51 MDM : **22** |
| | .1TIM05 | DD-50B : 36 | 100 MDM : 039 | 100 MDM : 039 | | 51 MDM : **39** |
| .1 ROX 06 | .1TVP06 | DD-50B : 37 | 100 MDM : 014 | 100 MDM : 014 | | 51 MDM : **23** |
| | .1TVM06 | DD-50B : 38 | 100 MDM : 040 | 100 MDM : 040 | | 51 MDM : **40** |
| | .1TIP06 | DD-50B : 39 | 100 MDM : 015 | 100 MDM : 015 | | 51 MDM : **24** |
| | .1TIM06 | DD-50B : 40 | 100 MDM : 041 | 100 MDM : 041 | | 51 MDM : **41** |
| .1 ROX 07 | .1TVP07 | DD-50B : 41 | 100 MDM : 016 | 100 MDM : 016 | | 51 MDM : **25** |
| | .1TVM07 | DD-50B : 42 | 100 MDM : 042 | 100 MDM : 042 | | 51 MDM : **42** |
| | .1TIP07 | DD-50B : 43 | 100 MDM : 017 | 100 MDM : 017 | | 51 MDM : **26** |
| | .1TIM07 | DD-50B : 44 | 100 MDM : 043 | 100 MDM : 043 | | 51 MDM : **43** |
| .1 ROX 08 | .1TVP08 | DD-50B : 45 | 100 MDM : 018 | 100 MDM : 018 | | 51 MDM : **27** |
| | .1TVM08 | DD-50B : 46 | 100 MDM : 044 | 100 MDM : 044 | | 51 MDM : **44** |
| | .1TIP08 | DD-50B : 47 | 100 MDM : 019 | 100 MDM : 019 | | 51 MDM : **28** |
| | .1TIM08 | DD-50B : 48 | 100 MDM : 045 | 100 MDM : 045 | | 51 MDM : **45** |
| .1 ROX 09 | .1TVP09 | DD-50C : 5 | 100 MDM : 020 | 100 MDM : 020 | | 51 MDM : **29** |
| | .1TVM09 | DD-50C : 6 | 100 MDM : 046 | 100 MDM : 046 | | 51 MDM : **46** |
| | .1TIP09 | DD-50C : 7 | 100 MDM : 021 | 100 MDM : 021 | | 51 MDM : **30** |
| | .1TIM09 | DD-50C : 8 | 100 MDM : 047 | 100 MDM : 047 | | 51 MDM : **47** |
| .1 GP 01 | .1TVP10 | DD-50C : 39 | 100 MDM : 022 | 100 MDM : 022 | | 51 MDM : **31** |
| | .1TVM10 | DD-50C : 40 | 100 MDM : 048 | 100 MDM : 048 | | 51 MDM : **48** |
| | .1TIP10 | DD-50C : 41 | 100 MDM : 023 | 100 MDM : 023 | | 51 MDM : **32** |
| | .1TIM10 | DD-50C : 42 | 100 MDM : 049 | 100 MDM : 049 | | 51 MDM : **49** |
| .1 GP 02 | .1TVP11 | DD-50C : 43 | 100 MDM : 024 | 100 MDM : 024 | | 51 MDM : **33** |
| | .1TVM11 | DD-50C : 44 | 100 MDM : 050 | 100 MDM : 050 | | 51 MDM : **50** |
| | .1TIP11 | DD-50C : 45 | 100 MDM : 025 | 100 MDM : 025 | | 51 MDM : **34** |
| | .1TIM11 | DD-50C : 46 | 100 MDM : 026 | 100 MDM : 026 | | 51 MDM : **51** |

Table 8: A map of all 100 mK housekeeping lines.

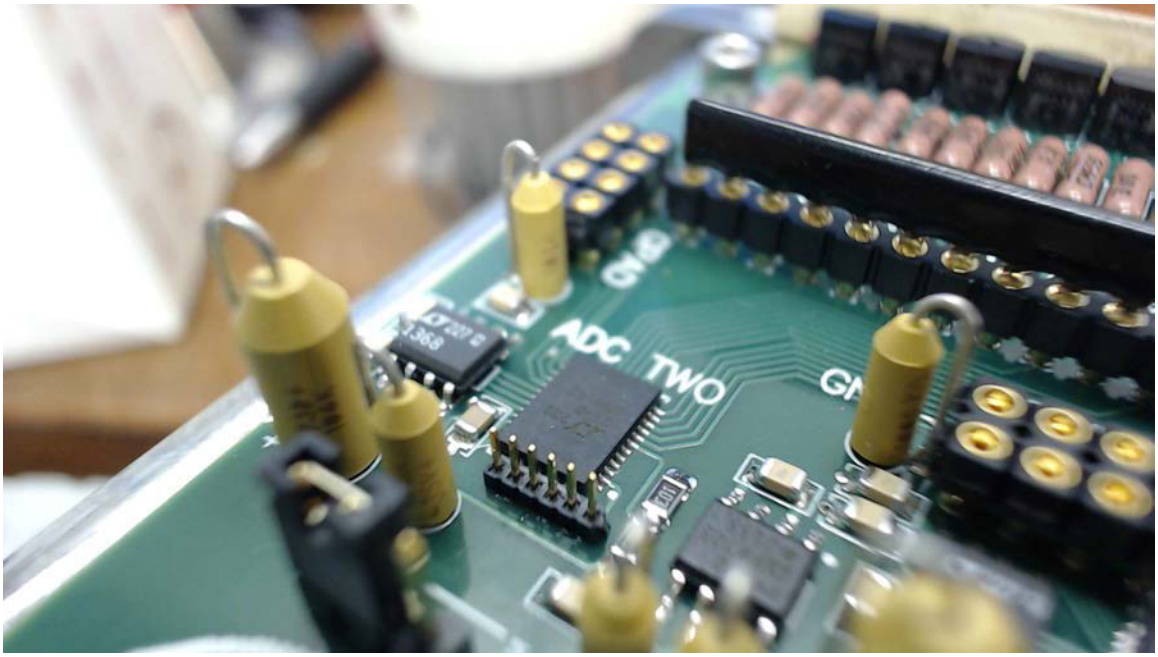


Figure 36: The heart of the data-acquisition, the LTC2449 analog-to-digital converter.

## 8.4 Custom Diode Circuit

The cryogenic systems of CLASS can be outfitted with up to 24 diodes. A commercial solution to read out this number of sensors at high sampling rates is cost prohibitive. The design requirement for a custom solution was simple: 24 channels with a target sampling rate of 100 Hz. "Sleipnir" is the codename for the diode readout project that met and exceed these design requirements.

Sleipnir is designed to bias up to 32 diodes with a constant, temperature compensated, 10 $\mu$A of constant DC current. The voltage drop across the diode is then measured by two high speed, synchronous, muxing, 16 channel Analog to Digital Converters (ADCs).

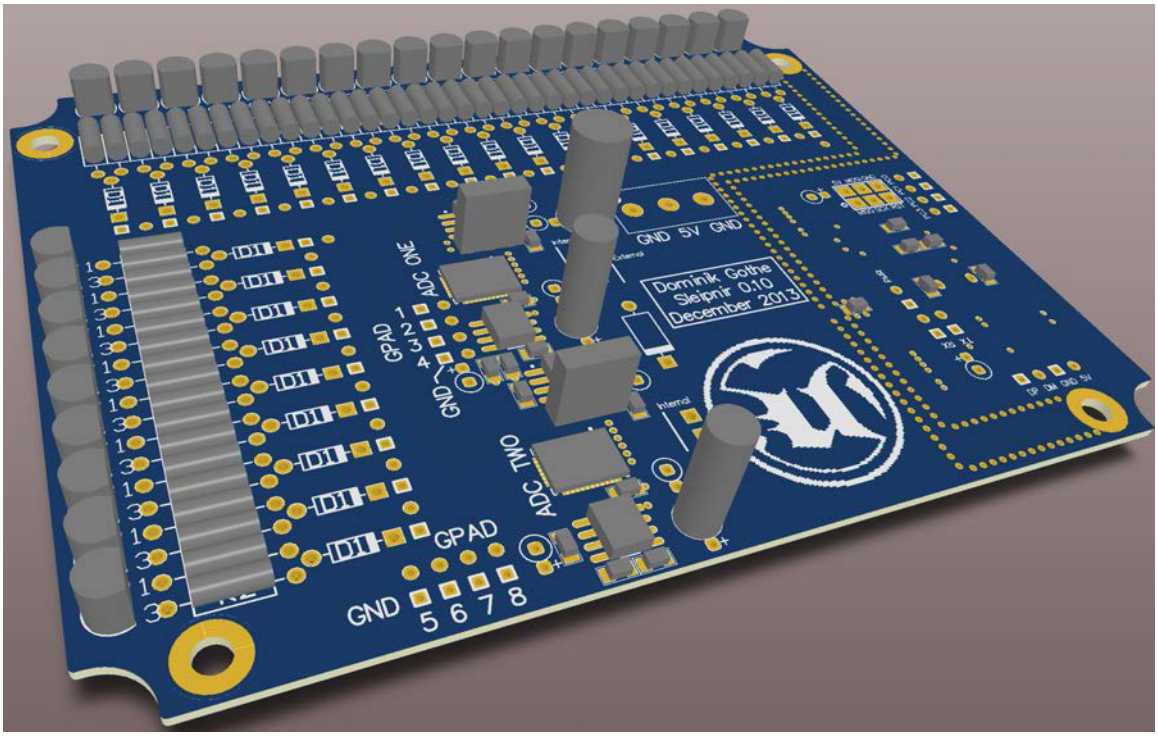


Figure 37: A 3D render of the Sleipnir Circuit Board. The current sources are populated on the periphery with both ADCs clearly visible. The micro-controllers are located on the opposite side.

The measurements are done over a standard two-wire scheme, interfacing with the cryostat's warm break-out via a one-to-one, shielded, twisted pair, 50 pin D-subminiature cable. The device connects directly to a computer, running either Linux or windows and the user interface for Sleipnir writes dir-files directly, the CLASS standard format. This ease of use makes it an incredibly convenient and seamlessly integrated instrument in the CLASS architecture.

### 8.4.1 Hardware

The heart of Sleipnir is the highly[6] linear LTC2449. This is an ADC built by Linear Technology based on sigma delta conversion techniques. Sigma-delta ADCs use very high oversampling ratios of up to $32768$, in the case of the LTC2449. This high over sampling rate with a very fast front end sample and hold ADC allows highly simplified anti aliasing filters to be deployed. In the case of Sleipnir the LTC2449 runs at a sampling frequency of $4\ \mathrm{MHz}$. Any information above the sample rate, typically $100\ \mathrm{Hz}$ up to the sample frequency of $4\ \mathrm{MHz}$ is rejected by the built in Sync envelope filter of the sigma delta architecture. Thus the LTC2449 is able to achieve very high resolution of up to $24.6$ effective bits, or $200\ \mathrm{nV}$. Another benefit of the LTC2449 is its automatic off-set calibration. Between every sample the ADC is calibrated against ground, therefore removing any $1/f$ drifts in offset. The LTC2449 allows a buffer amplifier to be inserted inside the calibration chain. This allows high impedance inputs without loss of absolute precision. Sleipnir uses the LT1368 Op-Amp to present a high enough impedance as to not significantly effect the measurement of the voltage drop across the diodes. These two considerations make the LTC2449 the ideal ADC for Sleipnir.

The voltage reference, used by the ADC is provided by an Analog Devices's ADR4540, at $V_{REF} = 4.096$. A common voltage of $V_{REF}/2$ is created by a simple $10\ \mathrm{k\Omega} : 10\ \mathrm{k\Omega}$ resistor ladder. Since the current sources return to ground, the voltage drop across the diode can be measured with a single ended measurement taken at the current source. The

[6]The LTC2449 specifies a total integral nonlinearity of $5\ ppm$ with respect to the voltage reference.

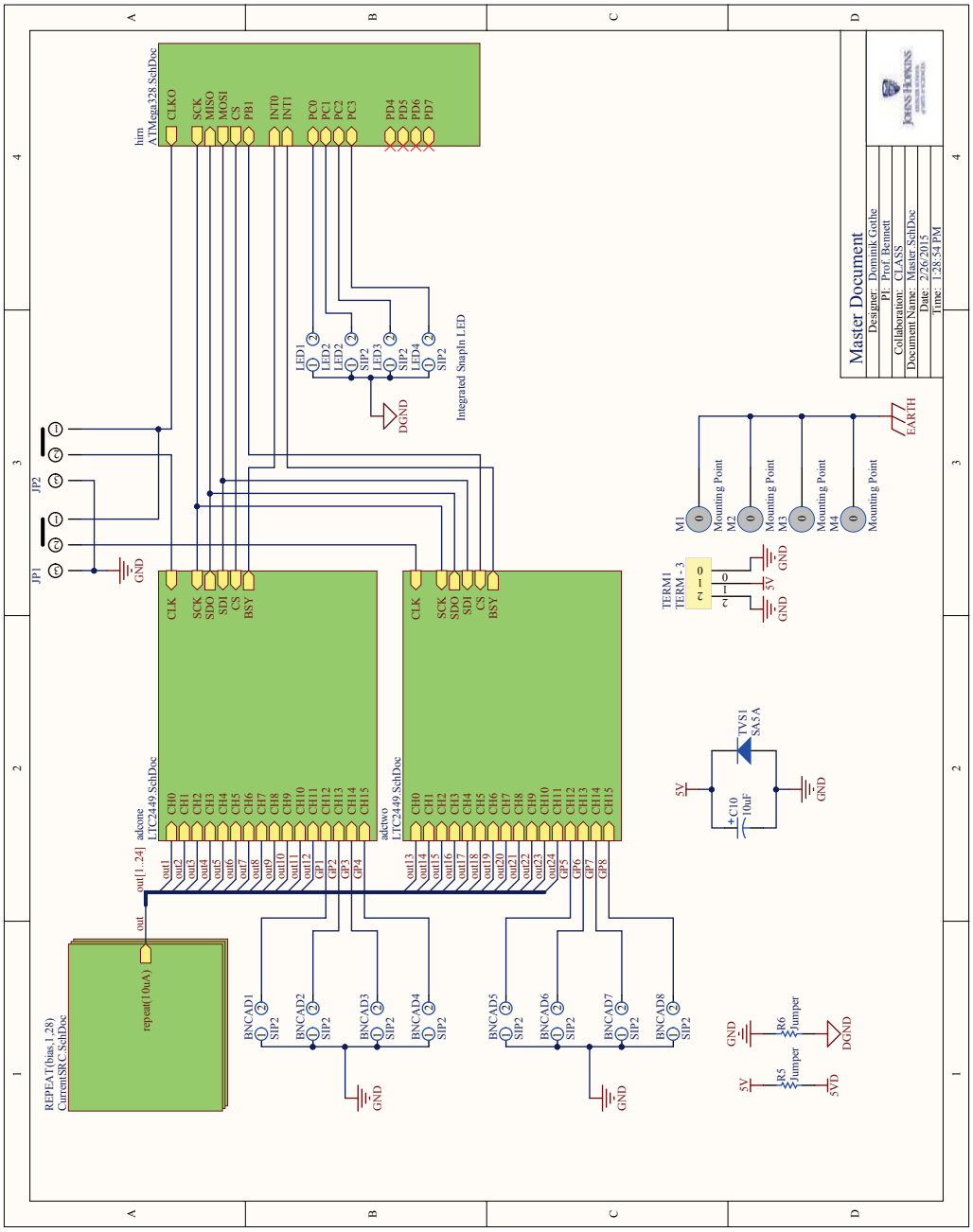


Figure 38: The Master schematic shows how the following sheets are related and interconnected.

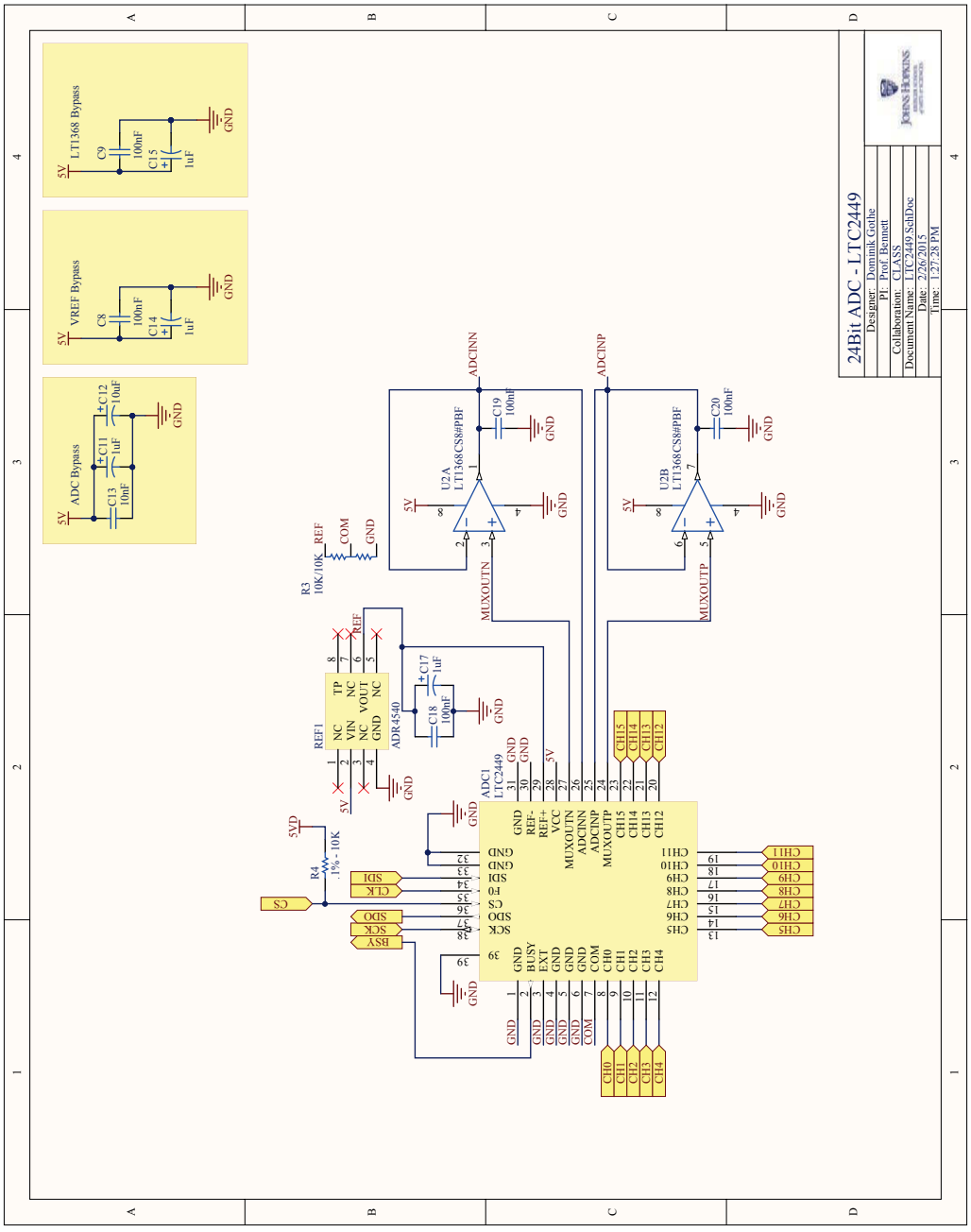


Figure 39: At the heart of the Sleipnir system are two LTC2449 analog-to-digital converters.

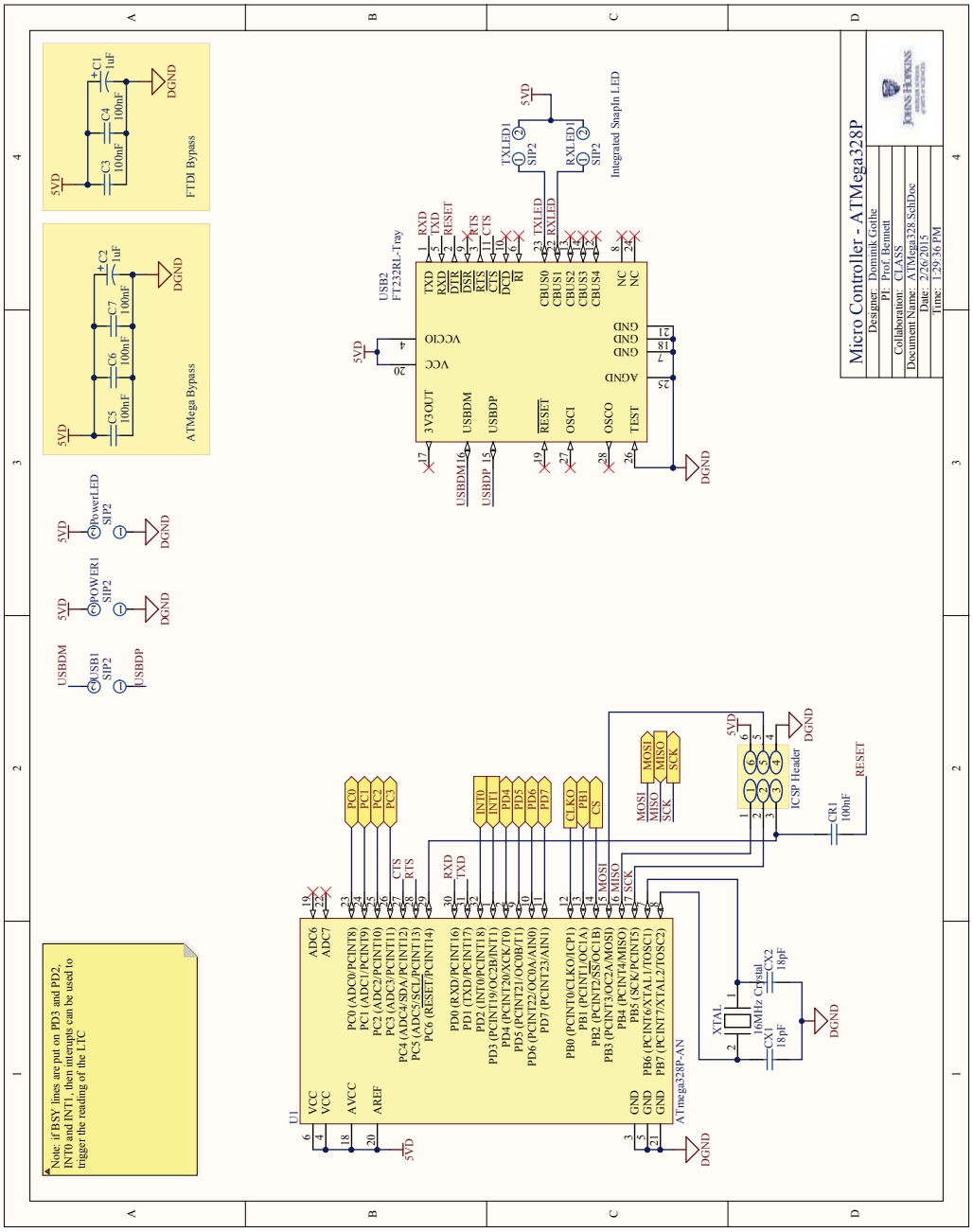


Figure 40: The ATMega328p provides the control glue for the ADC and the USB interface, the FT232RL.

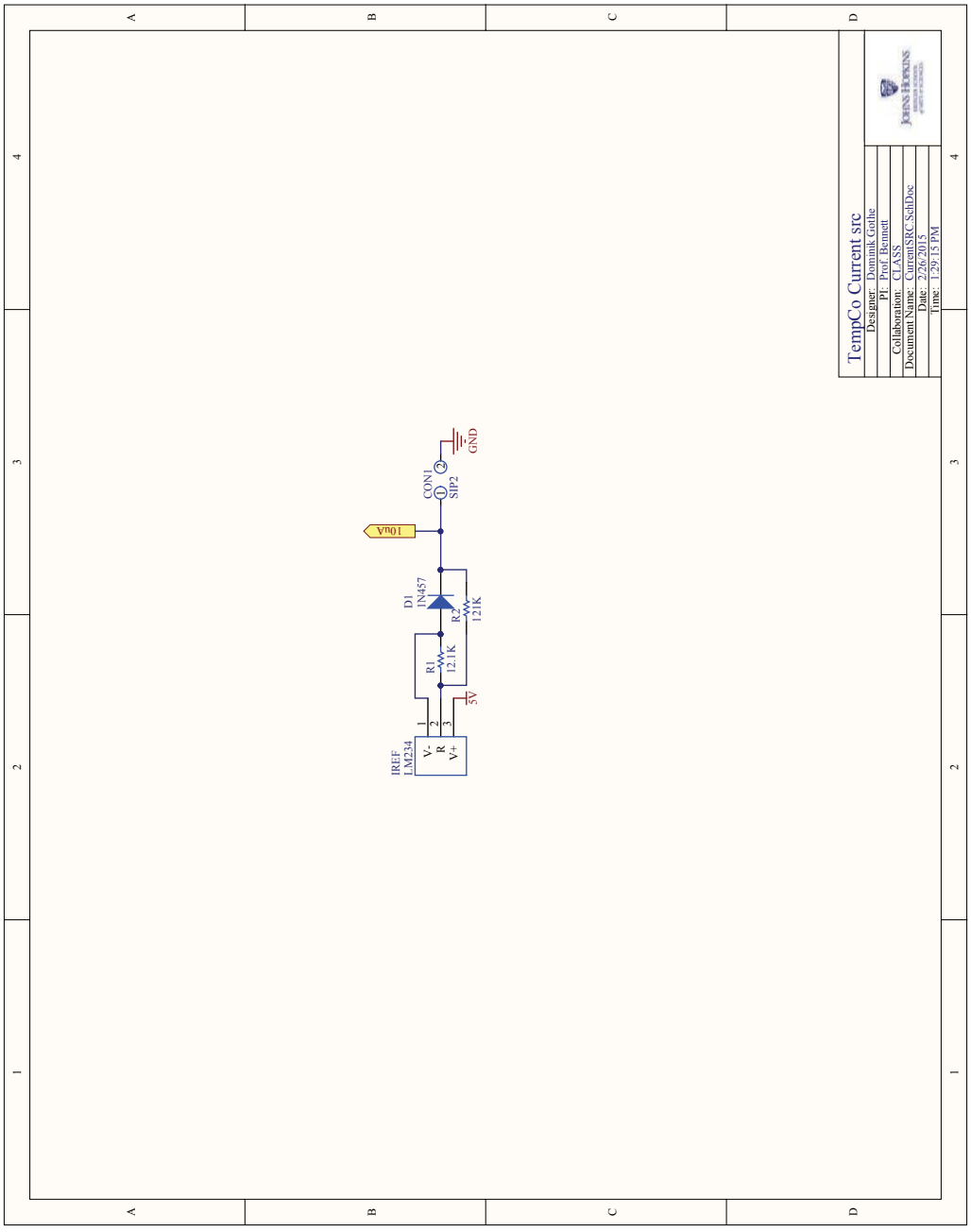


Figure 41: The temperature compensated current source used in Sleipnir to generate a $10\mu$A current bias.

range of the ADC is set by the voltage reference. However, it still has to compare the input to a reference signal. This is typically ground. To compare to ground the buffer opamps would require bi-polar power supplies as to give enough head-room at the rails. Elevating the common voltage from ground to $V_{REF}/2$, as done by the resistor ladder, simplifies the power requirements of Sleipnir to a single ended $5$ V power supply. Only one supply is necessary to power the ADCs, the buffers, and the voltage references. It is also a convenient level as $5V$ corresponds to the TTL level logic often used by $8$-bit micro-processors. The layout of the analog electronics can best be visualized with a the $3-D$ model in figure 37. Figure 39, 40, and 42 show the schematic of analog front end, the logic control, and the current source. While 38 shows how these schematic sheets are connected in the greater scheme.

The logic is implemented on Atmell's `ATmega328P` micro-processor. This chip is responsible for communicating, and controlling the ADC's via a Serial Peripheral Interface (SPI) running at $10$ MHz. It converts the samples from the ADC into a voltage and reports those to the host computer via Future Technology Devices International's `FTDI232R`. The `FTDI232R` creates a virtual COM port over a USB connection and communicates with the micro-processor via a simple, two wire, asynchronous serial interface.

### 8.4.2 Consistent Overhead Byte Stuffing Encoding

To ensure consistant data transfer over the streaming, asynchronous, serial interface I decided to implement an encoding scheme that would allow for identification of the start of a

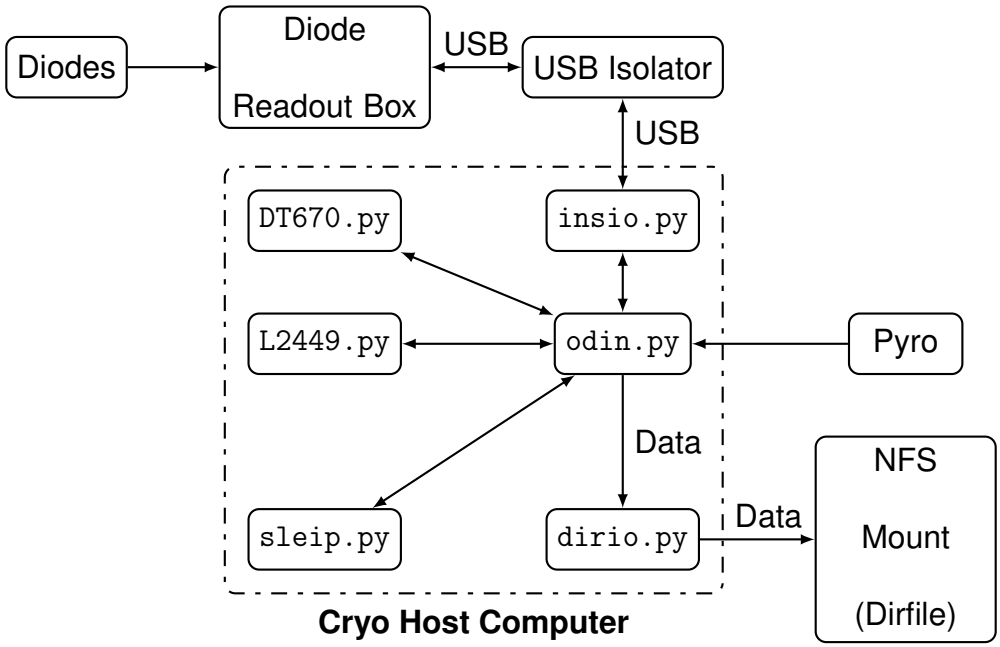


Figure 42: Schematic overview of Sleipnir, including the user interface. [Diagram courtesy of Matthew Petroff.]

new packet. The mechanism used is known as Consistent Overhead Byte Stuffing (COBS). The COBS algorithm, as implemented in Sleipnir replaces the `0x00` byte naturally occurring in the data, so that the `0x00` byte can be used as FLAG. This flag indicates the start of a new packet, the host computer can therefore jump into the stream at any given time and recover the start of the packets without prior knowledge.

### 8.4.3 Software

The user interface for Sleipnir runs on the respective cryo host computer. The software consists of six primary blocks. The communication is handled via the instrument IO class, `insio.py`. This class is responsible for latching onto the com-port and extract data packets from the stream. These packets are also decoded in this class. The Sleipnir class, `sleip.py`, contains information about the hardware layout of CLASS and how the packets are constructed. It can extract the channel number and ADC number as well as the ADC word from the data packet. The ADC word is then translated into a voltage by the `LTC2449` class, `L2449.py`. This conversion relies on four separate $12^{th}$ degree Chebychev polynomials with an RMS deviation of less than $10\,\mathrm{mK}$ from the theoretical response. Finally the voltage is converted to a temperature according to Lakeshore's specifications by the DT670 class, `DT670.py`. Once the voltage is calculated it is recorded along with the time the measurement was taken, the ADC number, and the channel number through the DirIO class. The DirIO, `dirio.py` is responsible for writing correctly formatted dir-files compatible with the CLASS architecture. The dir-files are directly written to the NFS-Mount, circumventing the need to move data. Odin is the python class that integrates all of these software blocks and ties the system into the PyRo control structure (see section 9).

### 8.4.4 Interface Isolation

When Sleipnir is configured so that the digital section receives power from the analog portion then the USB interface can be easily isolated using Analog Devices' `ADuM4160`.

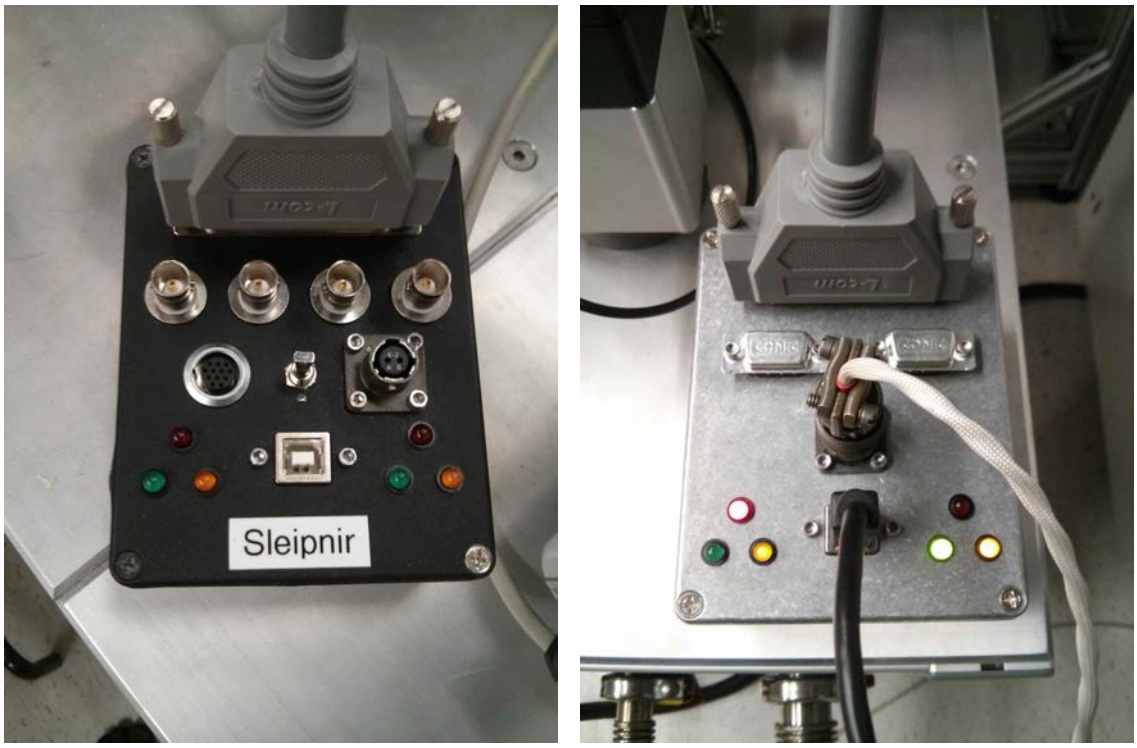


(a) Sleipnir Prototype

(b) Sleipnir Rev. A

Figure 43: Nothing is perfect the first time. Figure 43(a) shows the Sleipnir prototype. The face was cleaned up and simplified. Most importantly the production version, figure 43(b), no longer uses a non-conductive paint.

Pre-fabricated boards based on this isolation can be purchased from Circuits@Home[7]. This isolation is necessary to prevent the noise present on USB lines to infiltrate the cryostat and be picked up by the detectors.

[7] www.circuitsathome.com

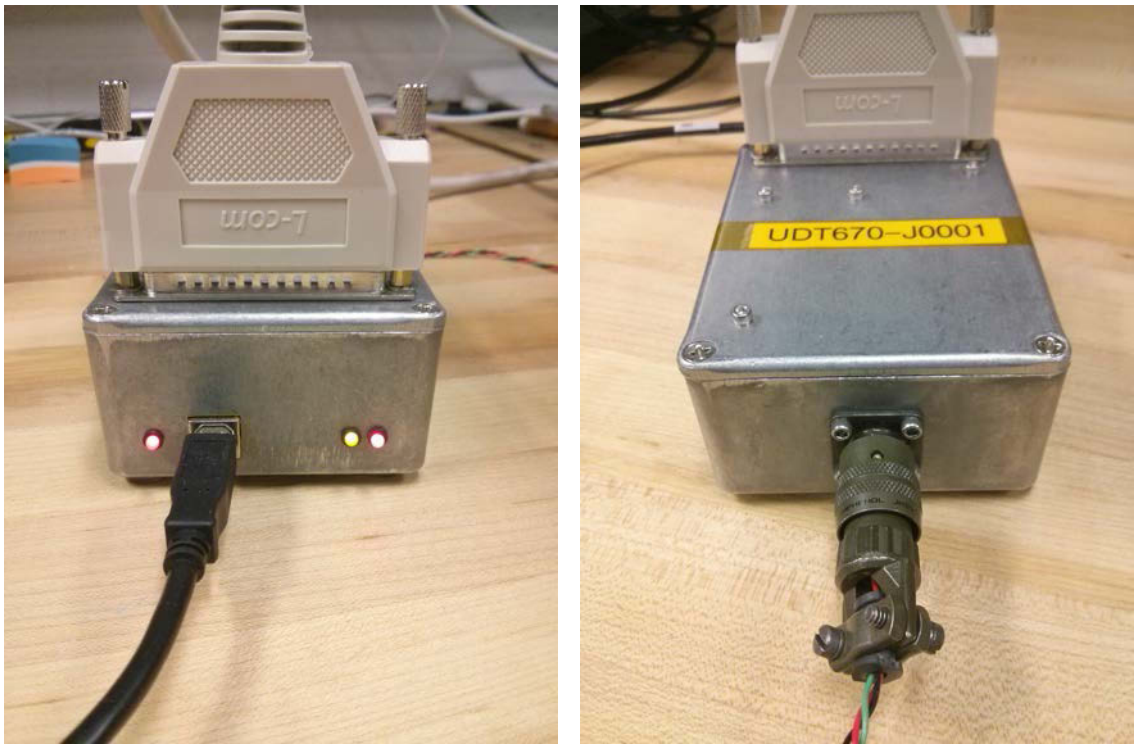


(a) UDT670 Rear

(b) UDT670 Front

Figure 44: The UDT670 device is the precursor to the Sleipnir system. It is fully functional and still used on one of our test cryostats, Bertha. Figure 44(a) shows the USB interface, power and debug LEDs. Figure 44(b) shows the power port, requiring a bipolar power supply.

## 8.5 The G Measurements

To understand the thermal performance of the cryostat I measured and calculated the thermal conductivity of the various stages. To do this I lump the length, area, and thermal conductivity into one constant, $G$. It is important to be aware that $G$ may not be constant with temperature.

$$P = G * \Delta T \tag{69}$$

The locations of the diodes are detailed in table 9. The table gives a description of the diode's locations, the schematic name corresponding to the pinout in section 8.3. It also indicates the color code of the wiring used to connect that particular diode. The serial number and type of diode is noted and finally the signal is mapped all the way through to Sleipnir's ADC and channel number.

### 8.5.1 HP6643 Control Code

The IEEE-488 is an 8-bit parallel multi-master interface developed by Hewlett-Packard under the codename HP-IB (Hawlett-Packard Interface Bus), today it is commonly known under the name GPIB (General Purpose Interface Bus) and is very commonly used by instrument developers targeting scientific labs. This standard does not only define a standard electrical interface, however it also defines a framework for a command set. These GPIB commands are used by the Standford Research System's Mainframe, the SIM900. This makes knowledge of the GPIB standard very practical.

To conduct the G measurements I used an HP6643 power supply. This power supply

| Location | Sch. Name | Color | DT-670 | Serial | adc | ch |
|---|---|---|---|---|---|---|
| 4K Series Array Board | 60K DT 01 | Red | C-CU | D6029761 | adc2 | 2 |
| 60K Plate next to BluFors Therm. | 60K DT 02 | Blue | C-CU | D6029762 | adc2 | 3 |
| 60K Plate Det. Feedthrough | 60K DT 03 | Yellow | C-CU | D6029759 | adc2 | 4 |
| 60K Plate Hous. Feedthrough | 60K DT 04 | Green | C-CU | D6039760 | adc2 | 5 |
| 60K Radiation Shield 3/3 146.7 cm | 60K DT 05 | Red | C-CU | D6032465 | adc2 | 6 |
| 60K Radiation Shield 2/3 96.0 cm | 60K DT 06 | Blue | C-SD | D6031606 | adc2 | 7 |
| 60K Radiation Shield 1/3 52.0 cm | 60K DT 07 | Yellow | C-SD | D6032235 | adc2 | 8 |
| 60K Radiation Shield 3/3 0.0 cm | 60K DT 08 | Green | C-CU | D6029765 | adc2 | 9 |
| Free Float | 60K DT 09 | White | C-SD | D6032233 | adc2 | 10 |
| Thermal Filter Stack | 60K DT 10 | Black | C-CU | D6032664 | adc2 | 11 |
| Cal Plate | 4K DT 01 | Red | B1-CU | D6031017 | adc1 | 0 |
| Cal Plate | 4K DT 02 | Blue | B1-CU | D6031033 | adc1 | 1 |
| SA Heat Sink | 4K DT 03 | Yellow | B1-CU | D6030649 | adc1 | 2 |
| BF Wire Feedthrough | 4K DT 04 | Green | B1-CU | D6030521 | adc1 | 3 |
| 4K Radiation Shield 3/3 141.0 cm | 4K DT 05 | Red | B1-CU | D6030622 | adc1 | 4 |
| 4K Radiation Shield 2/3 91.5 cm | 4K DT 06 | Blue | B1-SD | D6033167 | adc1 | 5 |
| 4K Radiation Shield 1/3 48.0 cm | 4K DT 07 | Yellow | B1-SD | D6033534 | adc1 | 6 |
| 4K Radiation Shield 0/3 0.0 cm | 4K DT 08 | Green | B1-CU | D6030627 | adc1 | 7 |
| Free Float | 4K DT 09 | White | B1-SD | D6033628 | adc1 | 8 |
| Thermal Filter Stack | 4K DT 10 | Black | B1-CU | D6030628 | adc1 | 9 |
| 100k Res | 4K DT 11 | Red-Blk | B1-CU | n/a | adc1 | 10 |
| SHA-D01 LK | 4K DT 12 | Blu-Blk | B1-CU | n/a | adc1 | 11 |
| Short | 4K DT 13 | Yel-Blk | B1-CU | n/a | adc2 | 0 |
| 1K Lens Dummy | 4K DT 14 | Grn-Blk | B1-CU | D6030589 | adc2 | 1 |

Table 9: Map of diode locations and Sleipnir's corresponding channels.

has a GPIB interface allowing one to remotely set parameters such as voltage, current, and power. A simple USB-to-GPIB converter, coupled with a Raspberry-Pi allowed me to create a powerful internet based, intelligent controller for the HP6643 power supply. This reduces the human-time required for a successful test, time constants can be as high as hours, manual operators will often forget about the experiment, allowing $1/f$ drift to reduce the accuracy of the run.

### 8.5.2 60K Load Test

Loading the top of the $60\ \mathrm{K}$ can is expected to produce $G$ values which monotonically decrease according to distance away from the cooling reservoir. That is, the $60\ \mathrm{K}$ plate should show the smallest response in temperature, while the top of the can should exhibit the largest. If there are no relative errors and the heat loading can be modeled as coming from a point source at the top of the can. These are reasonable assumptions as the power applied to the to heating-resistor is significant compared to residual loading.

Figure 45 shows analyzed results of the $60\ \mathrm{K}$ data (see figure 46) taken in April 2014. From this data we can extract the G value for the $60\ \mathrm{K}$ stage as follows:

$$G_{60\mathrm{K}} \approx 2\frac{K}{\mathrm{W}}\,. \tag{70}$$

The data contains far more information that becomes obvious when studying the temperature versus load at several different locations. We first note that we expect all thermometers to have an equal temperature if there is no loading. By fitting a line to the data and extrapolating one can identify the approximate location where the T-P curves of all the thermome-

ters intersect. This tells us that there is roughly a $0.615\ \mathrm{W}$ residual loading on the $60\ \mathrm{K}$ stage. This is intrinsic loading from the $300\ \mathrm{K}$ shield. This number can be used to quantitatively measure the quality of radiative shielding applied to the $60\ \mathrm{K}$ stage. Furthermore, it also tells us that the theoretical limit of this particular fridge is a $42.7\ \mathrm{K}$ base temperature. This provides the data necessary to make an informed decision in regards to adding more super-insulation to potentially reduce base temperatures.

With the help of this graph we can also identify the thermometer sitting at the base of the $60\ \mathrm{K}$ can to be an unreliable indicator of the $60\ \mathrm{K}$ temperature. We expect it to have a smaller response to loading then the thermometer sitting at $1/3$ up the can. That is its regression line should have a smaller slope than that of the $1/3$ thermometer. However, it has a slope of $1.039\ \mathrm{K/W}$, which is larger than the $0.8806\ \mathrm{K/W}$ of the thermometer located further towards up the can. Additionally there is an offset in temperature of about $2\ \mathrm{K}$. The slope indicates that the thermal resistance to the bath is higher, this could be caused by mounting the diode on the lip of the can, versus being epoxied onto the can directly. The temperature offset indicates that this diode sees additional loading not present at the other diodes. This can easily be explained by realizing that this particular diode is exposed to $300\ \mathrm{K}$ radiation, while the others are not. For both of these reasons, this thermometer should be considered an unreliable representation of the temperature, and it's data is not used in calculating the G value.

Finally, we can improve our understanding of the $60\ \mathrm{K}$ temperature by calibrating the diodes against each other. All of the diodes can have offsets of up to $.5\ \mathrm{K}$. These relative

offsets can be removed by realizing, that the temperatures should be exactly equal at zero loading. That is their regression lines should be minimally adjusted to have a well defined intersection. In general this is accomplished by subtracting a value, $\alpha_i$ from the respective intercept of the regression line, then minimizing the sum of all $\alpha_i$. In this case the diode on the Filter Stack should be adjusted by $-0.55\ \mathrm{K}$ and the diode at the top of the can should be adjusted by $-0.15\ \mathrm{K}$. Both of these adjustments are well within the error bars quoted by Lake Shore, offering a consistent analysis.

### 8.5.3 4 K Load Test

The thermal conductance measurement for the $4\ \mathrm{K}$ Stage was more difficult to execute as the time constants were shorter and the drift in base temperature higher. To work around this a carefully timed heating profile was automated. The data could then be fit to an exponential regression. This fit is repeated for each step in the measurement and then averaged. This allows for a more precise identification of the equilibrium temperature. These results are plotted in figure 48, and extracted from the raw data shown in figure 49. A linear fit was insufficient, and thus not plotted in 48. Instead a second order correction was necessary for a high $R$ regression. A second order polynomial of the form

$$T(P) = aP^2 + bP + c \tag{71}$$

was used to fit the data. The results of this regression is summarized in table 10. The necessity of this second order correction indicates that the thermal resistance changes appreciably at low temperatures. Specifically the thermal resistance increases as temperature

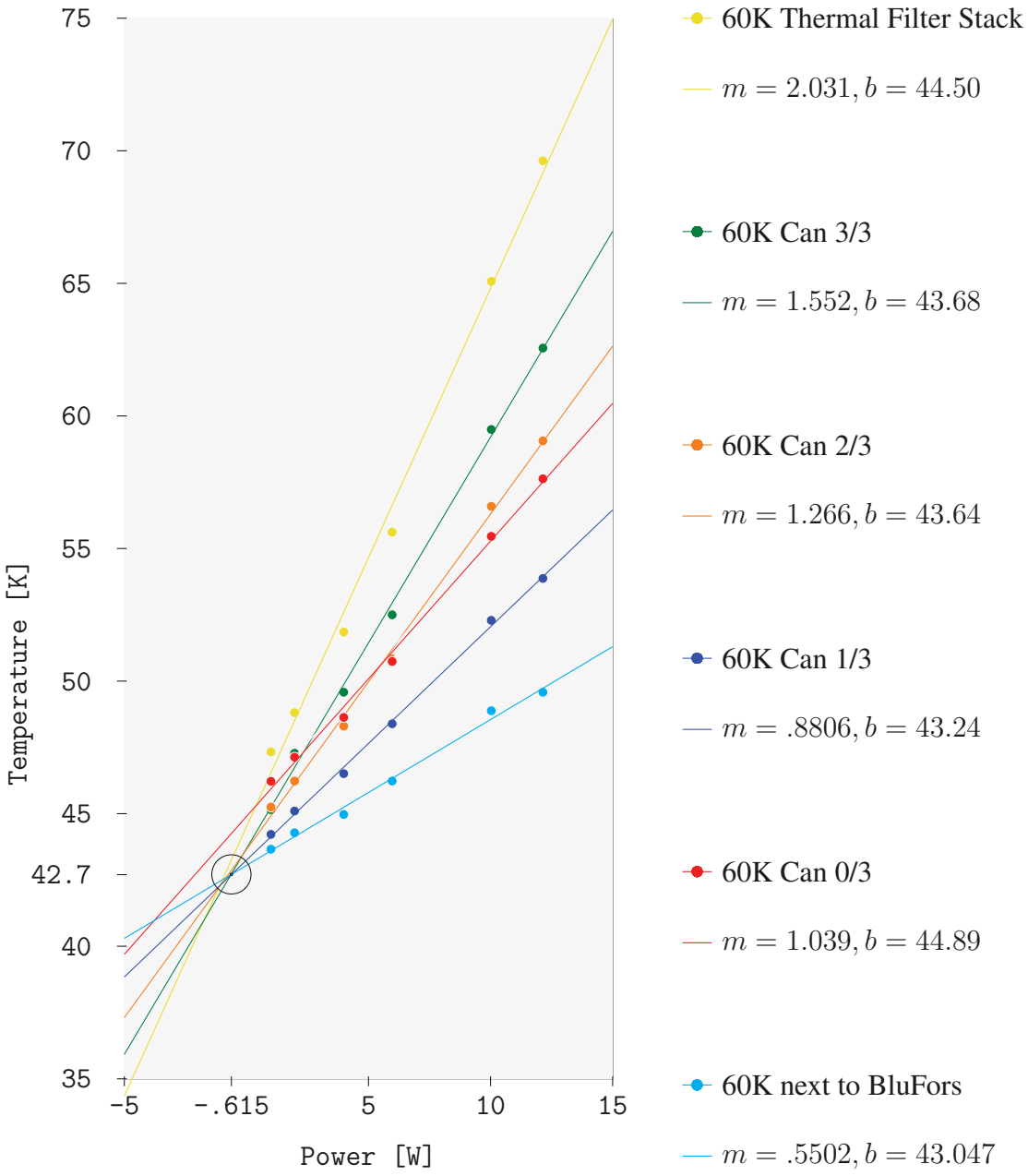


Figure 45: These are the results of the second loading test performed on Cryo One in April $10^{th}$ 2014. The temperature is plotted versus the power applied to the heater. Linear fits, of the form $y = mx + b$, are performed and the coefficients shown in the legend.

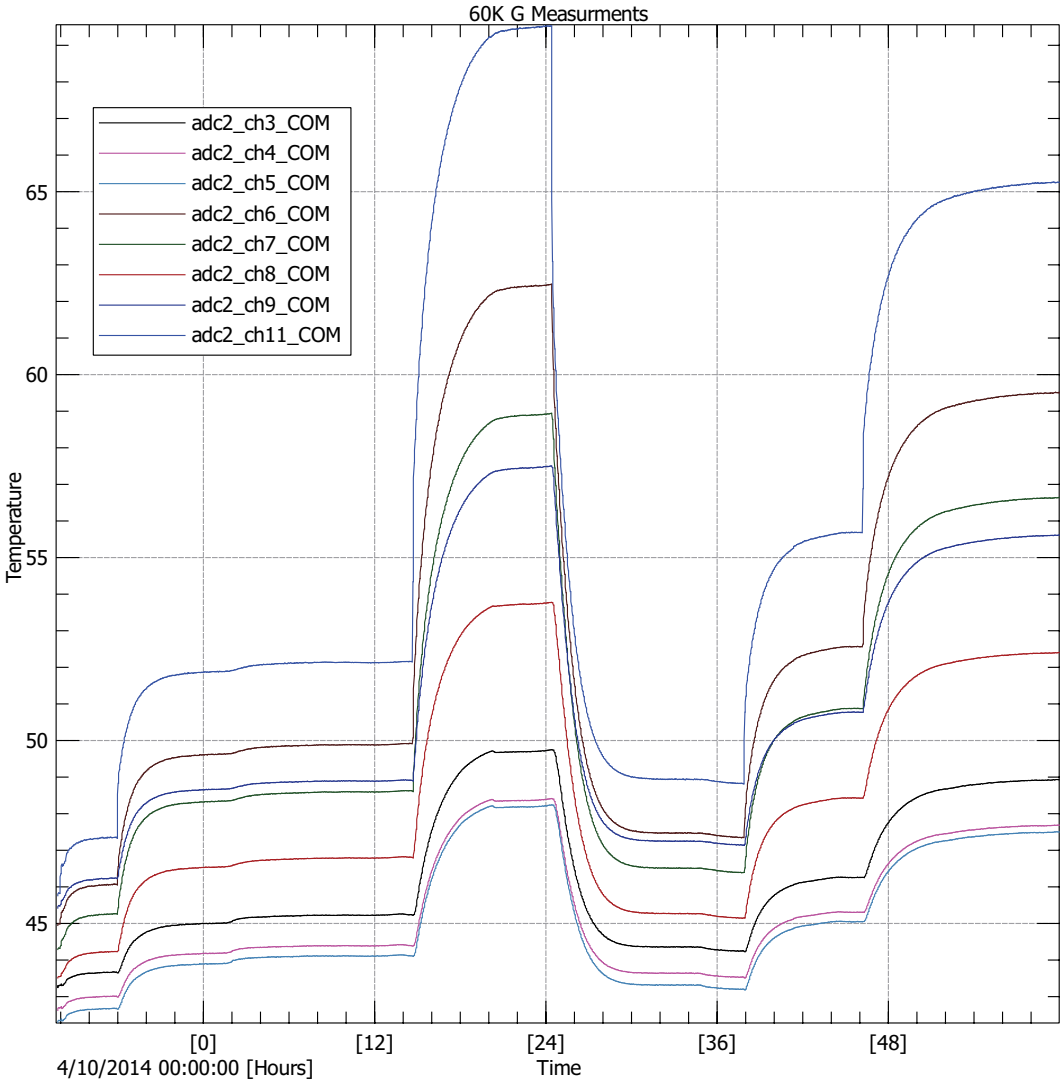


Figure 46: Temperature data collected on April $10^{th}$ $2014$.The plots show time, in hours since $0000$ GMT, vs. Temperature, in Kelvin. This is the raw data from which Figure 45 was produced. This plot was produced using KST2.

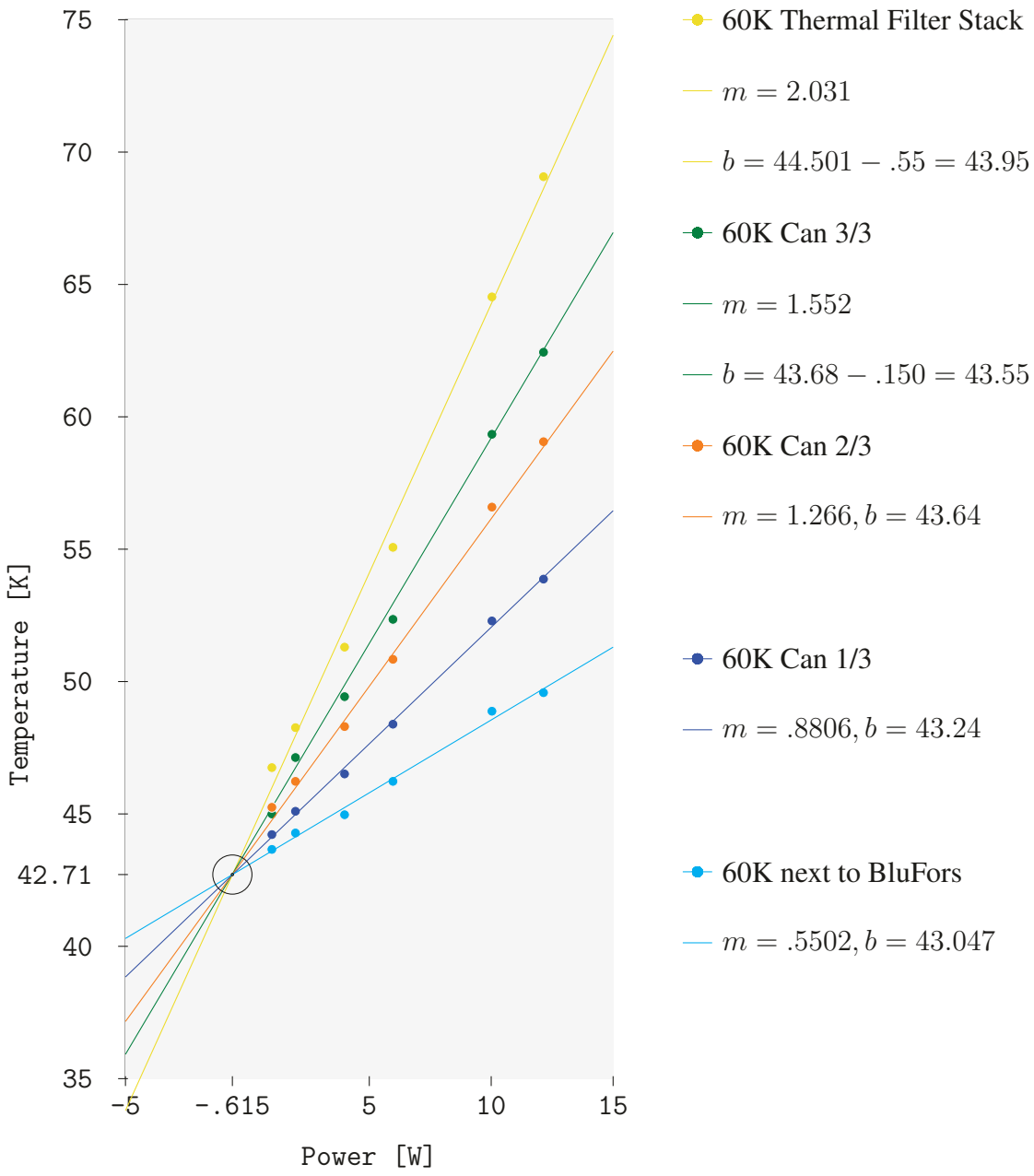


Figure 47: A relative calibration is performed on 60 K diodes. For reasons explained in the text, the 60K Can 0/3 thermometer is excluded.

| Location | a | b | c |
|---|---|---|---|
| 4K Thermal Filter Stack | $-9 \times 10^{-5}$ | 0.0370 | 2.5798 |
| 4K Can 3/3 | $-4 \times 10^{-5}$ | 0.0228 | 2.6890 |
| 4K Can 2/3 | $-4 \times 10^{-5}$ | 0.0194 | 2.0648 |
| 4K Can 1/3 | $-2 \times 10^{-5}$ | 0.0117 | 2.5165 |
| 4K Can 0/3 | $-5 \times 10^{-5}$ | 0.0051 | 3.2076 |
| SA Heat Sink | $-5 \times 10^{-6}$ | 0.0047 | 2.5081 |

Table 10: Fit Coefficients of $4$ K thermometers.

decreases. The final G value for the $4$ K can is given by:

$$G_{4\mathrm{K}} \approx 37 \frac{mK}{\mathrm{mW}} \,. \tag{72}$$

Similar analysis as presented in section 8.5.2 indicates that the $2/3$ thermometer reads relatively lower then the others. At these temperatures the rough $-0.5$ K offset is quite significant and should be noted with that particular diode. We confirm the $60$ K behavior on the $4$ K stage with the $0/3$ diode which is mounted identically to its sibling ont he $60$ K stage. It is exposed to radiation from the $60$ K stage and thus presents a large offset. Its thermal resistance behavior is identical to the diode on the series array heat sink, indicating that it does not suffer from a poor connection as the its $60$ K sibling.

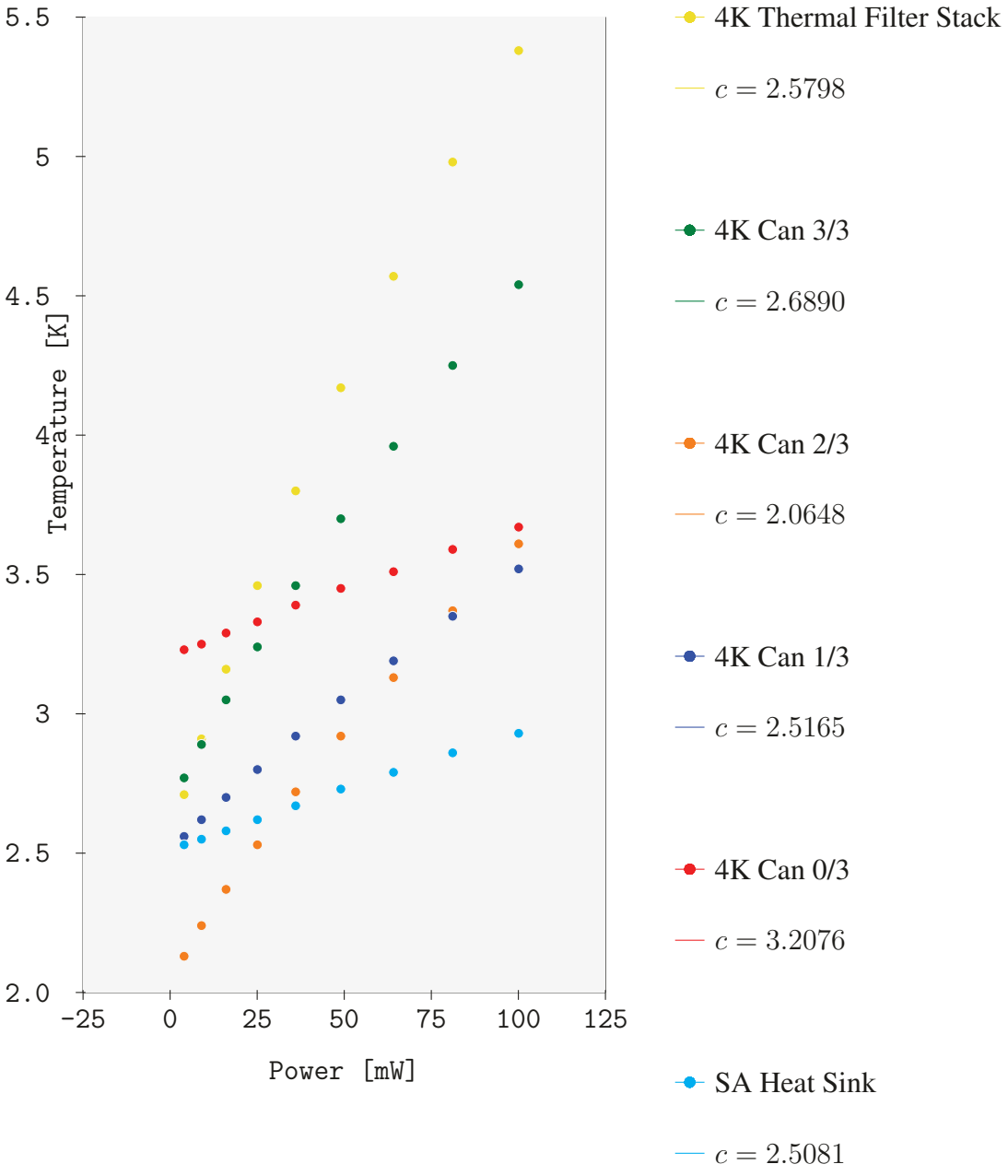


Figure 48: These are the results of the second loading test. Performed on Cryo One in April $15^{th}$.

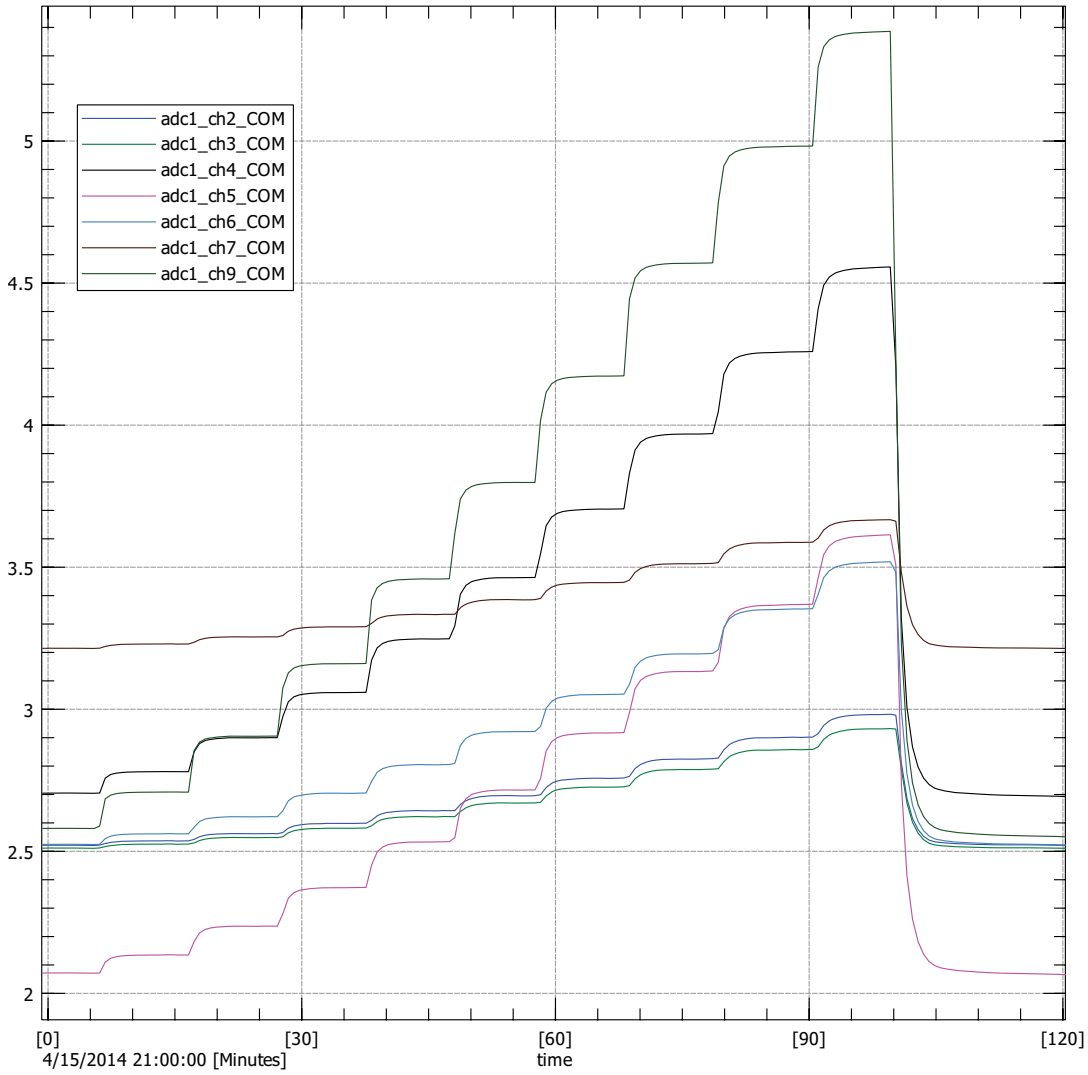


Figure 49: Temperature data collected on April $15^{th}$ $2014$. This plot shows time, in minutes, since $2100$ GMT, vs. Temperature, in Kelvin. This plot was produced using KST2.

### 8.5.4 1K Load Test

At the $1\ \mathrm{K}$ stage there was only one diode available. This diode was attached to the thermal filter stack. As we found on the $4\ \mathrm{K}$ stage, the G-value also showed a dependence on temperature, although a slightly smaller one then was exhibited on the $4\ \mathrm{K}$ stage. The fit values are given in figure 50. A value of

$$G \approx 22 \frac{mK}{\mu \mathrm{W}} \tag{73}$$

was derived for the $1\ \mathrm{K}$ stage.

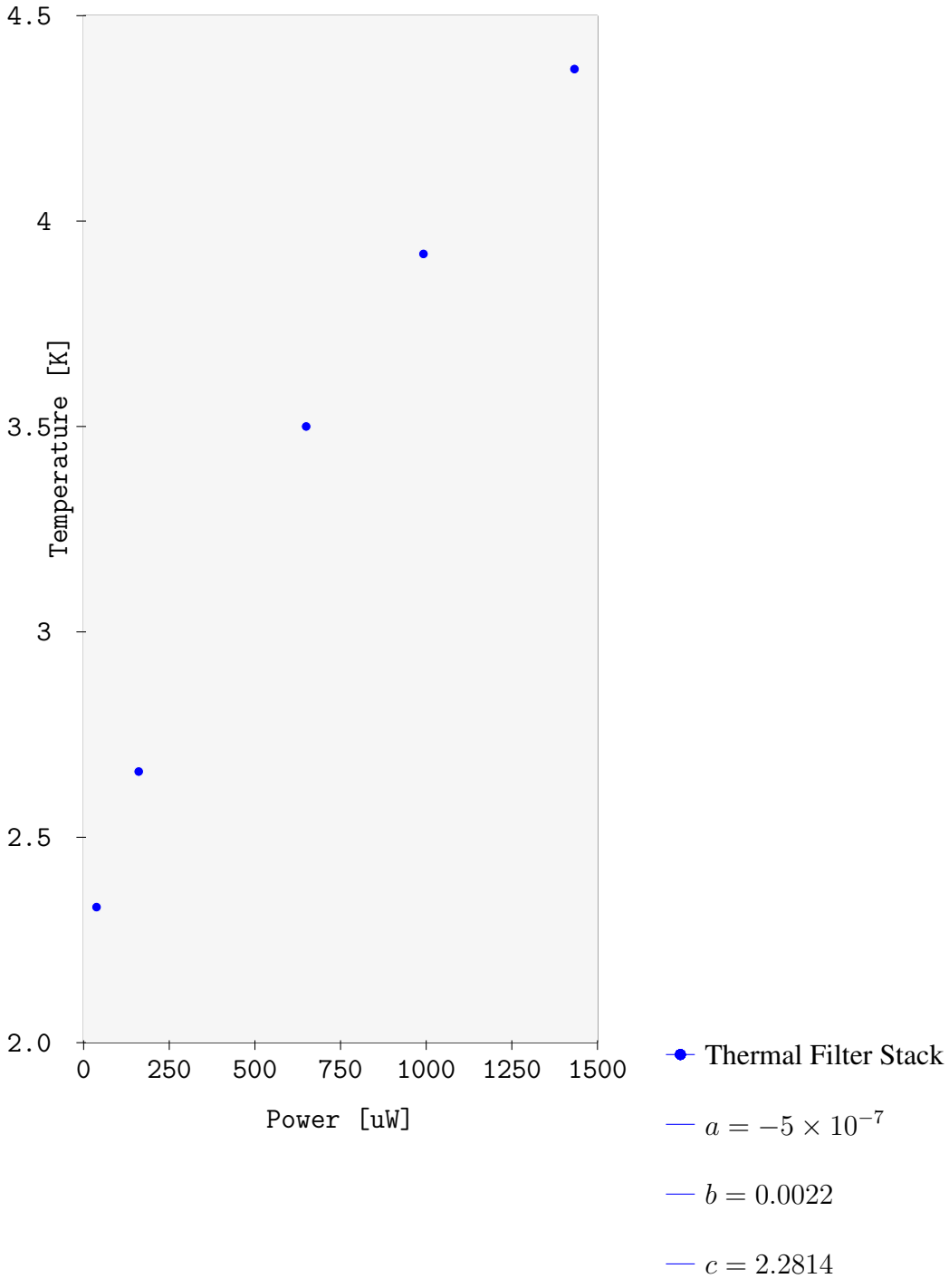


Figure 50: These are the results of the second loading test. Performed on Cryo One in April 2014.

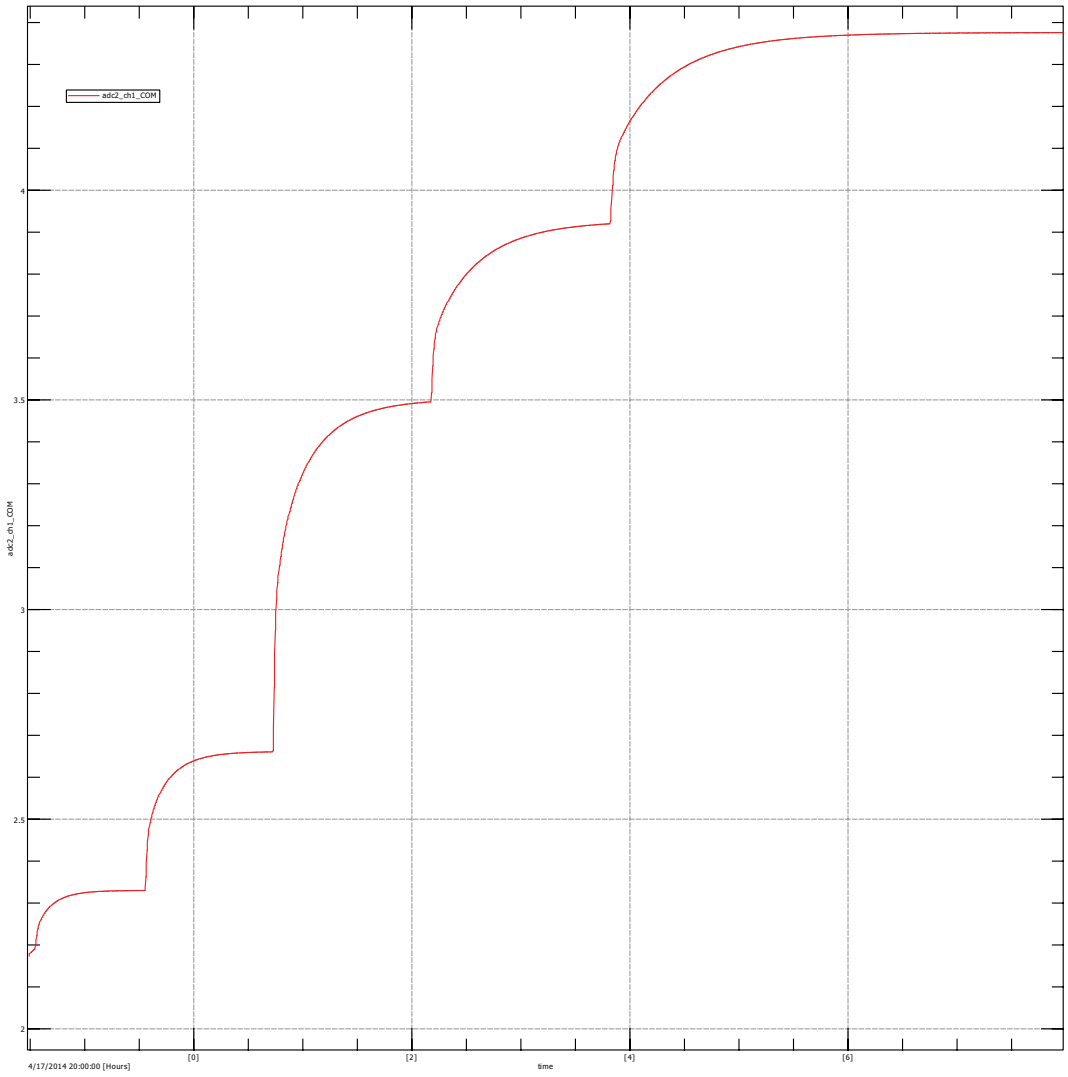


Figure 51: Temperature data collected on April $15^{th}$ $2014$. This plot shows time, in minutes, since $2100$ GMT, vs. Temperature, in Kelvin. This plot was produced using KST2.

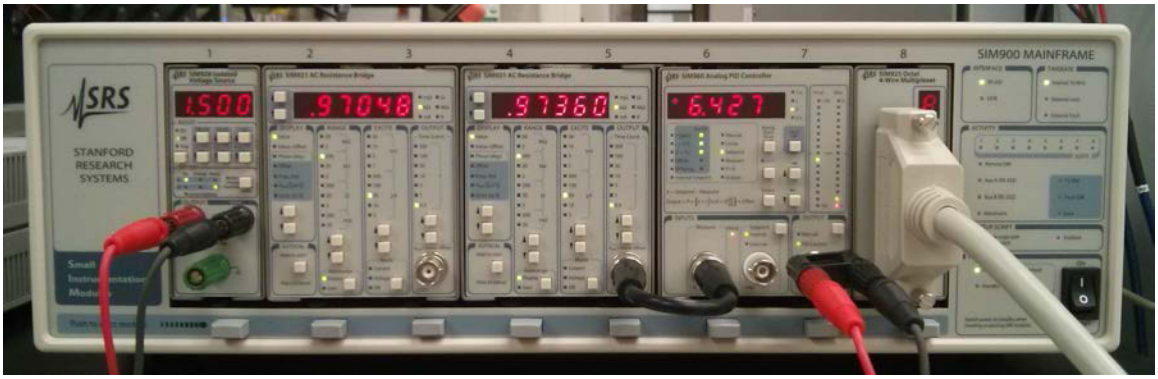


Figure 52: The Standford Research System Main Frame (SIM900), fully populated with the isolated voltage source (SIM928), two AC resistance bridges (SIM921), the PID controller (SIM960), and an octal 4-wire multiplexer (SIM925).

## 8.6 SRS Mainframe

The low temperature data acquisition and control is based on the Standford Research System's (SRS) SIM900 Mainframe. This mainframe is capable of accepting a variety of different modules. All temperature acquisition and control at temperatures of 1 K or less is accomplished via this system. The assembled system is shown in figure 52. In the following sections I will describe the individual modules and how the hardware ties into the CLASS control systems.

### 8.6.1 SRS Temperature Monitoring

The ROX thermometers are read out using two SRS AC resistance bridges (SIM921). The first bridge, in slot 2, is connected to the SRS octal multiplexer (SIM925), in slot 8. This combination is responsible for reading out eight ROX thermometers. Four are located on

the $1$ K stage and the other four are located on the $100$ mK stage.

### 8.6.2 SRS PID

To control the focal plane temperature an SRS analog proportional-integral-derivative (PID) controller is used. This controller is connected to a dedicated AC resistance bridge to allow for fast PID time constants. The AC resistance bridge provides the feedback to the PID loop. The PID module, `SIM960`, provides a voltage bias to a heater on the focal plane. The temperature of the focal plane is controlled by the PID varying the power dissipated across the focal plane heater.

### 8.6.3 SRS Voltage Source

A heater is placed on the still of the dilution refrigerator. This heater is necessary to increase the cooling power of the dilution refrigerator. The heater is typically biased with a $1.5$ V excitation via the `SIM928` isolated voltage source. This voltage source is powered from batteries and thus very low noise. The heater lines connected directly to BlueForse-provided wiring.

### 8.6.4 SRS Software

The user interface for the SRS system is implemented in three blocks. The low level communication and control of the SRS mainframe is accomplished via the SRS class, `SRS.py`. This class communicates over an RS-232 serial connection. The software commands are

based on the GPIB standard. A middleware class was necessary to tie together the low level commands implemented in the SRS class. This middleware, `srs_middleware.py`, is primarily responsible for translating high level commands and recording data to the NFS mount. Finally the SRS control class, `srs_ctrl.py`, ties this user interface into the PyRo control structure of CLASS.

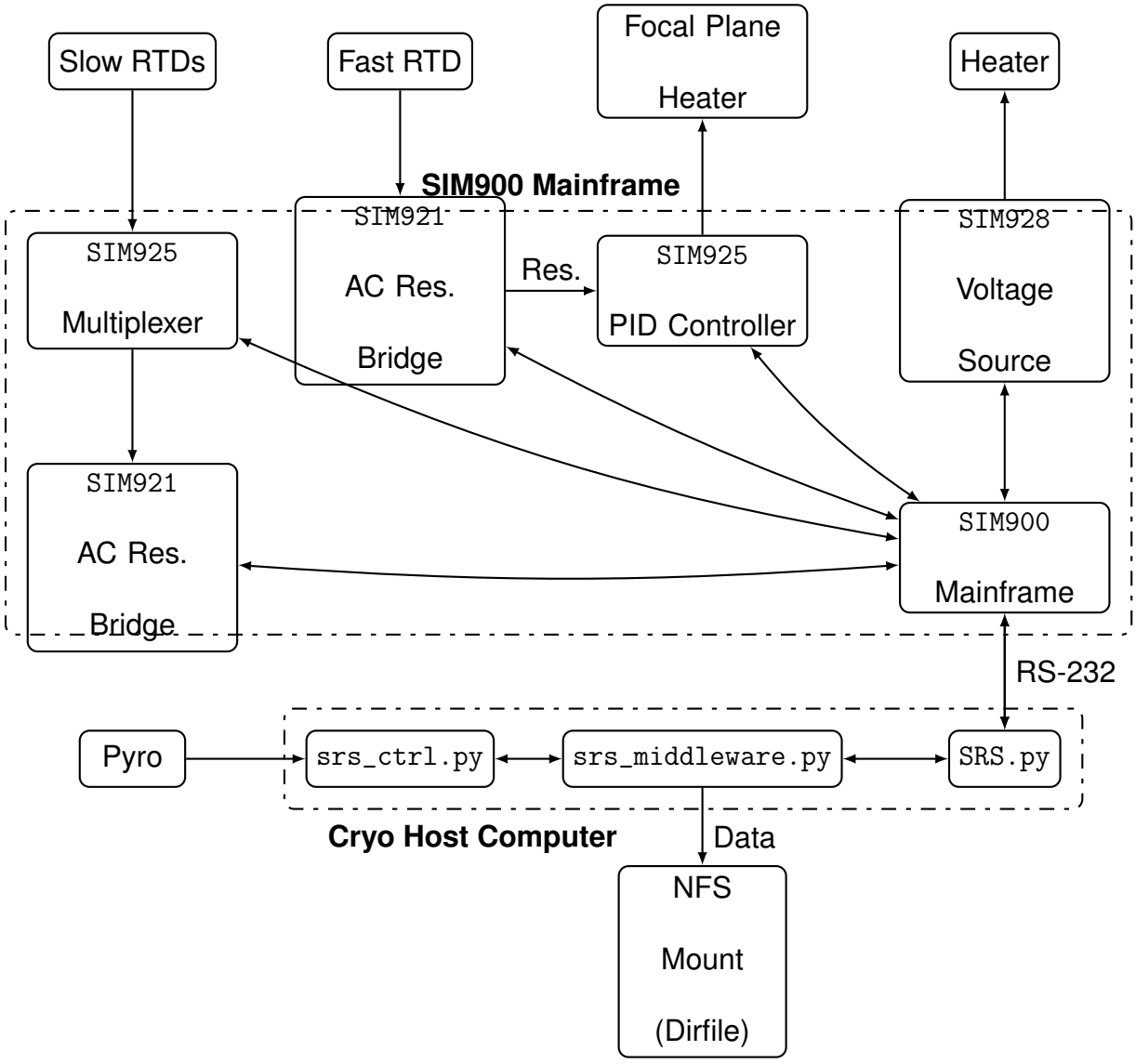


Figure 53: Schematic overview of the ruthenium oxide data acquisition system. [Diagram courtesy of Matthew Petroff.]

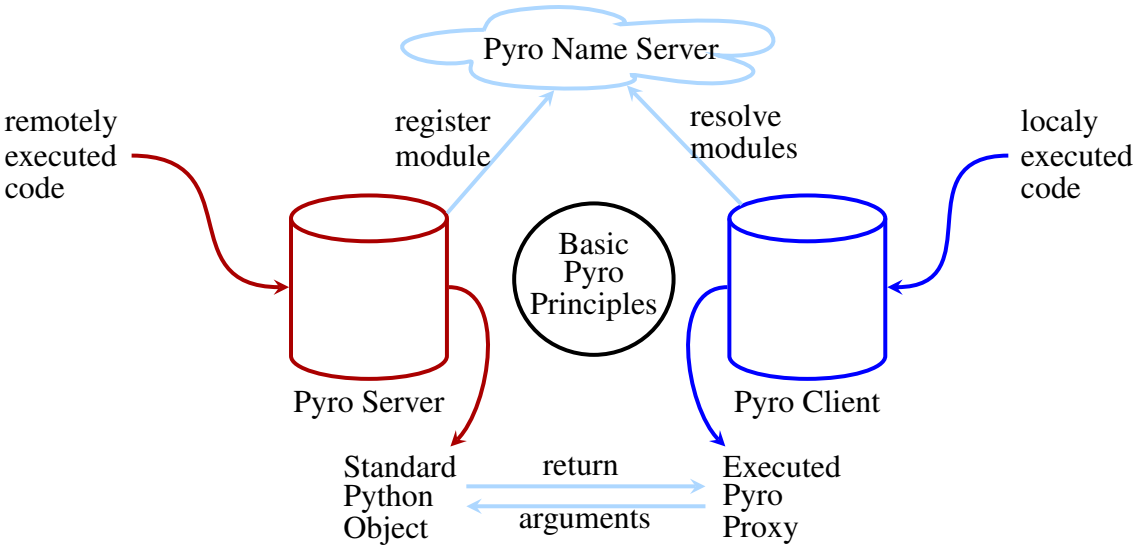


Figure 54: The relation between the Pyro Server, Client, and Name server are shown, including how information is passed via the Pyro interface. Locally, a Proxy object is executed, which communicates with a remote object living on the Pyro Server. The Pyro Client, executing the proxy object, is aware of all Pyro objects via the Pyro name server.

# 9 Site Software

The CLASS experiment requires the coordination of many separate subsystems in physically separated spaces. The hardware is controlled locally via python software packages. To enable the integration of all of these subsystems into a central scheduling network the Pyro package was deployed. Pyro[8] is a pure python software package that enables seam-

[8] https://pythonhosted.org/Pyro4/

less communication over a network. In this framework a local Pyro Client can execute an object on a remote Pyro Server. The arguments are passed to the server, where the remote object executes as a standard python object. Since the object is executed locally on the server it has easy and immediate access to hardware. The return statement of the object is then passed back to the Pyro Client. Pyro achieves this functionality by creating local Proxy objects on the Client. These proxy objects are linked to the remote object via a name server. Each new object registers itself with the name server. Once registered it can be called from any Pyro Client, just as a standard python object.

## 9.1 Pyro in the CLASS Infrastructure

We take the data acquisition of diode temperatures as an example to illustrate the two main architectural ways Pyro can be utilized. The premise is simple: a server needs to be able to start and stop the data acquisition of Sleipnir, connected to a remote machine. The two approaches center around who records the data, the client or the server. That is the pyro client could call a function `record_temp()` that would simply trigger the DAQ on the server. This function would return `void` and the server is responsible for recording the data, e.g., to an NFS mount. Alternatively Pyro can be used to pass messages back and forth. That is the client could execute the same function, but now it returns a temperature value over the Pyro network. The client would then be responsible for recording the data. For most of CLASS's subsystems the former approach has been chosen, due to already having a centralized data structure. Specifically the Pyro name-server runs on the primary

server named `Burgermeister`, as well as all Pyro clients. The Pyro Server, interfacing with Sleipnir, lives on one of the cryo-control computers, e.g., `MisterQ`. The proxy object executed locally on `Burgermeister` serves as a start or stop signal for the Pyro server living on `MisterQ`. The Pyro Server then acquires and records the data directly to an NFS mount, until it is signaled by the Pyro client to stop the acquisition.

## 9.2 Network Considerations

The deployed network consists of four primary locations: the two mounts, the control room, and the gateway site in a nearby city. In the next sections I will describe give an overview of each of these blocks and how they tie together. A schematic overview is shown in figure 55.

### 9.2.1 WiFi Link

The deployed network consists of two sites connected via a WiFi link. The main experimental site has no internet access, therefore a link has to be created to a nearby town. This WiFi link has to bridge a roughly $40\ \mathrm{km}$ distance. Two $1.5\ \mathrm{m}$ diameter dishes are used to focus the standard $1\ \mathrm{W}$, $2.4\ \mathrm{GHz}$ RF output of the Ubqiuity Bullet, `BM2-Ti` WiFi bridge. At $48\ \mathrm{Mbps}$ this radio achieves an average $24\ \mathrm{dBm}$ transmit power and a $-77\ \mathrm{dBm}$ receive sensitivity. Given the $30\ \mathrm{dBi}$ gain of the antennas and the $133\ \mathrm{dBi}$ free space loss of the $40\ \mathrm{km}$ air-space, the system still maintains a positive $28\ \mathrm{dB}$ headroom above the necessary signal-to-noise ratio required by the chosen radios. This headroom should provide

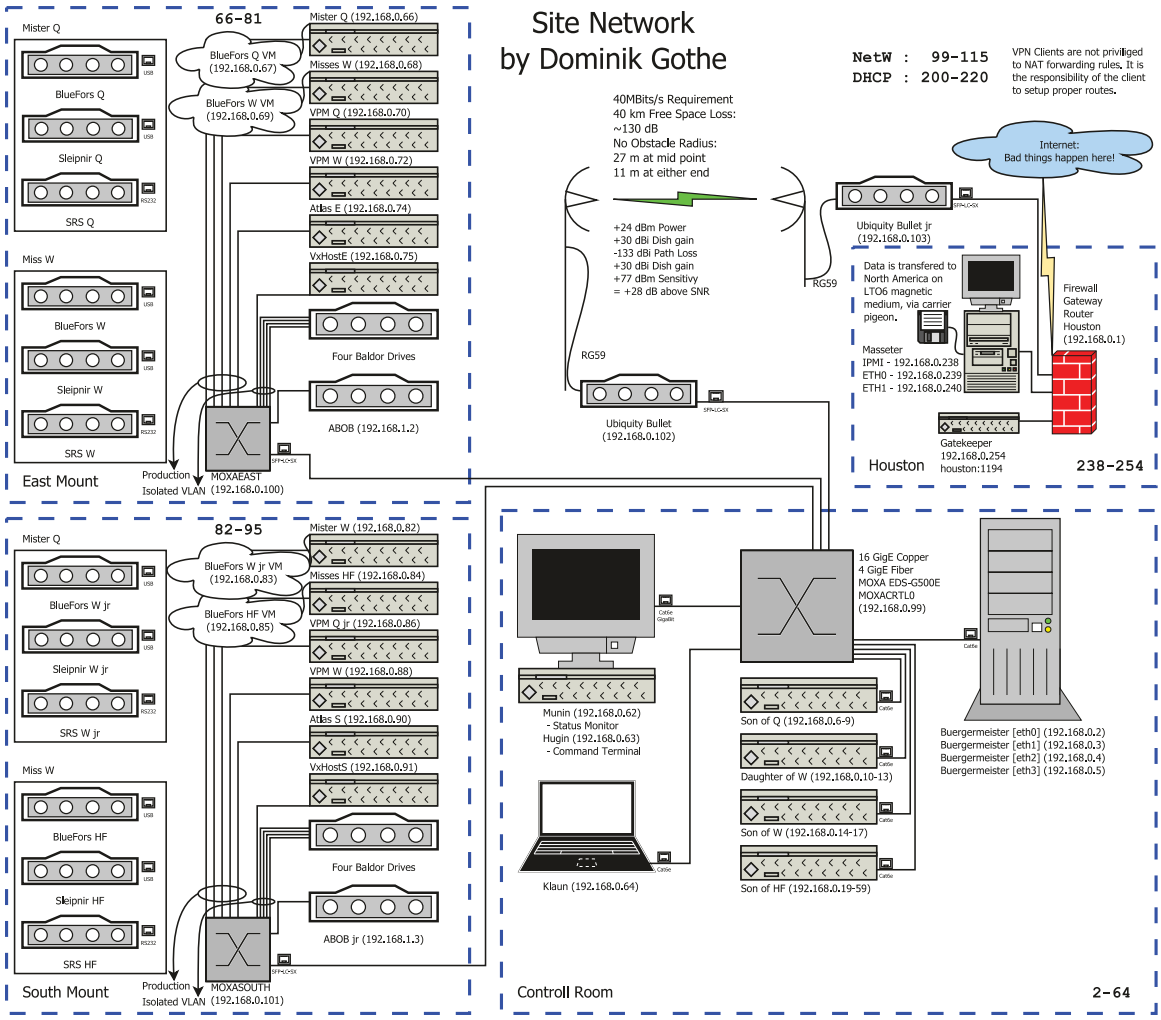


Figure 55: A schematic representation of the entire CLASS network. This diagram follows a physical layout. The two mounts are represented as the East and South Mount. The location off-site is represented by the box labeled "Houston". The wireless link between the site and Houston is also shown including required WiFi power calculations. The network is built around the industrial Moxa switches, `EDS-516E-4GSFP-T`. These are 12 port gigabit switches with two fiber links. The switches are rated for extreme temperatures ($-40^\circ$ to $75^\circ$) and accept redundant power supplies.

tolerance against varying weather conditions.

### 9.2.2 Switch Gear

On the main experimental site, the network is built around industrial ethernet switches, specifically three Moxa `EDS-516E-4GSFP-T`. One switch is place on each mount and another in the control room. These switches operated under extreme temperatures ($-40^\circ$ to $75^\circ$) and accept redundant power supplies. This hardware was chosen due to the harsh conditions in the Atacama desert and the need for 24/7 up-time. These switches have the additional convenience of built-in fiber channels. A single fiber cable is run between the control room and each mount. A third fiber connection galvanically isolates the WiFi antenna sub-system from the control room electronics. This is necessary as the WiFi tower is a potential lightning rod.

### 9.2.3 Overview of the Mount Networks

Each mount houses two cryostats and their supporting infrastructure. Each cryostat is accompanied by a cryostat control computer. This computer interfaces with the SRS and Sleipnir while simultaneous hosting a Virtual Machine. The Virtual Machine is necessary to run the Bluefors software to cycle the cryogenic system. A mount control computer takes in information from an analog break out box (ABOB) as well as the four servo drives driving the mount axes. This computer runs the VX-Works real-time operating system. A host computer is necessary to boot the VX-works computer. To prevent network resource

competition, the mount control computer and the four servo drives are on an isolated virtual LAN network. Additionally an ethernet device is required to interface with the VPM associated with each cryostat.

### 9.2.4 Overview of the Control Room Network

The control-room provides the required infrastructure to monitor and command the experiment. It also houses the MCE computers and the main computer responsible for scheduling and control. Data display is handled via a dedicated computer. A dedicated computer is set up acting as a command terminal. Finally there will be a laptop to be used by operators for non-mission critical tasks.

## 9.3 Beefy Miracle

Named after the $17^{\text{th}}$ release of Fedora, Beefy Miracle[9] is the underpinning of the CLASS control infrastructure. It's purpose is to provide a singular interface for all CLASS subsystems, that is both usable directly by an operator as well as an intelligent scheduler. The software, is based on a command line argument parsing utility. This allows BeefyMiracle to be executed like a standard Linux command. On `hugin`, the dedicated terminal, it is even added to the variable path allowing for tab completion. The program is very user-friendly, providing help information at every step. To reduce clutter all commands are categorized through several layers representing main systems. Once fully implemented the first strata

[9] https://beefymiracle.org/

will consist of the following:

- MountE, the first of the two mounts.
- MountS, the second mount.
- MisterQ, the first receiver, housing the Q band electronics.
- MissW, the second receiver, housing the W band electronics.
- MisterW, the third receiver, housing the second set of W band electronics.
- MisterHF, the fourth receiver, housing the high-frequency electronics.
- Burgermeister, the main server coordinating the CLASS schedule.

To help the operator these items, with a description can be pulled up via the `-h`, help option.

```
sigurd@hugin ~ $ BeefyMiracle -h
usage: BeefyMiracle [-h] [-version] {MisterQ,MissW,Burgermeister} ...


positional arguments:
  {MisterQ,MissW,Burgermeister}
                        Major Systems
    MountE The first, or east mount.
    MountS The second, or south mount.
```

```
    MisterQ             Cryostat One. MisterQ. 40GHz Cryostat.
    MissW               Cryostat Two. MissW. First 90GHz Cryostat.
    MisterW             Cryostat Three. MisterW. Second 90GHz Cryostat.
    MisterHF            Cryostat Four. MisterHF. HF Cryostat.
    Burgermeister       Main server.


optional arguments:
  -h, --help            show this help message and exit
  -version              show program's version number and exit
```

Any one of these subsystems is then divided into controllable instruments. For example the Q-band receiver, `MisterQ` has four instruments attached, Sleipnir, the SRS, the MCE, and the VPM. Again a list of the instruments can be retreived via the help command.

```
sigurd@hugin ~ $ BeefyMiracle MisterQ -h
usage: BeefyMiracle MisterQ [-h] {Sleipnir,SRS,MCE} ...


positional arguments:
  {Sleipnir,SRS,MCE}  Instruments
    Sleipnir          Sleipnir: the diode readout electronics.
    SRS               SRS, the RuthiniumOxide readout electronics.
    MCE               MCE: the detector readout electronics.
    VPM               VPM: the Variable delay-Polarization Modulator.
```

```
optional arguments:

  -h, --help          show this help message and exit
```

Any given instrument can then be queried for commands via the help option. For example Sleipnir only has a start and stop function.

```
usage: BeefyMiracle MisterQ Sleipnir [-h] [-start] [-stop]


optional arguments:

  -h, --help  show this help message and exit

  -start      Begin diode data aquisition.

  -stop       Stop diode data aquisition.

sigurd@hugin ~ $
```

## 9.4 Data Structure

All of CLASS data are stored in a binary, data-base like, directory file structure known as *DirFile*[10]. This system was designed for time ordered synchronous data. Non-synchronous and multiplexed data creates problems as discussed in section 8.4.3 and 8.6.4. It is a convenient format as it uses no encoding, thus making it easy to read and write, and also offers standard ways to display the data.

[10] http://getdata.sourceforge.net/DirFile.html

| Data Stream | Data Width | Multiple | Throughput |
|---|---|---|---|
| MCE 40 GHz | 32 bit | 72 | 237.5 Kbps |
| MCE 90 GHz One | 32 bit | 518 | 3237.5 Kbps |
| MCE 90 GHz One | 32 bit | 518 | 3237.5 Kbps |
| MCE 150 GHz | 32 bit | 1190 | 7437.5 Kbps |
| MCE 220 GHz | 32 bit | 1190 | 7437.5 Kbps |
| Azimuth Encoders | 32 bit | 2 | 12.5 Kbps |
| Elevation Encoders | 32 bit | 2 | 12.5 Kbps |
| Boresight Encoders | 32 bit | 2 | 12.5 Kbps |
| VPM Encoders | 64 bit | 12 | 75.0 Kbps |
| GPS Time | 64 bit | 2 | 12.5 Kbps |
| Sync Pulse | 32 bit | 2 | 12.5 Kbps |
| Total | | | 21725.0 Kbps |

Table 11: All science data is recorded synchronously with the 200 Hz sync pulse. The data displayed in this table are necessary for science results and indicates a throughput of roughly 22 Mbps at full deployment.

### 9.4.1 Overview

The science data that is essential for map-making includes the detector data, pointing information, VPM position and GPS time. All the science data systems have to be sampled on a synchronous clock to avoid the introduction of systematics. This is accomplished by

the use of the Sync Box. The Sync Box generates a serial number at a rate of 200 Hz. All science systems are sampled synchronously with this clock and are identified by the serial number. Additionally the GPS time is also sampled synchronously, allowing a precision correlation between Sync Box stamp and real time. It is this ability to know precisely at what time each sample was taken that will allow us to make maps with a minimum of systematics. See table 11 for an overview of the science data and projected bandwidth requirements.

The additional data consists of housekeeping information, mostly only useful for debugging of the system. This data includes the Mount system, ABOB, Cryogenics, Weather Hawk, and auxiliary data. These data are not taken synchronously with each other or the main system. It would be difficult to do this and there is no systematic requirement for it. The data rates for these systems are also vastly lower; some fields will be recorded at a rate less then 1 Hz. This data will not contribute significantly to the bandwidth requirements.

### 9.4.2 Science Data

The primary science data, the detector values, are recorded by the multi-channel electronics (MCE). The encoders, sync pulse, and GPS time are all recorded by the mount control computer `Atlas`, see section 9.6.8 for details on the recording implementation. It is necessary for Atlas to manage this data as the characteristics of the real-time-operating-system VxWorks are required for synchronous data acquisition. As mentioned earlier all science data are recorded at 200 Hz allowing for a Nyquist-Shannon bandwidth of up to 100 Hz.

Care must be taken to avoid analog bandwidths that exceed the Nyquist-Shannon limit, or aliasing will introduce unnecessary systematics. The first cryostat, the $40\ \mathrm{GHz}$ radiometer, will be fielded with $36$ polarimeter pairs. This accounts for the $72$ separate detectors shown in table 11.

### 9.4.3 Additional Mount Data

There is an analog breakout box (ABOB) monitoring analog signals relevant to the health of the mount. This includes power supply voltages and the mount's temperature. A Weatherhawk Model 232 weather station[11] is used to monitor environmental conditions such as temperature, humidity, pressure, solar radiation, rainfall, wind speed, and wind direction. Both of these systems sample at less then $0.1\ \mathrm{Hz}$ and therefore do not significantly contribute to the data bandwidth requirements.

### 9.4.4 Cryogenics

Cryogenic data consist of three subsystems: the diode system, the SRS system, and the BlueFors system. The diode system acquires temperature data down to $4\ \mathrm{K}$ At the $1\ \mathrm{K}$ and $100\ \mathrm{mK}$ stage the SRS system records temperature via the Lakeshore ROX thermometers. The BlueFors system, controlling the cryogenic cycle, records relevant information such as pressure and helium flow rate.

[11] WeatherHawk, 815 W 1800 N, Logan, UT 84321

## 9.5 Data Storage and Handling

### 9.5.1 Storage

CLASS adopted an approach of centralized storage. Science data are never stored locally, and thus fragmented, instead, it is stored on a central file server. This is achieved via the NFS protocol version 3. This raw data is written to *uranus* on `Bürgermeister`.

`Bürgermeister` has four physical gigabit interfaces. These four interfaces are used to segment the data flow into three distinct groups: data collection, data archiving, and data visualization. This segmentation ensures that the three tasks do not interfere with one another. In other words, the bandwidth for any given task is guaranteed, no matter what demands other tasks place on the network. Currently two interfaces are dedicated to data collection, one for visualization, and one for the downlink to *Houston*. Should four gigabit connections not suffice, `Bürgermeister` is provisioned to easily scale to eight or up to sixteen gigabit total aggregate throughput, through the use of up to three quad gigabit PCI-E Network Interface Cards (Intel E1G44HT).

The raw data structure, as represented by the folder structure in *uranus*, follows a hierarchical structure, placing the subsystem at the top of the hierarchy. This was chosen, versus the user friendly structure with time stamps as the top node, so as to avoid any possible human error corrupting data. A subsystem-first approach allows the NFS server to only serve those directories that are needed by the subsystem. Thus, the subsystem is not capable of writing to the wrong directory and thus corrupting data.

```
sigurd@burgermeister:~$ cd /mnt/

sigurd@burgermeister:/mnt$ ls

drwxrwxr-x 2 root control 4096 Sep 26 12:18 neptune

drwxrwxr-x 2 root control 4096 Sep 26 12:23 pluto

drwxrwxr-x 6 root control 4096 Sep 24 14:29 uranus
```

Aside from `/mnt/uranus` `Bürgermeister` also has `/mnt/neptune`, to serve as scratch space in preparing archivale data, and `/mtn/pluto` to server as a general, temperorary, scratch space. *uranus* and *neptune* differ not only in there data structure (uranus -> misterQ -> diode -> time stamp vs neptune -> times tamp -> diode -> misterQ ), but neptune is not accessible by anyone other then *Bürgermeister*. The data on *neptune* is also compressed, preparing it for transmission via the wireless link.

### 9.5.2 Bürgermeister RAID Configuration

`Bürgermeister` acts as the data storage server for CLASS on the mountain site. The details of this implementation are found in Section 9.4. `Bürgermeister` has one $128$ GB Samsung 840 Pro SSD, acting as a system drive, accessible via a hot swap bay. Additionally `Bürgermeister` has hardware RAID implemented by an ASUS Pike 2008/IMR 8-port SASII. There is a provision for eight hot swap $512$ GB to be connected to this RAID array. The hardware RAID array is configured in its own bios and thus no software configuration is required. Currently the RAID array is populated with four $512$ GB Samsung 840 Pro SSDs to provide a $2$ TB disk array. This RAID array is mounted in the OS at the mount

point $/mnt$ via the following fstab entry:

```
/dev/sdb1        /mnt/uranus     ext4    noatime      0          2
```

## 9.6 Low-Level Mount Control

The telescope mounts are controlled by the Atlas computers. There are two physical computers, *AtlasE* (192.168.0.74) and *AtlasS* (192.168.0.90), corresponding to the east and south mounts. See section 9.2 for more information. The Atlas computers run VxWorks, a modular and scalable real-time operating system (RTOS). This structure is necessary to allow for synchronous control of CLASS subsystems. Atlas ships with a shell that allows the operator to control the telescope via several built-in functions. This shell is callable via the terminal by the C-command, *mc_shell*. This shell can be queried (*?*) to list the built-in commands.

```
-> mc_shell

> ?

Shmem commands

    Ephem Sky Source Telescope PModel Azimuth Elevation Boresight

    SyncBox TimePlace DataCollection TiltMeters FivePoint AzScan

    DecScan DriftScan SkyDip ProfileScan StarCam QBand
```

Accessing Atlas is possible via telnet and a hardwired terminal. Telnet is available from any computer on the network and as such a simpler and more preferable method. The

hardwired terminal is accessible via the *vxhost* and should only be used for init-commands and as a backup option to the telnet and TCP interface. The terminal, only supports one connection. See section 9.8 for details on the TCP interface.

### 9.6.1 Start Up

Upon boot of the Atlas system, the various modules have to be loaded and started. It is advisable to do this via the terminal instead of a telnet session. The programs will periodically print debug information to the screen in which they were started. By following the best practice of starting in the terminal, the debug information stream will never be lost and can always be read by attaching a console. Attaching to the terminal is easy with the preconfigured Kermit file. From the home directory of *vxdev* on *VxHost* simply execute *./vxcon*. In this terminal the operator should now load all modules and start the update, track, mount control, and mc-server via the following sequence.

```
-> < load_all
-> updatE_start
-> track_start
-> mc_start
-> mcserver_start
```

Note that I have omitted debug outputs for brevity. Loading all of the modules takes several seconds. We also note that *track* is synchronized with *update*, therefore track has to be started after update and stopped before update. The finite state machine that controls

the mount is *mc*, short for mount-control. The TCP server is started by the command *mcserver_start*.

### 9.6.2 General Notes

The mount control software is based on a shared memory infrastructure. That is, all relevant variables are stored in custom data structures in shared memory. These $2\mathrm{MB}$ of random access memory (RAM) are periodically written to the *VxHost*. This allows *Atlas* to load the last configuration at boot. Each shared memory object, *Shmem commands* from section 9.6, can be read (*get*), written (*set*), and executed. Calling the object without a *set* or *get* prefix will call the objects exec function. The object values can also be set via the execute function. Each object will store an error number (*Errno*), error-method (*Errmethod*), error message (*ErrMsg*) and a program ID (*PgmID*). During normal operation these variables can be glanced over; they only provide debug information. In the following sections I will detail the important mount control commands. Providing a list of relevant inputs and example usage.

### 9.6.3 The Screen Program

The screen program can be monitored by typing *screen_start* in the c-shell. Note this is not a command to be entered into the mc_shell.

```
-> screen_start
```

The screen program accepts three basic commands, *1*, *2*, and *r*. These commands are entered by simply entering the corresponding keys and sending the return character. The

commands *1* and *2* will switch between the first and second screen. The first screen shows pointing information:

```
                          *** Mount 1 ***
DATE     MAR 02, 2015  UT1   22:39:31.7   OPERATOR None                   Idle
SOURCE   Tau A         LST    4:49:52.9   AZ EL    Main    Halt  SCAN   1 of   0
RECEIVER StarCam       BEAM   0     9                                     21.0

            RA           DEC                  AZ         EL                BORE
2000.00   4:49:22.2   -22:58:44   STATE         Off        Off  STATE        Off
2015.16   4:43:13.7   -24:14:10   REQUEST  230.0000    90.0000  REQUEST     0.00
READOUT   4:50:18.6   -22:53:33   OFFSET     0.0000     0.0000  READOUT    16.23
           SUN 20       MOON      PCOR       0.5245    -0.0580  ERROR      16.23
RA       22:52:54.5    8:53:02.9  COMMAND  230.5245    89.9420  RATE       0.000
DEC      -7:07:45     13:31:31    READOUT  230.5254    90.0459   PTG OFFSETS
AZ       263.8564      64.8934    ERROR      0.0010     0.1060  AZ     0.0000
EL         3.5848      20.1013    RATE       0.0000    -0.0040  EL     0.0000
ANGLE     86.5787      69.7946                   1     0.0002
STATE       Cle77        Cle49
```

The second screen shows servo information:

```
                          *** Mount 1 ***
DATE     MAR 02, 2015  UT1   22:40:27.7   OPERATOR None                   Idle
SOURCE   Tau A         LST    4:50:58.0   AZ EL    Main    Halt  SCAN   1 of   0
RECEIVER StarCam       BEAM   0     6                                     21.0
                                  SYSTEM
SERVO POWER Good  BRAKE RELAY POWER Down  OPERATING LINE Down  ESTOP Active
MESSAGE Emergency Stop

                        AZ                 EL          BORE
                MASTER      SLAVE
```

```
BUS VOLTS        0.0         0.0         0.0          7.7
VOLTAGE          0.0         0.0         0.0          0.0
CURRENT       -0.012       0.013       0.047        0.008
SOFT LIMIT     0.016  Ok      06         095       -0.034
ELEC LIMIT            Ok                 Ok           Ok
MECH LIMIT            Ok                 Ok           Ok
BRAKES             Engaged            Engaged      Engaged

AZ   MESSAGE DisableServo:Slave:Powerdown::GetError:code 10012 Power base is not
EL   MESSAGE Ok
qORE MESSAGE Ok
```

The drawing of the screens can be refreshed by submitting the *r* command. Both of these screens should always be monitored by the operator. There is no limit to how many screen programs can be running concurrently.

### 9.6.4 The Telescope Object

The Telescope object defines the telescope name, *Telescope*, which should be set to either *Mount_1* or *Mount_2*. This will correspond to the DirFile names. This and most of the other parameters are monitored via the screen program. It is most important for the operator to specify the *Operator* field according to the operator's name. When the operator has finished commanding the telescope, the *Operator* field should be set to *none*. A "none" operator indicates to other users that the telescope is not in use. If the telescope is being commanded by higher level software the operator field will either read *BeefyMiracle* or *Scheduler*, depending on the originating entity taking control. The pointing tolerances are also set in this object. If the pointing tolerances are exceeded the telescope will not go into the tracking mode. Finally the telescope can either be commanded to halt or point. When the *Point* field is set to *Point* the software will attempt to point at the commanded position. When the field is set to *Halt* the telescope will halt all movement. Finally the telescope can

also be put into a stow and service position by setting the *Point* field to *Stow* and *Service* respectively. The stow and service positions are set for each axis independently, see section 9.6.7.

```
Telescope  -Status OK -Abort false -Errno 0 -Errmethod "null" -ErrorMsg "OK"
 -TimeFrac 0.725 -AzCom[0] 180 -AzCom[1] 180 -AzCom[2] 180 -ElCom[0] 45
 -ElCom[1] 45 -ElCom[2] 45 -BoreCom[0] 0 -BoreCom[1] 0 -BoreCom[2] 0
 -AzVelCom[0] 0 -AzVelCom[1] 0 -ElVelCom[0] 0 -ElVelCom[1] 0 -BoreVelCom[0] 0
 -BoreVelCom[1] 0 -AzReadOut 130.0 -ElReadOut 60.0 -BoreReadOut 0.0
 -RaReadOut  06:11:48.22 -DecReadOut -39:22:08.5 -AzError -50.5 -ElError 0.8
 -BoreError 0.0 -AzErrInt 0 -ElErrInt 0 -AzOld 0 -ElOld 0 -AzReadOld 130.0
 -ElReadOld 60.0 -AzVelocity 0.0 -ElVelocity 0 -AzRate 0.0 -ElRate 0.0
 -BoreRate 0.0 -AzAvgRate 0.0 -ElAvgRate 0.0 -BoreAvgRate 0.0 -PointingTolerance 1
 -AzPC 0 -ElPC 0 -AzCor 0.0 -ElCor 0.0 -AzPoff 0 -ElPoff 0 -Point Halt
 -AzSoftLimit Error -ElSoftLimit Error -AzElecLimit Error -ElElecLimit OK
 -DIOInputs 0x6020 -DIOOutputs 0x0 -SystemStatus[0] 0xEC0C0C0
 -SystemStatus[1] 0x8111 -PointError Good -ElevationHold true -ServoPower Good
 -OperatingLine Good -BrakeRelayPower Good -EStop Ok -Telescope "Mount_1"
 -Operator "Dominik_Gothe"
```

Since the telescope name should never be changed the only relevant telescope commands are setting the operators name and indicating the pointing mode.

```
set Telescope -Operator Dominik_Gothe -Point Stow
```

### 9.6.5 The Sky Object

The Sky object is the primary object that keeps track of on sky locations. As such it will compute the equatorial coordinates in both the J2000 epoch and the current epoch. All of this information is displayed on the screen program as well. An operator would likely not use the get command to query positions. Since the Sky object also keeps track of the sun

and moon location it is also responsible for sun and moon avoidance. The avoidance angles for the both the sun and moon, *SunAvoidAngle* and *MoonAvoidAngle* can be adjusted by setting their respective parameters. The moon avoidance algorithm can also be completely turned off by setting the boolean flag, *AvoidMoon* to false. The sun avoidance algorithm can not be disabled. When the operator points the telescope in the azimuth and elevation system the requested position is specified in the Sky object, via *AzReq*, *ElReq* and *BoreReq*. Note that the requested positions are stored in a two-vector, *Req[0]* and *Req[1]*, corresponding to the main position the reference position. These two positions can easily be switched between by setting the *Position* keyword to either *Main* or *Ref*.

```
Sky  -Status OK -Abort false -Errno 0 -Errmethod "null" -ErrorMsg "OK"
 -AzReq[0] 180 -AzReq[1] 130 -ElReq[0] 45 -ElReq[1] 60 -BoreReq[0] 0
 -BoreReq[1] 0 -AzOff[0] 0.355 -AzOff[1] 0 -ElOff[0] 14.25 -ElOff[1] 0
 -RaOff[0]  00:00:00.00 -RaOff[1]  00:00:00.00 -DecOff[0]  00:00:00.0
 -DecOff[1]  00:00:00.0 -Dl[0] 0 -Dl[1] 0 -Db[0] 0 -Db[1] 128.8929715
 -Ra2000[0]  04:10:30.47 -Ra2000[1]  06:15:44.05 -Dec2000[0] -67:59:26.5
 -Dec2000[1] -39:18:53.6 -RaCom  04:10:32.05 -DecCom -67:57:34.5 -LCom 281.1
 -BCom -39.6 -RaNow[0]  04:08:08.12 -RaNow[1]  06:16:15.23 -DecNow[0] -53:42:22.5
 -DecNow[1] -39:19:39.4 -SunAvoidAngle 10 -RaSun  22:26:29.42 -DecSun -09:45:30.7
 -RaSunNow  22:27:16.27 -DecSunNow -09:40:54.3 -AzSun 262.7 -ElSun 7.6
 -SunAng 102.7 -MoonAvoidAngle 10 -RaMoon  02:42:48.85 -DecMoon  13:31:41.1
 -RaMoonNow  02:43:38.57 -DecMoonNow  13:35:23.7 -AzMoon 327.7 -ElMoon 47.7
 -MoonAng 71.3 -SunMoonAng 67.7 -ObsVel 1.1 -BaryVel -3.1 -Refrac 136.1
 -ParAng 0.94 -GalAng -118.05 -ComAng -89.99 -ElClip 88 -Position Main
 -RaSys Coord -AzSys Sky -MovPos 0 -SunState Clear -MoonState Clear -AvoidMoon Off
```

- The requested angles, *AzReq[]*, *ElReq[]*, and *BorReq[]* are set in degrees.
- The soft and hard limit on the azimuth drive is set to $(-200^\circ, 560^\circ)$ and $(-225^\circ, 595^\circ)$.
- The soft and hard limit on the elevation drive is set to $(18^\circ, 90.5^\circ)$ and $(16.5^\circ, 92^\circ)$.

- The soft and hard limit on the boresight drive is set to $(-45.5°, 45.5°)$ and $(-47.5°, 47.5°)$.
- The *Position* flag allows the operator to switch between the *Main* and *Ref* position, corresponding to *Req[0]* and *Req[1]* respectively.

```
> set Sky -AzReq[0] 90 -AzReq[1] 180 -ElReq[0] 35 -ElReq[1] 55 -BorReq[0] 0
..-BorReq[90] -Position Main
  set Sky -AzReq[0] 90 -AzReq[1] 180 -ElReq[0] 35 -ElReq[1] 55 -BorReq[0] 0
..-BorReq[90] -Position Main
```

A script that repeatedly switches between the main and reference position could easily be submitted using the position switch. See section 9.8 for details on scripting.

### 9.6.6 The Source Object

The Source object allows the operator to point the telescope to a particular star, planet, or other target. It is also used to specify the source for various scans. There are some planets built into the software. For example, we can set the source to point at Mars, simply by setting the *Planet* keyword to the corresponding planet. If the operator wants to point the telescope in this manner he has to make sure the coordinate system, *CoordSys* is set to *RA_DEC*, otherwise the telescope will not move. On the other hand if the operator wants to control the telescope in the azimuth and elevation coordinate system then the *CoordSys* should be set to *AZ_EL*.

```
Source  -Status DONE -Abort false -Errno 0 -Errmethod "null"
 -ErrorMsg "Ok" -Ra[0]  21:55:32.44 -Ra[1]  00:16:02.46 -Dec[0] -68:01:59.7
 -Dec[1]  01:09:44.2 -L[0] 323.2 -L[1] 246.6 -B[0] -41.5 -B[1] -23.31212883
 -Epoch 2000 -Velocity -6.8 -CoordSys AZ_EL -VelSys VBARY -Planet Mars
 -SourceName "Mars"
```

We can easily point to objects not in the built-in catalog. For example, we might want to set the source to *Tau A* to calibrate the pointing of CLASS, see part IV for details on this method. Since this source is not in the built-in catalog we set the *Planet* to *none* and indicate the proper coordinates.

```
set Source -Ra[0] 04:29:30 -Dec[0] 26:16:53 -Planet none
```

```
set Source -SourceName Tau_A -CoordSys RA_DEC
```

Now we could execute a five-point or drift scan with Tau A as the source.

### 9.6.7 Axis Objects

The Axis objects (Azimuth, Elevation and Boresight) store all relevant variables for the three pointing axes. Debug information includes servo voltage and current as well as commanded and actual position. The commanded position is that which the servo loops try to achieve. The actual position is exactly what the encoders read out. The parameters that an operator might wish to modify are the stow and service positions for each axes. The axis can also be individually turned on and off. When an axis is turned off the power to the corresponding drive is turned off. The azimuth drive is different than the elevation and boresight because its axis is biased. The master drive is responsible for pointing the telescope while the slave drive is responsible for taking up the slack in the gears. That way we can accurately point the telescope without worrying about gear backlash. This does not affect how it is commanded; however, it explains why the azimuth reports master and slave drive information.

```
Azimuth  -Status RUNNING -Abort false -Errno 0 -Errmethod "null" -ErrorMsg "Ok"
 -MaxAccel 1 -MaxVel 1 -TickTime 0.05 -Tick 0.875 -Tolerance 278 -BackOutVel 0.1
 -LimitForward 560 -LimitReverse -200 -StowPos 180 -ServicePos 180
 -TargetPosition 180.0 -TargetVelocity 0 -TargetAcceleration 0 -ScanVelocity 0.2
 -ScanAcceleration 0 -CommandVelocity 0 -CommandAcceleration -1 -Position 130.0
```

```
-Velocity 0 -Acceleration 0 -PositionError -50.0 -VelocityError 0
-AccelerationError -1 -BusVolts[0] 294 -BusVolts[1] 294.6617126 -Voltage[0] 0
-Voltage[1] 0 -Current[0] -0.05 -Current[1] -0.02 -FollowError[0] 0
-FollowError[1] 0 -MotorEncoder[0] 130.0 -MotorEncoder[1] -122.0 -RateFactor 6.5
-TolTicks 10 -AxisCommand Off -CommandStatus Ok -State Off -ServoStatus[0] 0x1
-ServoStatus[1] 0x1 -ErrorCode[0] 0 -ErrorCode[1] 0 -SoftLimit Ok -ElecLimit Ok
-MechLimit Ok -BrakeStatus Engaged -ControlMode Interpolated -EncoderStatus 0x0
```

The most common axis command is to turn the drives off or on. We refer to this as bringing an axis down or up, respectively. For that purpose there are built in shortcuts in the shell.

```
> azdown
  azdown
  set Azimuth -AxisCommand Off
> azup
  azup
  set Azimuth -AxisCommand On
> eldown
  eldown
  set Elevation -AxisCommand Off
> elup
  elup
  set Elevation -AxisCommand On
> boredown
```

```
  boredown

  set Boresight -AxisCommand Off

> boreup

  boreup

  set Boresight -AxisCommand On
```

### 9.6.8 Sync Box

The SyncBox object is responsible for controlling the MCE sync box as well as recording the data, as described in section 9.4.1. Recording begins when the *Record* flag is set to *On*. The maximum time for any given DirFile is set in seconds and stored under the *MaxRecord* keyword. The DirFile begins at when the record flag is set and ends when the maximum time is exceeded. This is not compatible with the general CLASS data structure. For compatibility with the CLASS data structure the dir file length is not a counter that increments at start of data collection, but rather at the full hour. For example a ten minute data session, started at $9:05$ will finish the first DirFile at $9:10$. Before this data is shipped off the site it is processed by a packaging script. The amount of data recorded can be set by limiting the number of DirFiles recorded, via *MaxDirFiles*. If free-running behavior is desired then the *MaxDirFiles* field should be set to zero and the data recording should be controlled via the *Record* boolean. The NFS-path, where the data should be recorded, is also specified alongside the NFS-host information. The *DirFile* field sets the format for the DirFiles names.

```
SyncBox  -Status Error -Abort false -Errno 0 -Errmethod "null" -ErrorMsg "Ok"
  -Record Off -Recording Idle -NewFile Current -FileState File Closed
  -MaxRecord 1200 -MaxDirFiles 0 -DirFile "2015-02-20-22-44-15_acu"
  -NFSHost "BurgerMeister" -NFSPath "/mnt/uranus/atlase/data"


set SyncBox -Record On -MaxRecord 20 -MaxDirFiles 0
```

### 9.6.9 Shut Down

To cleanly shut down the system the start up sequence should be reversed.

```
-> track_stop
-> update_stop
-> [CRTL]-x
```

The [CRTL]-x escape sequence will initiate a reboot of the VxWorks machine. Just like the start up sequence it is good practice to execute these commands only in the terminal, not in a telnet session or over TCP.

## 9.7 Scan Commanding

The built-in observing routines are *FivePoint*, *DriftScan*, *SkyDip*, *AzScan*, *DecScan*, and *ProfileScan*. The properties of these scans are stored in the shared memory. As described before, this memory can be read via the *get* and modified via the *set* command. In the following sections I will describe each scan, reference the *get* output, define each variable, and give a typical-use example.

### 9.7.1 General Notes

Most scans have the option to repeat the scan $n$ times. This is typically set by the *Num-Scan* parameter. If this parameter is present it can be set to zero to repeat the scan until the boolean stop-scan flag, *EndScan*, is set to *True*. All scans can be aborted (not rec-

ommended) by setting the boolean abort flag, *Abort* to *True*. Most scans also allow the operator to specify the turn-around behavior. This is set to either slow or fast. The slow mode attempts to avoid the jerk due to the discontinuity in acceleration of the fast mode. In the fast mode the telescope will decelerate at the maximum deceleration starting at $\alpha_f$ from the end of the scan, depending on the angular velocity, $v$ and angular acceleration $a$. The turn around time is given by $t_f$.

$$\alpha_f = \frac{1}{2}\frac{v^2}{a} \qquad \text{and} \qquad t_f = 2\frac{v}{a} \tag{74}$$

The slow mode avoids the discontinuity at turn-around by linearly ramping up the acceleration and deceleration to maximum. This is more gentle as it avoids the jerk when full acceleration is applied instantly. Of course the turn-around takes longer in this mode. The turnaround angle and time, $\alpha_s$ and $t_s$ are both longer.

$$\alpha_s = \frac{4}{3}\frac{v^2}{a} \qquad \text{and} \qquad t_s = 4\frac{v}{a} \tag{75}$$

Both modes are symmetric in how they apply deceleration and acceleration. The maximum acceleration and velocities are parameters of the Azimuth object, *MaxAccel* and *MaxVel*.

As described in section 9.6.5, the the starting position of the scan is set via the requested azimuth, *AzReq[0]* and requested elevation, *ElReq[0]* of the Sky object.

### 9.7.2 FivePoint Scan

A five-point scan is a traditional method of determining pointing. When pointed at a known source this scan will take data at the reference position, then move half a beam width to either side in azimuth and elevation. This results in a measurement of five points to which

the user could fit a gaussian to determine the pointing of the detector. This pattern is also repeated at a reference position near the calibration object.

```
FivePoint  -Status OK -Abort false -Errno 0 -Errmethod "null" -ErrorMsg "OK"
-PgmID 1 -ObsReset OK -TMain 10 -TRef 10 -HPBW 90 -NumRpt 1
```

- The half power beam width, *HPBW*, is set in arcminutes.
- Dwell time on each position, *TMain*, is set in seconds.
- Dwell time on the reference position, *TRef*, is also set in seconds.
- This scan is repeated *NumRpt* times.

```
> set FivePoint -TMain 5 -TRef 5 -HPBW 100 -NumRpt 5
  set FivePoint -TMain 5 -TRef 5 -HPBW 100 -NumRpt 5
> get FivePoint
  get FivePoint
> FivePoint  -Status OK -Abort false -Errno 0 -Errmethod "null" -ErrorMsg "OK"
    -PgmID 1 -ObsReset OK -TMain 5 -TRef 5 -HPBW 100 -NumRpt 5
> FivePoint
  FSM command(s):
  FivePoint
```

### 9.7.3 DriftScan Routine

During a drift-scan the telescope is positioned such that the target drifts through the line of sight while telescope is scanning back and forth in azimuth. Since the elevation is always constant the atmosphere contributions are constant. This scan can also be used to determine the pointing of the telescope. The *DriftScan* routine will position the telescope above or

below the target, depending on the current hour angle, by *ElRange*, given in *HPBW* units. The telescope will scan back and forth by $\pm$ *AzRange* at a velocity given by *Velocity*. The scan is over when the target has drifted one *ElRange* past the beam.

```
DriftScan  -HPBW 90 -ElRange 0.5 -AzRange 1 -Velocity 0.1 -ScanType Az
  -TurnMode Fast -EndScan false -Status OK -Abort false -Errno 0 -Errmethod
  "null" -ErrorMsg "OK" -PgmID 5 -ObsReset OK
```

- The half power beam width, *HPBW*, is set in arcminutes.
- The elevation range, *ElRange*, is set in multiples of *HPBW*.
- The azimuth range, *AzRange*, is set in multiples of *HPBW*.
- The scan velocity, *Velocity*, is set in $\mathrm{deg/sec}$.
- The turn-around-behavior, *TurnMode*, can be set to either *Fast* or *Slow*.

```
> set DrifScan -HPBW 90 -ElRange 0.5 -AzRange 0.5 -Velocity 0.15 -TurnMode Fast
  set DrifScan -HPBW 90 -ElRange 0.5 -AzRange 0.5 -Velocity 0.15 -TurnMode Fast
> DriftScan
  FSM command(s):
  DriftScan
```

### 9.7.4 SkyDip Routine

The optical depth of the atmosphere can be estimated by performing a Sky-Dip scan. This is only true for a given frequency, at constant azimuth. The details of this calculation are well documented [23]. This type of scan simply scans up and down in elevation. Specifically the *SkyDip* routine will start at reference elevation,*ElMid*, and scan up and down by a specified

range, $\pm$ *Range*, at a given scan speed, *Velocity*. As always if the number of scans is set to zero the scan will repeat until the *EndScan* boolean flag is set to true. Like other scans, this scan also allows you to specify the turn-around mode, either *Fast* or *Slow*.

```
SkyDip  -ElMid 45 -Range 25 -Velocity 0.5 -NumScan 2 -ScanType El -TurnMode Fast
  -EndScan false -Status OK -Abort false -Errno 0 -Errmethod "null" -ErrorMsg "OK"
  -PgmID 2 -ObsReset OK
```

- The reference elevation, *ElMid*, is set in degrees.
- The scan range, *Range*, is set in degrees. The resulting range is *ElMid* $\pm$ *Range*.
- The scan velocity, *Velocity*, is set in $\mathrm{deg/sec}$.

```
> set SkyDip -ElMid 45 -Range 25 -Velocity 0.15 -NumScan 5
  set SkyDip -ElMid 45 -Range 25 -Velocity 0.15 -NumScan 5
> SkyDip
  FSM command(s):
  SkyDip
```

### 9.7.5 AzScan Routine

The AzScan Routine executes CLASS's primary observing strategy as outlined in section 6.1.2. It scans back and forth in azimuth by $\pm$ the azimuth range, *Range*, at a constant velocity, *Velocity*. This scan will typically be called with *NumScan* set to zero. This will repeat the scan indefinitely without gaps between the scan periods. When the end-scan flag is set to true the last scan will finish executing and the telescope will move back into its commanded position.

```
AzScan  -Range 20 -Velocity 1 -NumScan 10 -ScanType Az -TurnMode Fast
  -EndScan false -Status OK -Abort false -Errno 0 -Errmethod "null"
  -ErrorMsg "OK" -PgmID 3 -ObsReset OK
```

- The azimuth velocity, *Velocity*, is set in $\mathrm{deg/sec}$.
- The azimuth range, *Range*, is set in $\mathrm{deg}$.
- The number of scans, *NumScan*, should be set to zero for repeating scans.

```
> set AzScan -Range 180 -Velocity 1 -NumScan 0
  set AzScan -Range 180 -Velocity 1 -NumScan 0
> AzScan
  FSM command(s):
  AzScan
```

### 9.7.6 DecScan Routine

The DecScan Routine is similar to the aforementioned AzScan Routine. Instead of scanning at a constant azimuthal velocity it attempts to scan at a constant square degree rate, $\mathrm{deg}^2/\mathrm{sec}$. This results in every sky pixel being integrated for an equal amount of time. To do that we have to compensate for the distortion of the coordinate grid on the sky, see section 10.3 and 6.1.2 for more information.

$$DecRate = \cos(\mathrm{dec}) * \frac{d\,\mathrm{dec}}{dt} \tag{76}$$

```
DecScan  -DecRate 0.5 -MaxVel 2 -Range 360 -NumScan 0 -ScanType Dec
  -TurnMode Fast -EndScan false -Status OK -Abort false -Errno 0
  -Errmethod "null" -ErrorMsg "OK" -PgmID 4 -ObsReset OK
```

- The rate in wich the declination is scanned, *DecRate*, is set in $\mathrm{deg/sec}$.

- The maximum azimuth velocity, *MaxVel*, is set in $\mathrm{deg/sec}$.
- The azimuth range, *Range*, is set in $\mathrm{deg}$.
- The number of scans, *NumScan*, should be set to zero for repeating scans.

```
> set DecScan -DecRate .5 -MaxVel 2 -Range 180  -NumScan 0
  set DecScan -DecRate .5 -MaxVel 2 -Range 180  -NumScan 0
> DecScan
  FSM command(s):
  DecScan
```

### 9.7.7 ProfileScan Routine

As a final scanning option the FSM can read a scan profile from file and execute the path. The program reads the profile from *VxHost*. Each line of the profile text-file is an azimuth-elevation pair. There is one second time interval between each line. The FSM will interpolate a smooth path between the points given in the profile. Given that neither the maximum acceleration or velocity are exceeded the scan will trace out the profile supplied, otherwise it will limit the velocity and acceleration to the preset software limits. If *NumScan* is set to zero the scan will repeat until the boolean *EndScan* is set to true.

```
vxdev@vxhost1:~/input$ less Profile1.txt
0.000  45.000
0.083  45.017
Profile1.txt
```

```
ProfileScan  -Status OK -Abort false -Errno 0 -Errmethod "null" -ErrorMsg "OK"
  -PgmID 6 -ObsReset OK -NumScan 0 -EndScan false -FileName "Profile1"
```

- The profile is loaded from a text file, *FileName*, which is located in */home/vxdev/input/*.
- The number of scans, *NumScan*, can be set to zero to repeat the scan until *EndScan* is set to *True*.

```
> set ProfileScan -FileName Profile1 -NumScan 0
  set ProfileScan -FileName Profile1 -NumScan 0
> ProfileScan
  FSM command(s):
  ProfileScan
```

## 9.8 Mount Control Scripting Language

Atlas has a custom script interpreter exposed via a TCP server. The server listens on port 2023 and accepts one null terminated string. The string can include an arbitrary number of lines, terminated by the newline character. Each line represents a separate command and the script interpreter accepts the full range of shell commands, e.g., set and get. The set and get commands can, alternatively, be semicolon delimitered as shown below.

```
set Source -CoordSys AZ_EL; Sky -Position Main
```

The behavior of a semicolon delimitered line is equivalent to two separate set or get commands.

```
set Source -CoordSys AZ_EL
set Sky -Position Main
```

The *get* command will return semicolon or newline delimetered data depending on how it was called.

### 9.8.1 Submitting Scripts

To submit a script we have to first open a script block, via *beginScript*. The block is intuitively closed with the *endScript* keyword. The set and get commands are not supported within a script. Every command must be an executable command. It is important to recall that those objects that do not execute a particular control sequence have exec-functions that simply set the desired fields and return null.

```
beginScript
Command 1
Command 2
.
.
.
Command n
endScript
```

### 9.8.2 Precise Timing of Execution Function

The scripting language adds support for the timing of commands. That is, a command can be executed at a particular time. Since Atlas runs a real-time-operating-system tied to a GPS clock, this timing of commands can be very precise.

- -at_start_utc [+]hh:mm:ss
- -at_end_utc [+]hh:mm:ss

The *at_start_utc* command starts the script at the given hour, minute and second. This command acts as a condition. That is, it will block until the time is equal to or greater then the at-command. If the script is submitted after the time indicated in the at-command it will simply execute the script without throwing an error. All *at_end* prerogatives are optional.

The time that the script is submitted is referred to as the reference time. The optional + argument will cause execution at a time equal to the reference time plus the given hours, minutes and seconds. Since multiple *at* blocks can be submitted in a single script, the optional + argument will use the start time of the previous *at_start_utc* prerogatives, if available.

```
At -at\_start\_utc hh:mm:ss
Command
endAt
```

The *at block* takes several optional arguments specifying the start day, month, and year. It can also accept arguments that will abort the command at a given time, day, month and year. If the commands execute before an *at_end* primitive, then the at command will be blocking until such a time indicated by the *at_end*.

- -at_start_day dd
- -at_start_month mm
- -at_start_year yy
- -at_end_utc hh:mm:ss
- -at_end_day dd
- -at_end_month mm
- -at_end_year yy

The optional day, month, and year arguments default to the current date. This is important as an *at* prerogative for `06:00 UTC` submitted at `07:00 UTC` will not block until `06:00 UTC` the following day, it will execute immediately.

### 9.8.3 Loops within a Script

Within a script a loop can easily be set up with the *Loop* block.

```
Loop -loop\_repeat N
Commands
endLoop
```

Optionally a loop name can also be supplied. The loops should always be named as this will make debug via the status messages easier. The operator will be able to distinguish between inner and outer loops, for example.

```
Loop -loop\_name Outie -loop\_repeat N
Commands
Loop -loop\_name Innie -loop\_repeat M
Commands
endLoop
endLoop
```

If necessary a pause, measured in seconds, can be inserted in the program via the sleep command, *Sleep -sec sss*.

### 9.8.4 Closing Thoughts

Only one script can run at a time. If another script is submitted before the previous script has finished the server will respond with "FSM busy, please try later." To check if a script is running the server can be queried with *scriptStatus*. This will return the script status as detailed below.

```
scriptStatus
FSM -AtStartJD 0.000000 -AtEndJD 0.000000 -LoopName "loop" -LoopIndex 5
  -LoopRepeats 5 -Line 13 -ErrorCount 0 -FSMBusy false -Abort false
  -AbortScript false -AbortAt false -InAt false -NewCmd false -LineOK true
  -Override false -CurrentCmd "Boresight" -CmdLine "Boresight"  -ErrorMsg "null"
```

- The *AtStartJD* and *AtEndJD* indicate the time, converted to a julian date, that the at block is indicated to begin and end. These fields are nonzero after the *At* prerogatives is encountered and before the *endAt* prerogatives is encountered.
- The *LoopName* field indicates the name, if set, of the loop currently being processed.
- The *LoopIndex* field indicates the current index of the loop corresponding to *LoopName*. Note that both *LoopName* and *LoopIndex* are for the inner most loop currently being executed.
- The *LoopRepeats* field indicates the number the loop will repeat for.
- The *Line* field indicates the line of the script, currently being executed.
- The *FSMBusy* boolean flag is true whenever a script is running.
- The *Abort* flag is set to true if the script was aborted.
- The *AbortAt* field reports the time the script was aborted, if *Abort* is true.
- The *InAt* is true if an at-block is currently active.
- The *CurrentCmd* indicates the currently executed object.

Of course any script can be aborted by sending the *scriptAbort* command. This will result in the currently running exec-function to be aborted and the script terminated. When a script is successfully submitted the server will respond with the task ID of the running script. The script always spawns as "TMCJob". This TCP server could easily be leveraged to implement a simple web interface or local graphical user interface that can send commands and periodically display key values by sending the get commands once a second.

# Part IV

# CLASS Simulation

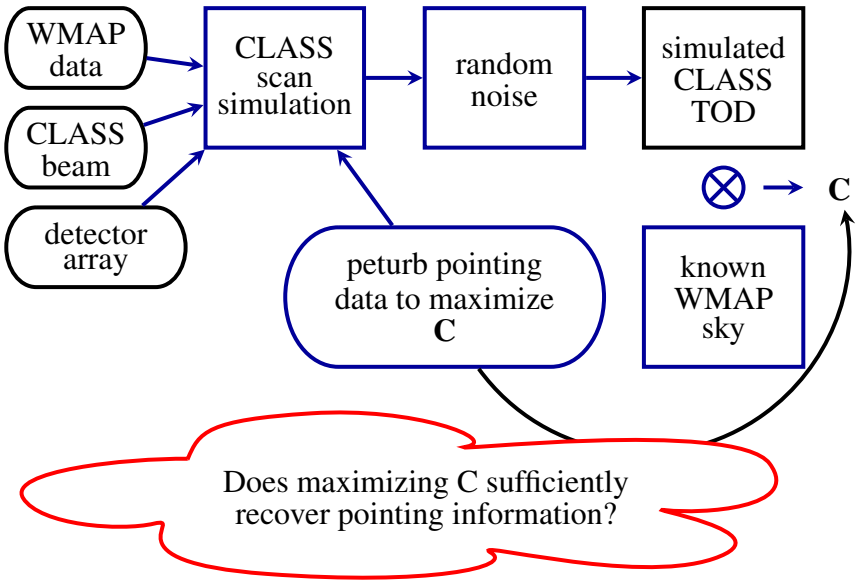


Figure 56: Overview of the CLASS simulation that will answer to what degree CLASS can calibrate pointing from known sources directly in the time-domain. The software determines pointing by comparing the CLASS data against a simulated data drawn from WMAP data and a pointing model. The two time-streams are compared and reduced to a single number, $C$ corresponding to the likelihood that the model is true.

This simulation is inspired by the need of CLASS, as any observatory, to calibrate its pointing. A polarized experiment, like CLASS, has the additional requirement of constraining the polarization angle. To detect $B$-modes on the level of $r = 0.01$ requires the polarization angle to be calibrated to better then $0.9^\circ$ [5]. The simulation is designed to test Tau A as a calibration source both for pointing and polarization angle. To this end the simulation creates an $X$, $Y$ time stream as corresponding to the two linear detector polar-

izations of CLASS. The time ordered data is assumed to be de-modulated, as a simulation of the VPM is outside of the scope of this exercise. I will refer to the simulated CLASS data as the fiducial data set. The fiducial data set is then compared to a series of models with varying detector offsets. These models do not include any noise. The software is designed to identify the model which maximizes the likelihood that the fiducial data set is equivalent to the model plus guassian noise. A Monte Carlo method will be used to determine to what degree this technique can determine the pointing offsets and then separately for the polarization offsets only. Once real CLASS data is generated the software will be able to determine the pointing of CLASS on a detector by detector basis according to the limits prescribed by the Monte Carlo simulations.

# 10 Software Overview

The simulation begins with three major components, the WMAP sky, the CLASS beam, and the CLASS detector array. The WMAP sky is taken from the nine-year release and is packaged in heal-pix maps. The optical parameters [26] of the CLASS telescope can be combined with the individual detector's offset from the center of the detector array to provide a reasonable initial condition for each of the detectors pointing information. With this information we can now simulate a particular physical (az, el) scan of the telescope. Given this scan we simulate the sampling of the sky by the TES pairs. The resulting time ordered data can be compared with that of the physical experiment and the pointing parameters can

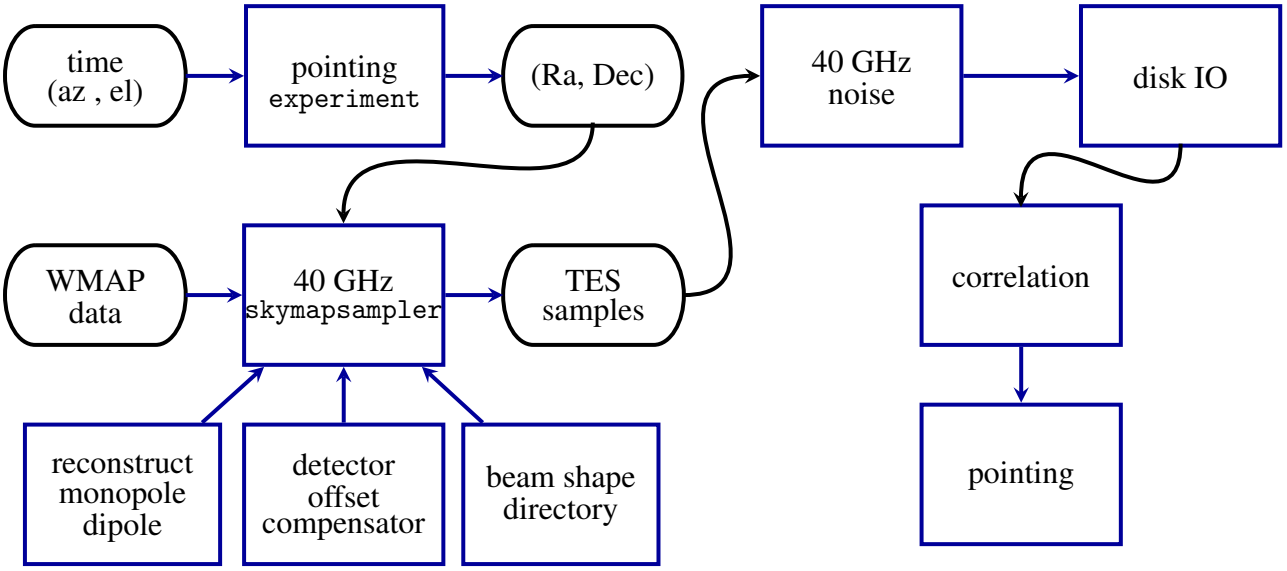


Figure 57: Overview of the CLASS simulation that seeks to answer the question of pointing calibration: can the instrument's pointing be recovered from the known WMAP sky.

now be tweaked to maximize the correlation. In this manner we can recover the actual physical pointing of the CLASS telescope on a detector by detector basis. This corrected pointing will short-circuit the effects of physical optics and even those of uncalibrated information of the mount.

## 10.1 Beam Shape

The beam-shape is approximated as a gaussian beam with $1.5^\circ$ FWHM for $40$ GHz [26]. In the simulation this is easily accomplished by smoothing the WMAP sky with a gaussian beam of identical FWHM. This is easily accomplished using the healpix smoothing

function.

```
smoothed_sky = healpy.smoothing( wmap_sky, math.radians( FWHM ) )
```

Sampling a single pixel of the `smoothed_sky` is the equivalent of sampling the `wmap_sky` with a gaussian beam. While the beam is only approximated by a gaussian, this approximation does not impact the validity of the simulation. No matter what the beam shape is, recovery of pointing information is independent as long as the data are adjusted for the beam-shape.

## 10.2 Focal Plane Offset

Only a detector in the center of the focal path would point in the direction of the telescope. Any other detector, will have a point error, or offset. This pointing-offset can be calculated knowing the effective focal length, $f_{eff}$, and the distance, $d$, the detector is offset from the center. The angular-offset is characterized by the angle $\beta$

$$\tan\beta = \frac{d}{f_{eff}} \,. \tag{77}$$

This calculation is often done by using the $\tan\beta \approx \beta$ approximation. In the CLASS case this results in an up to $9$ arcsec error. Since this is a calculation done once, and the result stored, this calculation should not be approximated.

Similarly, the same calculation can be done on the $y-plane$, resulting in a $\beta_y$ offset, for example. $\beta_x$ and $\beta_y$ could then be used to correct pointed. Alternatively the focal plane can be parameterized in the polar coordinate system. Every detector is parameterized by two

variables, an angle $\alpha$ and a distance $d$. Where a detector who's offset vector is along the $\hat{x}$ vector, is considered to have $\alpha = 0$. This parameterization makes pointing corrections more trivial. As we can now imagine a spherical coordinate system where all longitudinal lines meet at the location indicated by the pointing of the telescope. The angular corrections are now, always, movements along a great circle. The importance of this is explained in section 10.3.

## 10.3 Focal Plane Distortion

Intuitively, we would translate the $\mathrm{x} - \mathrm{offset}$ and $\mathrm{y} - \mathrm{offset}$ into an angle $\theta_x$ and $\theta_y$, which we would then add to the $az$ and $el$ to result in the corrected pointing. This type of angle addition only works if the pointing directions are moving along a great circle. Azimuthal offsets are smaller at higher elevations. This type of distortion is depicted in figure 58.

To properly perturb the pointing the rotation offsets are implemented using quaternion rotations. The axis angle quaternion is defined by the fiducial pointing vector. It is then rotated twice. First a quaternion is created that represents the $\beta$ offset. This quaternion is then rotated by the $\alpha$ quaternion before it is applied to the pointing quaternion. Finally the corrected pointing quaternion is converted back to $az$, $el$ coordinates. This pointing correction is implemented in `pointing.py` and supported by `quaternion_utils.py`.

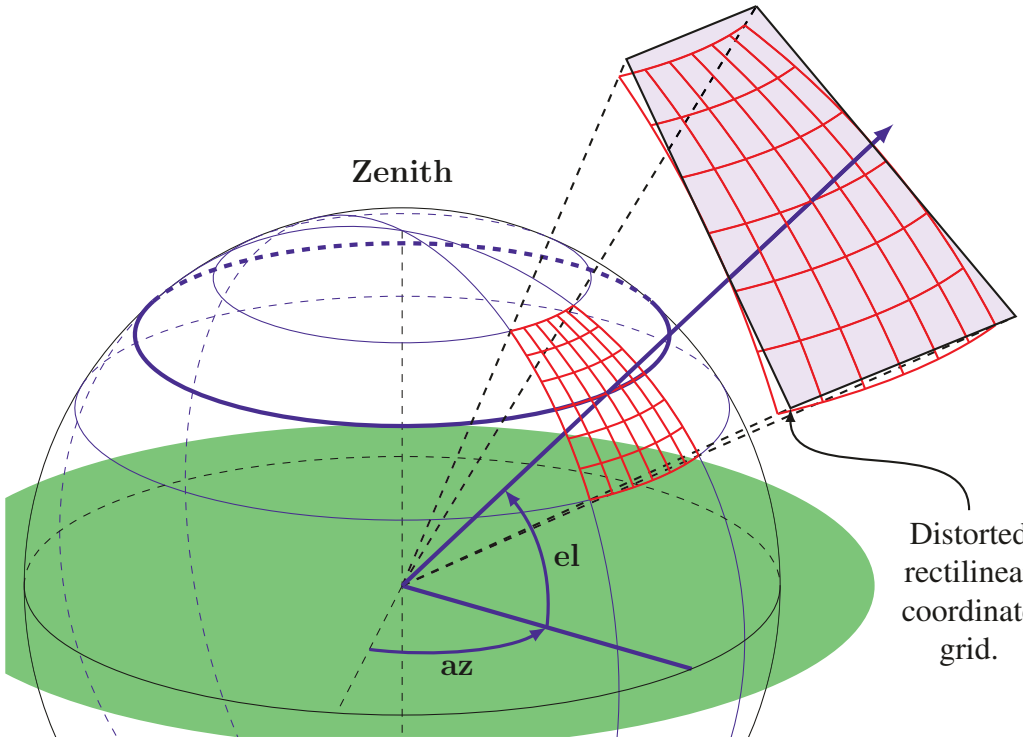


Figure 58: The angular corrections depend on the elevation of the detector. This is due to the fact that off-sets in the $x - axis$ are not angular-offsets on a great circle. The $y$ offsets, however, are angular offsets on a great circle and therefore are not distorted. We further notice that this distortion disappears at the zenith. At the zenith, a movement in an arbitrary direction is always a movement along a great-circle. We can exploit this fact by wisely choosing our coordinate system.

## 10.4 Creating Time Ordered Data

Each CLASS detector is a pair of perpendicularly polarized TES detectors. These detectors are sensitive to unpolarized light and linearly polarized light, parallel to the principle axis of the detector. Expressed using Stokes polarization parameters the $X$ and $Y$ detectors

sample the intensity $I$ and the $Q$ stokes parameter as follows:

$$X = \frac{1}{2}\left(I + Q_{\rm det}\right) \tag{78}$$

$$Y = \frac{1}{2}\left(I - Q_{\rm det}\right) \ , \tag{79}$$

where $Q_{\rm det}$ is defined with respect to the detector orientation.

### 10.4.1 Sky Coordinates

The local parameterization system, $Q_{det}$ has to be related to $Q$ and $U$ parameters defined with respect to the galactic coordinate system, as they are found in WMAP data products. By rotating the detectors $45^\circ$ they could either measure $Q_{\rm sky}$ or $U_{\rm sky}$. The angle of rotation between the galactic coordinate system and the local one is given by the parallactic angle, $\delta$. Of course the rotation of the boresight changes the detectors reference angle, and thus the important quantity is the sum of the parallactic angle and the boresight angle, or $\delta + \gamma$. We can then compute the $X$ and $Y$ value given we know the $I_{\rm sky}$, $Q_{\rm sky}$, and $U_{\rm sky}$ values, as follows:

$$X = \frac{1}{2}\left(I + Q\cos(\delta+\gamma) + U\cos(\delta+\gamma)\right) \tag{80}$$

$$Y = \frac{1}{2}\left(I - Q\cos(\delta+\gamma) - U\cos(\delta+\gamma)\right) \ . \tag{81}$$

### 10.4.2 Detector Noise

The effective $Q$ equivalent temperature noise is $207\ \mu{\rm K} * \sqrt{s}$ per detector. At $200\ {\rm sps}$ this is equivalent to $2.927\ {\rm mK}$ rms noise per sample. This is implemented by added a random

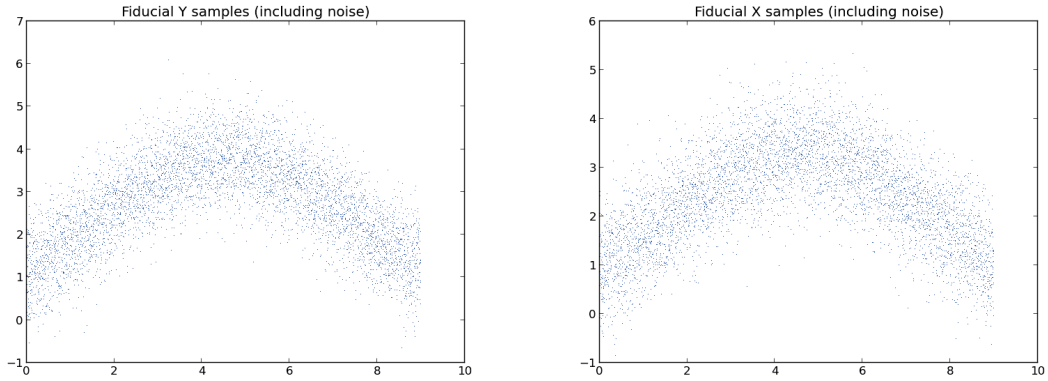


Figure 59: A sample of $X$ and $Y$ time ordered data streams produced by allowing Tau A to drift through the field of view of a single detector. The horizontal axis plots temperature in $\mathrm{mK}$ and the vertical axis plots time in minutes.

variable $N$, whose distribution is given by a gaussian statistic centered around $0\ \mathrm{mK}$ with $2.927\ \mathrm{mK}$ standard deviation. An example of a detector pair time stream is shown in figure 59.

# 11 Analysis

Once the time ordered data is created the pointing matrix needs to be perturbed to maximize the correlation to the actual data set. In order to do this we have to define exactly how we compare two data sets. Eventually we want to be able to predict, with confidence, the likelihood that two data sets were generated by the same underlying parameters. Let's define the set of measured time-ordered values as $\mathbb{M}$ and the set of simulated values as $\mathbb{D}$. We will use the constant $C_{\alpha\beta\gamma}$ to represent the likelihood that $\mathbb{M}$ and $\mathbb{D}$ were produced by

the same underlying parameters, $\alpha$, $\beta$, and $\gamma$. A search function that maximizes $C$ will, in this context, find the pointing information most likely to be true.

## 11.1 Mathematical Foundation

Given $N$ terms of an independent sequence, $\{X_N\}$ of normal random variables having mean $y(x_i)$ and variance of $\sigma_i^2$, the likelihood function is as follows:

$$L(a_1, a_2, \ldots, a_p) = \left[\prod_i^N \left(\frac{1}{\sqrt{2\pi\sigma_i^2}}\right)\right] \exp\left(-\frac{1}{2}\sum_i^N \frac{(y_i - y(x_i))^2}{\sigma_i^2}\right) . \tag{82}$$

The model parameters are represented by $a_1, a_2, \ldots, a_p$. To maximize the likelihood is to minimize $\chi^2$, where $\chi^2$ is defined as follows.

$$\chi^2(a_1, a_2, \ldots, a_p) = \sum_i^N \frac{(y_i - y(x_i))^2}{\sigma_i^2} \tag{83}$$

### 11.1.1 Practical Considerations

So long as the signal does not change appreciably on time scales faster then the sampling rate, a reduced sampling rate is equivalent to a time integrated faster sampling rate. In a drift scan, for example, the time scales will be on the order of $3\,\mathrm{min}$. This allows the simulation to run at drastically reduced sampling rates, $1\,\mathrm{sps}$ vs. $200\,\mathrm{sps}$. To make $\chi^2$ quantities more robust against changing sample rates we consider the reduced $\chi^2$ formula:

$$\chi^2_{\mathrm{red}}(a_1, a_2, \ldots, a_p) = \frac{1}{N}\sum_i^N \frac{(y_i - y(x_i))^2}{\sigma_i^2}. \tag{84}$$

The standard deviation is given by the detector noise and depends on the sample rate. The number of points, $N$ can be expressed in terms of simulation time, $T$ and sample rate, $r$:

$$N = \frac{T}{r} \quad \text{and} \quad \sigma^2 = \frac{(207\ \mu\text{K})^2}{r}. \tag{85}$$

We now consider the reduced $\chi^2$ quantity for the fiducial model. That is $y_i - y(x_i)$ is simply noise.

$$\chi^2_{\text{red}}(a_1, a_2, \ldots, a_p) = \frac{1}{N}\sum_i^N \left(\mathcal{N}(0,1)\right)^2 = \chi^2(N)/N. \tag{86}$$

We thus calculate the expected value of the $\chi^2_{\text{red}}$ as unity, with a standard deviation of $\sqrt{2/N}$. We find that the expected value is independent of the sample rate, while the variance of the $\chi^2$ decreases with an increased sample rate. It is important to note that a decreased variance in the $\chi^2$ value does not increase the ability to distinguish different models. The ability to distinguish different models depends only on the noise and simulation time.

## 11.2 $\chi^2$ Problems

In the previous section I assumed that the degrees of freedom, $\nu$ are approximately equal to the number of samples, $N$. The definition in equation 84 is only true if $\nu = N$. The $\chi^2_{\text{red}}$ as a random variable distributed according to a $\chi^2$ distribution is a problematic proposal. If we assume that the model under test is the true model and $N$ is sufficiently large so that $N \approx \nu$ then the $\chi^2$ test could reject the model if and only if the calculated $\chi^2_{\text{red}}$ is more then two or three, depending on the confidence required, away from $1$. Any deviation smaller and the $\chi^2$ test can not make a significant statement of the models correctness. This is

further complicated by the fact that we can not easily calculate the degrees of freedom if the model under test is not the true model. For further discussion see [3].

Instead the $\chi^2_{\rm red}$ present in section 11.1 is only used to minimize the average residual, expressed in units of noise, and normalized against the number of samples:

$$\frac{1}{N\sigma}\sum(y_i - y(x_i))^2. \tag{87}$$

The errors on this method will be estimated via a Monte Carlo simulation.

# 12 Results

The Crab Nebula at coordinates $\alpha = 5^{\rm h}34^{\rm m}32^{\rm s}$ and $\delta = 22°0'52''$, J2000 represents the brightest polarized point source in the sky [5]. The brightness and well known location of Tau A, within the Crab Nebula, make Tau A an excellent candidate to test simulations and to calibrate the pointing. Figure 60 shows the $Q$ and $U$ polarization maps of Tau A reconstructed from the $40$ GHz WMAP data and smoothed to a $1.5°$ FWHM beam. This is the signal as CLASS would see it.

## 12.1 Recovering Tau A

CLASS is not designed to be sensitive to temperature anisotropy as those measurements will not be controlled by the VPM. This effect can be thought of as gain drift, $\Delta g$ in the intensity of the detectors, as follows:

$$X = .5\left((1+\Delta g)I + Q\cos pa + U\sin pa\right) \tag{88}$$

and

$$Y = .5\left((1+\Delta g)I - Q\cos pa - U\sin pa\right)\ , \tag{89}$$

where $pa$ is the parallactic angle. Since this drift is not present in the difference of the two detectors $X - Y$,

$$X - Y = Q\cos pa + U\sin pa\ , \tag{90}$$

we rely on the difference of the detector pair to reconstruct the polarization signal and do not worry about drifts in the overall temperature.

### 12.1.1 Dip Scan

As is evident in figure 60 the maximum signal to noise ratio is achieved when the detectors are lined up with the $Q$ polarization axis. One is tempted to simply let this source drift through the field of view while scanning back and forth. Such a scan lasts roughly $12\ \mathrm{min}$. The simulated scan was started `2015/05/01 19:00:00` and lasted exactly $12\ \mathrm{min}$. At $200\ \mathrm{sps}$ the scan produced $144000\ \mathrm{samples}$ with an rms noise of $2.927\ \mathrm{mK}$ each sample. The azimuth was fixed at $7.54^\circ$ while the elevation axis scanned at $1.5^\circ/\mathrm{s}$. As seen in figure 61 this level of noise does not allow for reconstruction of Tau A. This scan is implemented in `makescan.py`.

### 12.1.2 A 24 Hour Lissajous Scan

Due to the weak polarized signal the simulation is tested with a $24$ hour scan tracking Tau A. In practice this scan would have to be broken up over several days as Tau A would

set. While the telescope is tracking Tau A the pointing is disturbed according to a never repeating Lissajous pattern defined as follows:

$$x = A_x sin(\omega_x t), \tag{91}$$

$$y = A_y sin(\omega_y t), \tag{92}$$

where $x$ and $y$ corrospond to the offset in the azimuth and elevation, $A_x$ and $A_y$ are the maximum offsets respectivly.

The simulated scan was started `2015/05/01 19:00:00` and lasted exactly $24$ hours. At $200\ \mathrm{sps}$ the scan produced $17.28\ \mathrm{mega\ samples}$ with an rms noise of $2.927\ \mathrm{mK}$ each sample. The azimuth and elevation tracked Tau A with an additional Lissajous offset defined by an offset magnitude of $2^\circ$ in both azimuth and elevation, with a period $32\,\mathrm{sec}$ for the elevation component and $\sqrt{2}32\,\mathrm{sec}$ for the azimuth, guaranteeing a non repeating pattern. The result of this scan are shown in figure 62. This scan is implemented in `makescan_lissajous.py`.

### 12.1.3 Drift Scan

Time ordered data is best demonstrated with a simple drift scan, in which Tau A drifts through the field of view of a single detector. This is also the scan which will be used in the later analysis as it maximizes signal to noise. The simulated scan was started `2015/05/01 19:00:00` and lasted exactly $9$ minutes. So that the noise is visually less overwhelming the scan was integrated down to $10\ \mathrm{sps}$ with an rms noise of $654.5\ \mu\mathrm{K}$ each sample. The azimuth and elevation were fixed at $44.7^\circ$ and $20.0^\circ$ respectively. The hitmap

as well as the Q time stream are shown in figure 63. A gaussian function was fitted to the time stream of the form:

$$T = ae^{-\frac{(x-\mu)^2}{2\sigma^2}}. \tag{93}$$

The fit paramaters corosponding to the fit in 63 are as follows:

$$(a, \mu, \sigma) = (-0.4585, 4.1357, 3.2113), \tag{94}$$

indicating a minimum observered temperature of $-459$ $\mu$K a deviation of only $19$ $\mu$K from WMAP data. This scan is implemented in `makescan_drift.py`.

## 12.2 Monte Carlo Error Estimation

Without prior knowledge the most reasonable assumption is that of gaussianity. So I will assume that the error on any one variable, $\alpha$, $\beta$, or $\gamma$ follows a gaussian distribution. A gaussian distribution will be fit to the results of the Monte Carlo simulations to estimate the variance.

### 12.2.1 Monte Carlo $\alpha$

In this simulation the $\beta$ offset is fixed at $2'$ and $\gamma$ offset is fixed at zero, while the $\alpha$ offsets are allowed to vary between $\pm 180^\circ$. The $\alpha$ which minimizes the residual is recorded. The simulation is then repeated with a new fiducial data set, assuring a new random outcome. The results are plotted in figure 64. With a standard deviation of $8.814^\circ$, this method could possibly be useful to constrain pointing to roughly within $\pm 29^\circ$ with $99.7\%$ confi-

dence, given $\beta$ and $\gamma$ are fixed. There is no significant mean offset, indicating an unbiased estimator.

### 12.2.2 Monte Carlo $\beta$

In this simulation the $\alpha$ and $\gamma$ offsets are fixed at zero, while the $\beta$ offsets are allowed to vary between $\pm 20'$. The $\beta$ which minimizes the residual is recorded. The simulation is then repeated with a new fiducial data set, assuring a new random outcome. The results are plotted in figure 65. With a standard deviation of $7.9'$, this method could possibly be useful to constrain pointing to roughly within $\pm 24'$ with $99.7\%$ confidence, given $\alpha$ and $\gamma$ are fixed. A mean offset of $-2.924'$ is troubling as this is significant compared to the standard deviation and indicates that the estimator is biased or just not accurate.

### 12.2.3 Monte Carlo $\gamma$

In this simulation the $\alpha$ and $\beta$ offsets are fixed at zero, while the $\gamma$ offsets are allowed to vary between $\pm 20^\circ$. The $\beta$ which minimizes the residual is recorded. The simulation is then repeated with a new fiducial data set, assuring a new random outcome. The results are plotted in figure 66. With a standard deviation of $5.326^\circ$, this method could possibly be useful to constrain pointing to roughly within $\pm 15^\circ$ with $99.7\%$ confidence, given $\alpha$ and $\beta$ are fixed. A mean offset of $-2.725^\circ$ is troubling as this is significant compared to the standard deviation and indicates that the estimator is biased or just not accurate.

### 12.2.4 Observing Time

The Monte Carlo simulations ran for $9\ \mathrm{min}$, the time it takes Tau A to drift by $1.5^{\circ}$. The ability to constrain pointing is a function of the signal to noise ratio. Since there is no brighter object in the sky the only way to increase the signal to noise ratio is increase the observing time. The telescope could track Tau A so that it takes $900\ \mathrm{min}$ for Tau A to drift through the field of view of the detector. This would increase the signal to noise ratio ten-fold. Since such a large scan is computationally prohibitive using the Monte Carlo simulation I simulate an increased observing time by reducing the noise by a factor of ten.

In practice Tau A only stays within observable elevations roughly $7.4\ \mathrm{hours}$ every day, or roughly $450\ \mathrm{min}$. To achieve a factor of ten improvement in signal to noise would require dedicating two days. To achieve a factor of one hundred improvement would require more then half a year of dedicated observation of Tau A. The results of these reduced noise simulations are shown in figures 67, 68, and 69. The error on $\alpha$ reduced almost ten fold, the error on $\beta$ reduced about four fold, and the error on $\gamma$ reduced by about a third. These results are summarized in table 12. Even if Tau A is observed for two continuous days, the $\gamma$ angle alone can not be recovered with high enough precision to allow detection of B-modes on the level of $r = 0.01$.

In closing, we note the skewness of both the $\beta$ and $\gamma$ results, both showing a strong deviation from a normal distribution as well as a tendency to fall negative of zero. The $\beta$ bias can be explained by the fact that the scan hits just above the center of Tau A, thus a bias towards higher signal to noise models would result in a bias towards negative $\beta$ offsets. The

| Time: | 9 min | | 2 days | |
|---|---|---|---|---|
| | $\mu$ | $\sigma$ | $\mu$ | $\sigma$ |
| $\alpha$ | $-0.264^\circ$ | $8.814^\circ$ | $+0.002^\circ$ | $0.986^\circ$ |
| $\beta$ | $-2.924'$ | $7.900'$ | $-0.556'$ | $2.201'$ |
| $\gamma$ | $-2.752^\circ$ | $5.326^\circ$ | $-1.994^\circ$ | $2.203^\circ$ |

Table 12: Summary of Monte Carlo results of drift scans integrated over nine minutes and two days.

$\gamma$ one-sidedness can be explained by noting that the scan was designed to maximize $Q$, that is a rotation of $\pm\gamma$ has the same effect on the magnitude of $Q$, hence it is indistinguishable in the model.

## 12.3 Optimizing the Scan strategy

As we have seen a simple drift scan is not optimal for probing pointing. The pointing error can be reduced simply by nodding the elevation axis. Specifically the scan strategy proposed for calibrating off the Tau A signal has the azimuth axis fixed, while the elevation axis moves $\pm.75^\circ$ and the boresight moves $+45^\circ$ and back. The speed of the elevation dip and the boresight rotation is timed so that it completes three full periods in the time it takes Tau A to drift by. See figure 70 for scan parameters. This scan is implemented in `monticarlo_utils.py`. This is a practical scan strategy as the same scan allows for calibration of all three variables, $\alpha$, $\beta$ and $\gamma$. The improved pointing accuracy is evident in

figures 71,72,73. No significant errors are found in either the $\alpha$, $\beta$ or $\gamma$ simulation.

### 12.3.1 Extended scan

As done before, the errors on the parameters are significantly reduced by increasing the scan time to $900\ \mathrm{min}$, the equivalent of observing Tau A for $7.5\ \mathrm{hours}$ on two days. With the extended optimized scan the pointing can be located with a standard error of roughly $21''$, with an ambiguity remaining in the polar angle $\alpha$ with a standard error of roughly $40'$. If the pointing is already known this optimized scan can determine the polarization angle to within $\pm 0.67^\circ$ with $99.7\%$ confidence, a level sufficient for recovery of B-Modes to the level of $r = 0.01$.

## 12.4 Conclusion

The optimized extended scan is able to constrain the polarization angle with an error less then $0.67^\circ$ with $99.7\%$ confidence a level sufficient for CLASS's detection of B-Modes on the order of $r = 01$.

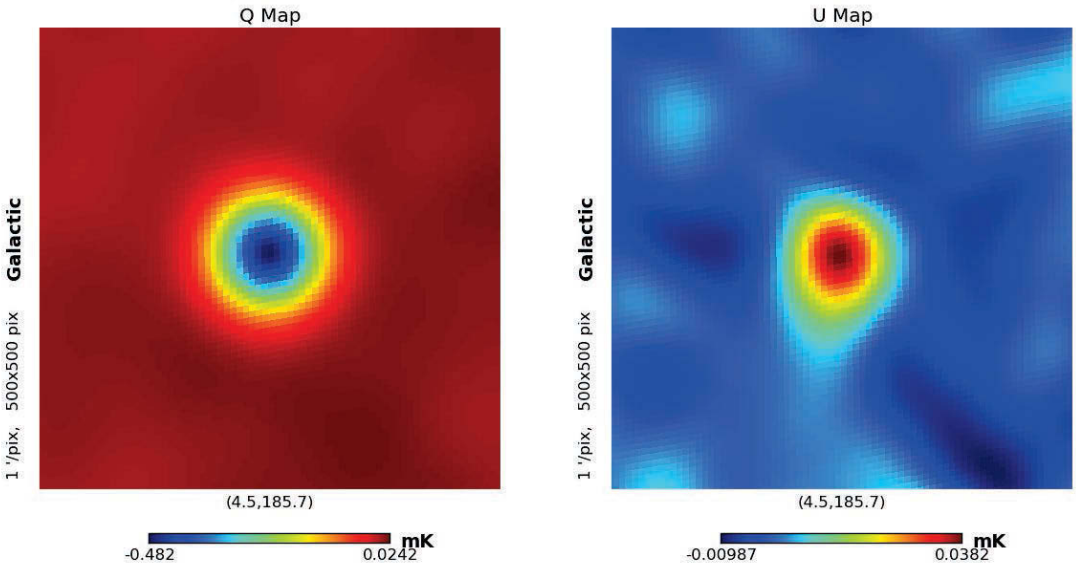


Figure 60: Q and U maps of Tau A, smoothed to a gaussian $1.5^\circ$ beam and observed in the $40$ GHz band. The maps were produced using WMAP data.

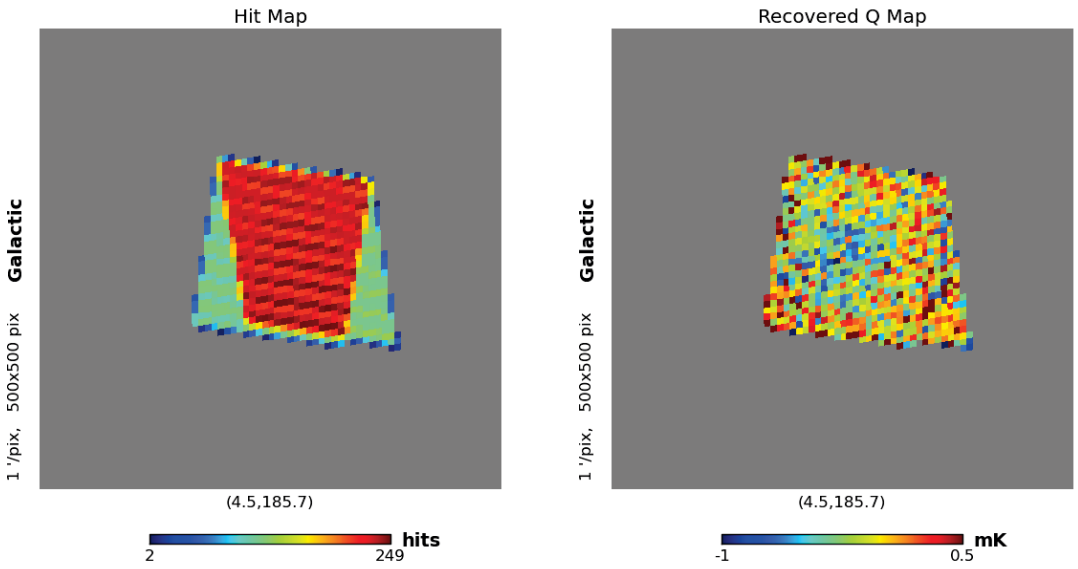


Figure 61: A hit map showing the number of times a pixel was sampled, and a reconstructed Q polarization map. This is the result of the dip scan.

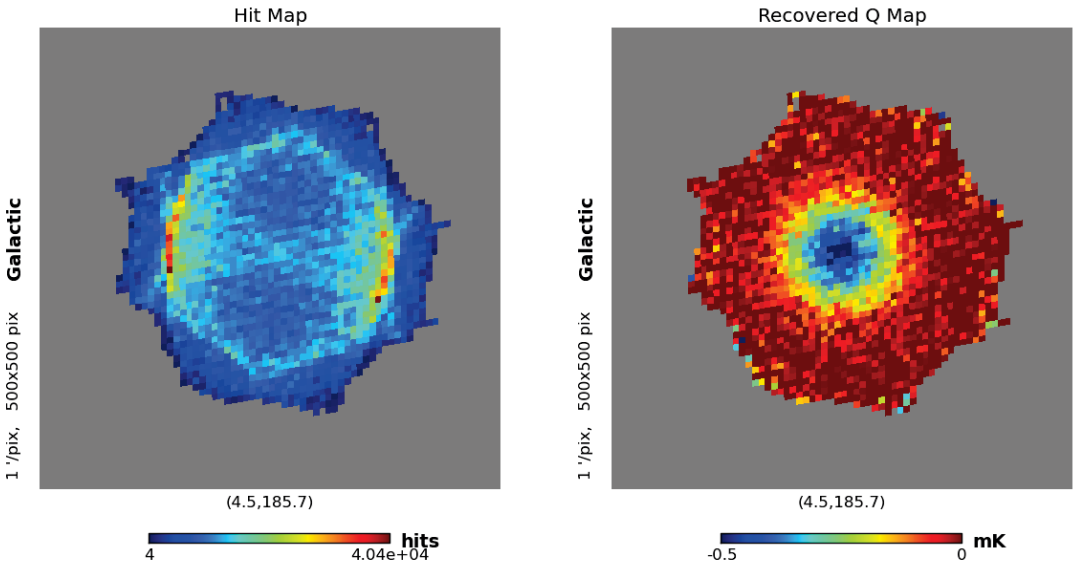


Figure 62: A hit map showing the number of times a pixel was sampled, and a reconstructed Q polarization map. This is the result of Lissajous wobble super imposed while tracking Tau A for 24 hours.

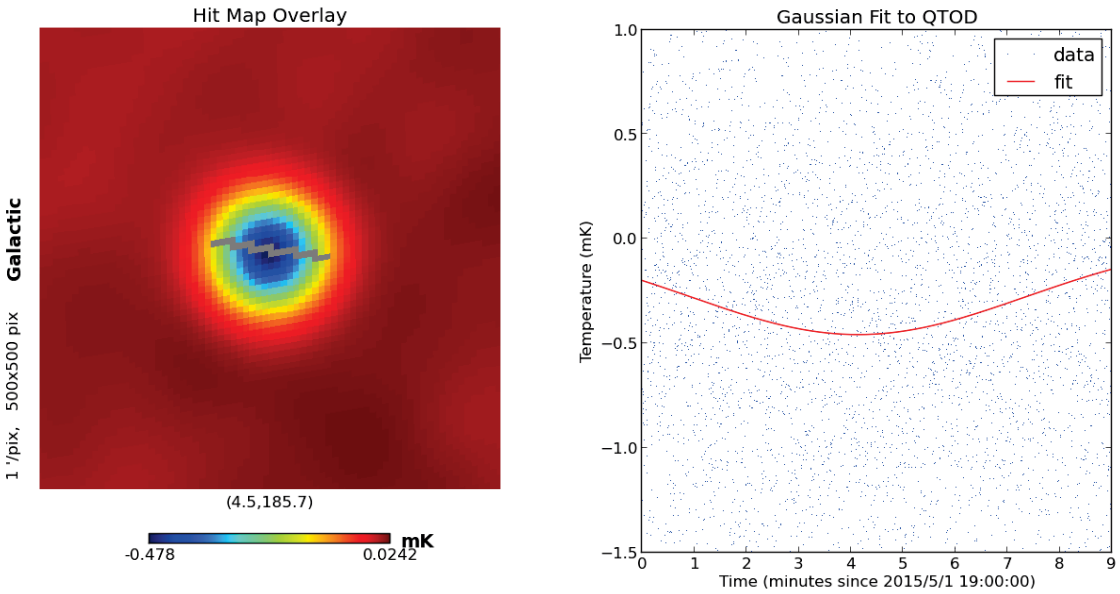


Figure 63: A hit map showing the pixels sampled is overlaid on smoothed WMAP data to visualize the drift scan.

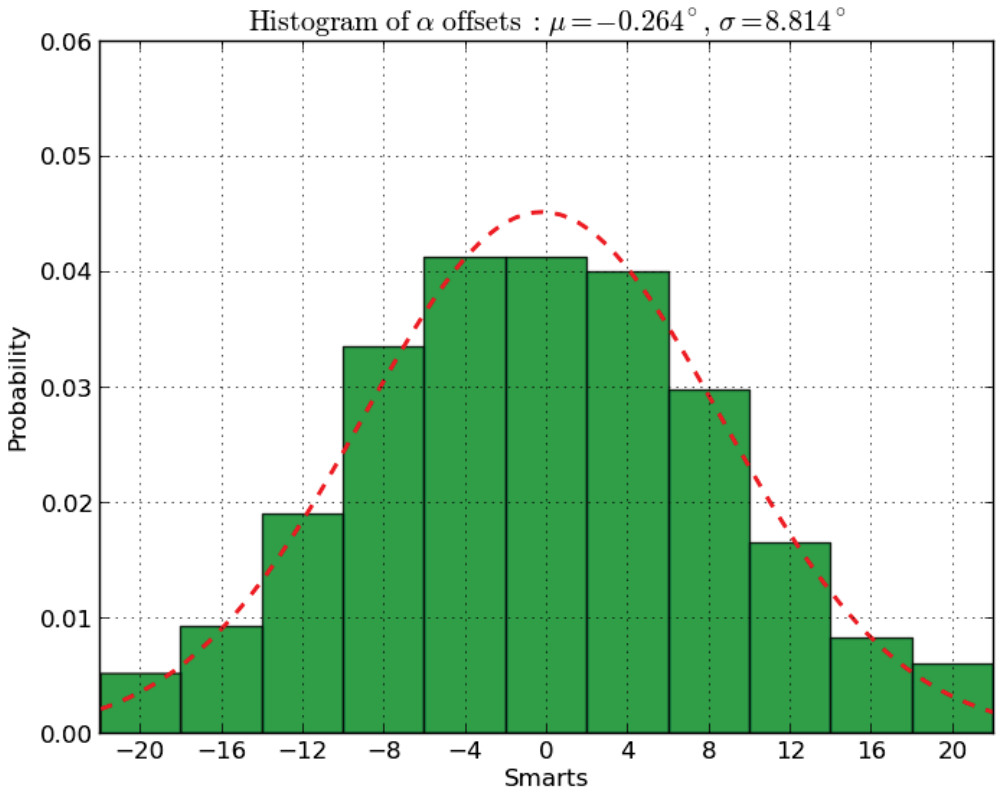


Figure 64: The Monte Carlo simulation with 1000 runs, holding $\beta = 0.15'$ and $\gamma = 0$ fixed resulted in an estimated standard error of $8.814^\circ$.

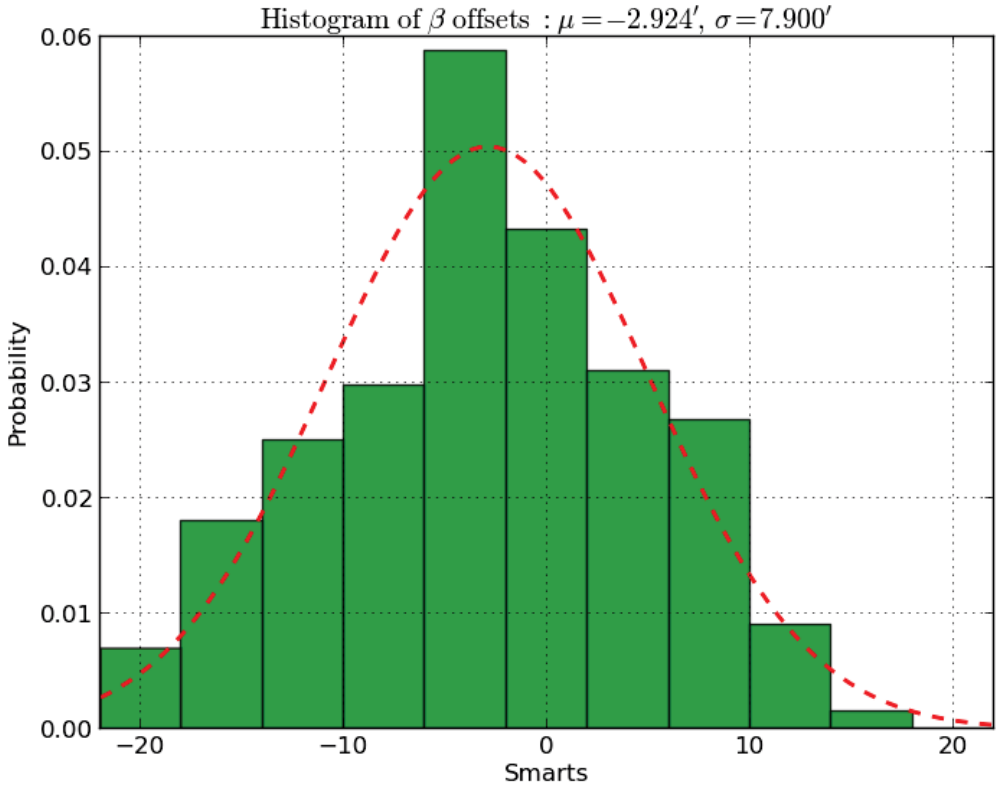


Figure 65: The Monte Carlo simulation with $1000$ runs, holding $\alpha = 0$ and $\gamma = 0$ fixed resulted in an estimated standard error of $7.9'$.

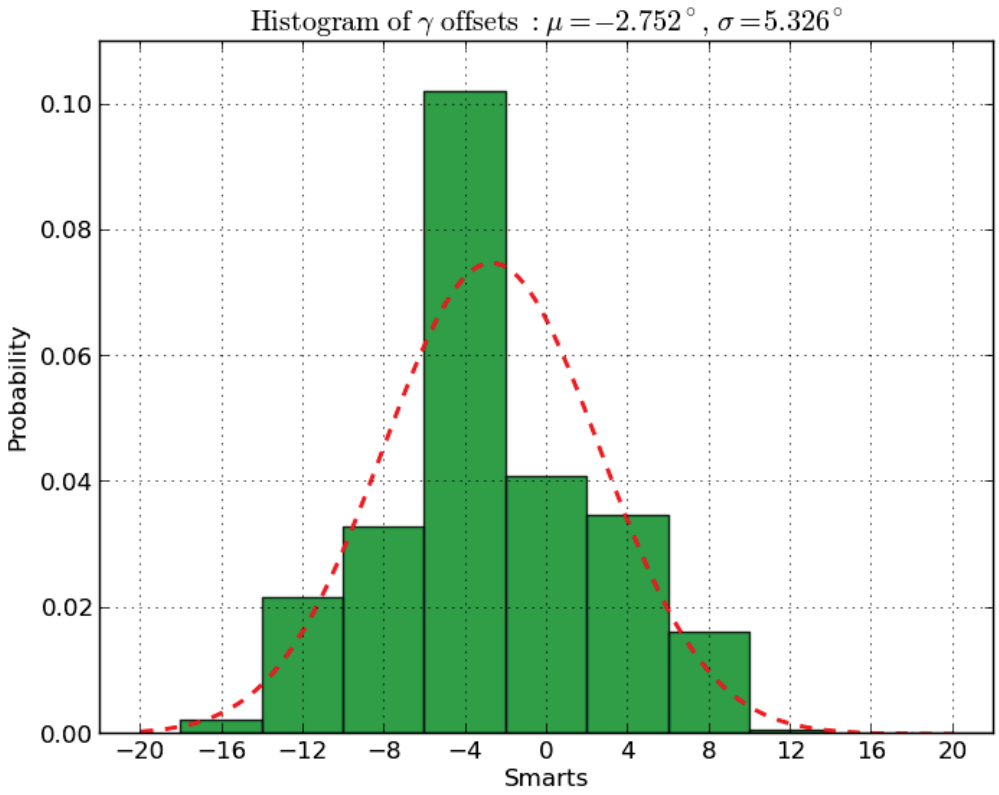


Figure 66: The Monte Carlo simulation with $1000$ runs, holding $\alpha = 0$ and $\gamma = 0$ fixed resulted in an estimated standard error of $5.326°$.

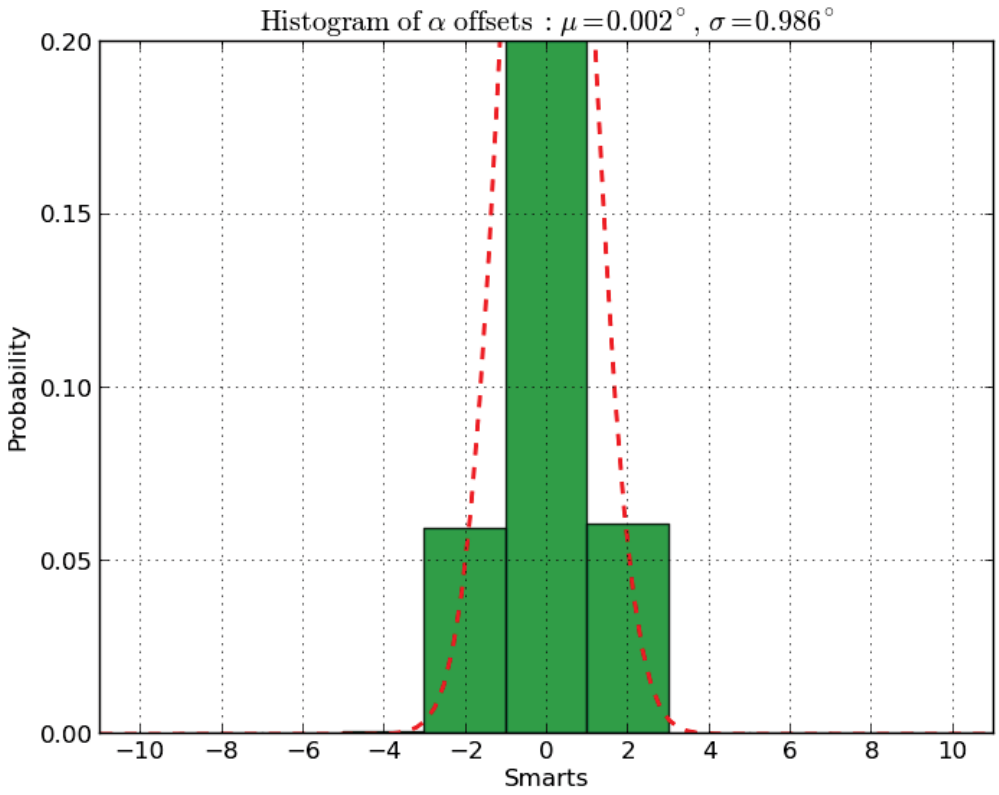


Figure 67: The Monte Carlo simulation with $1000$ runs, holding $\beta = .15'$ and $\gamma = 0$ fixed resulted in an estimated standard error of $8.814^\circ$.

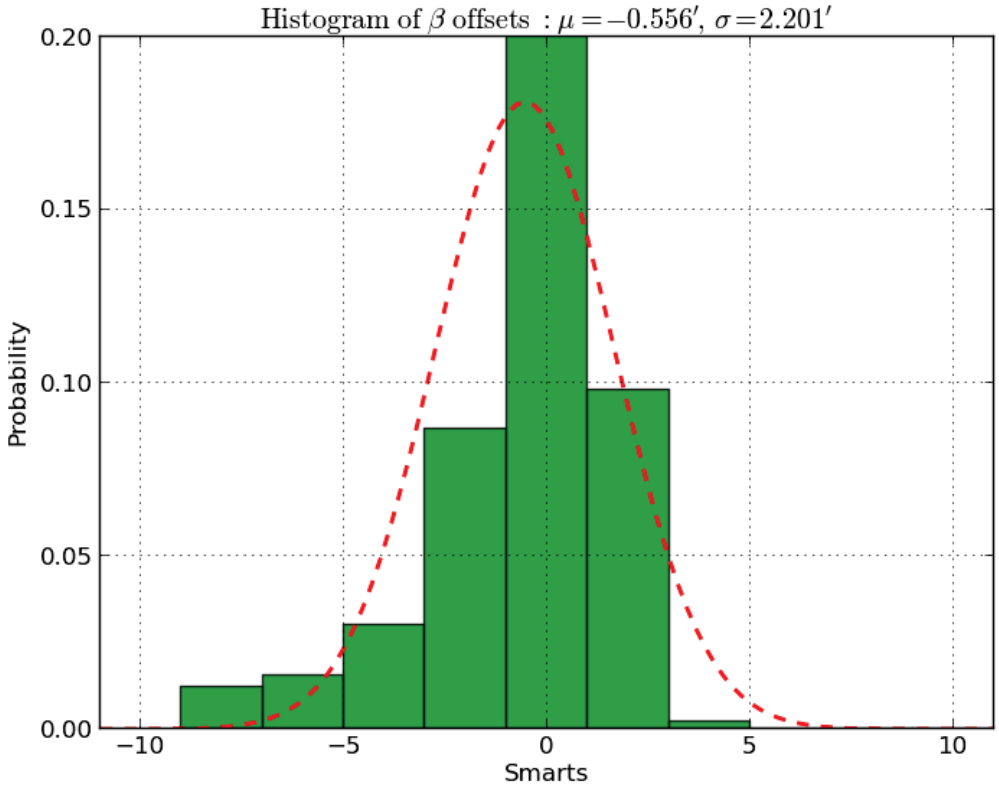


Figure 68: The Monte Carlo simulation with $1000$ runs, holding $\alpha = 0$ and $\gamma = 0$ fixed resulted in an estimated standard error of $7.9'$.

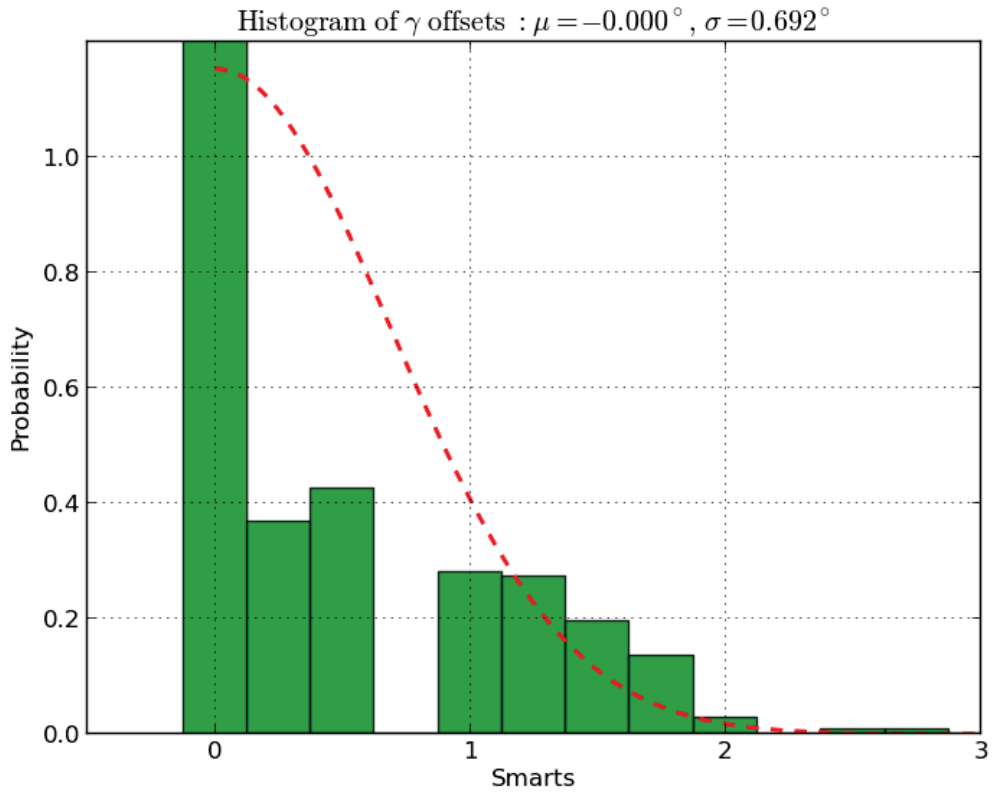


Figure 69: The Monte Carlo simulation with $1000$ runs, holding $\alpha = 0$ and $\gamma = 0$ fixed resulted in an estimated standard error of $5.326°$.

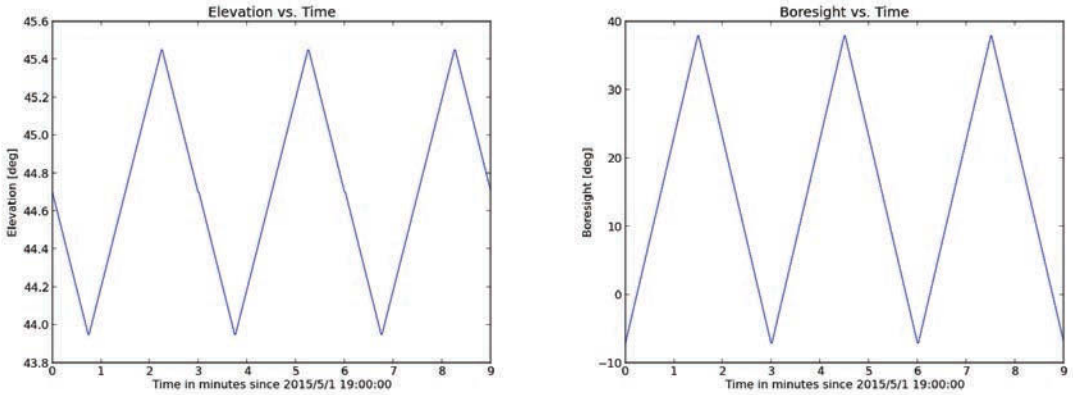


Figure 70: The left plot shows the elevation axis versus time. The right shows the Boresight axis versus time. This movement occurs as the source drifts through the line of sight.

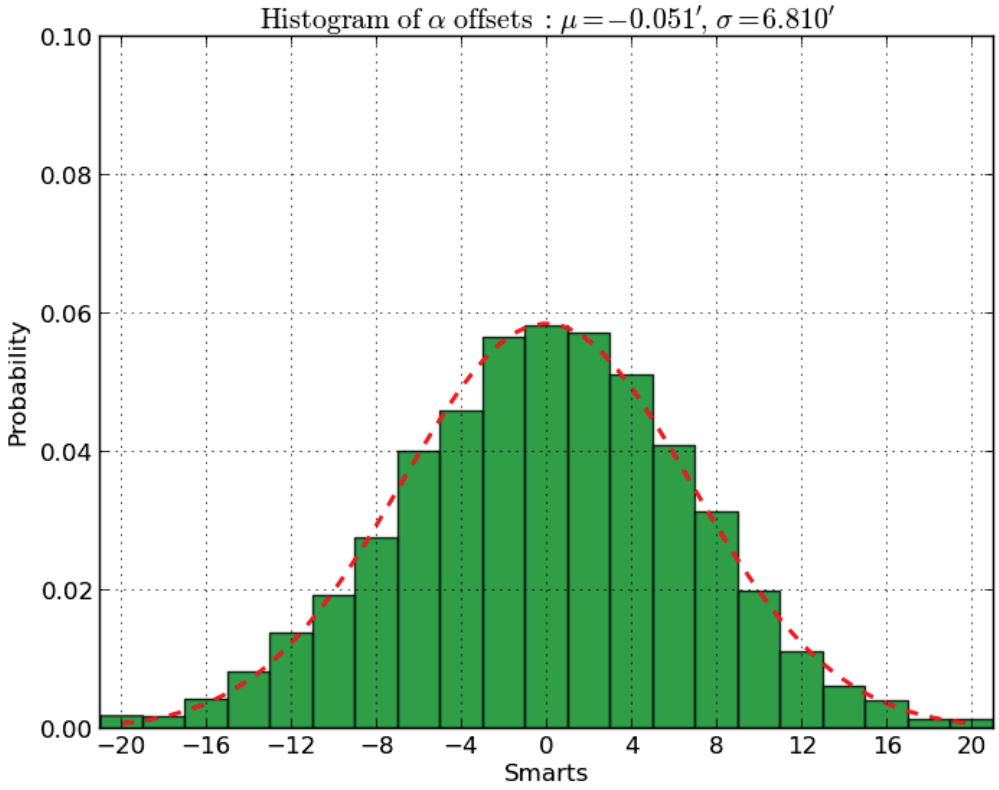


Figure 71: The Monte Carlo simulation with 10000 runs, holding $\beta = 0.30'$ and $\gamma = 0$ fixed resulted in an estimated standard error of $6.810°$.

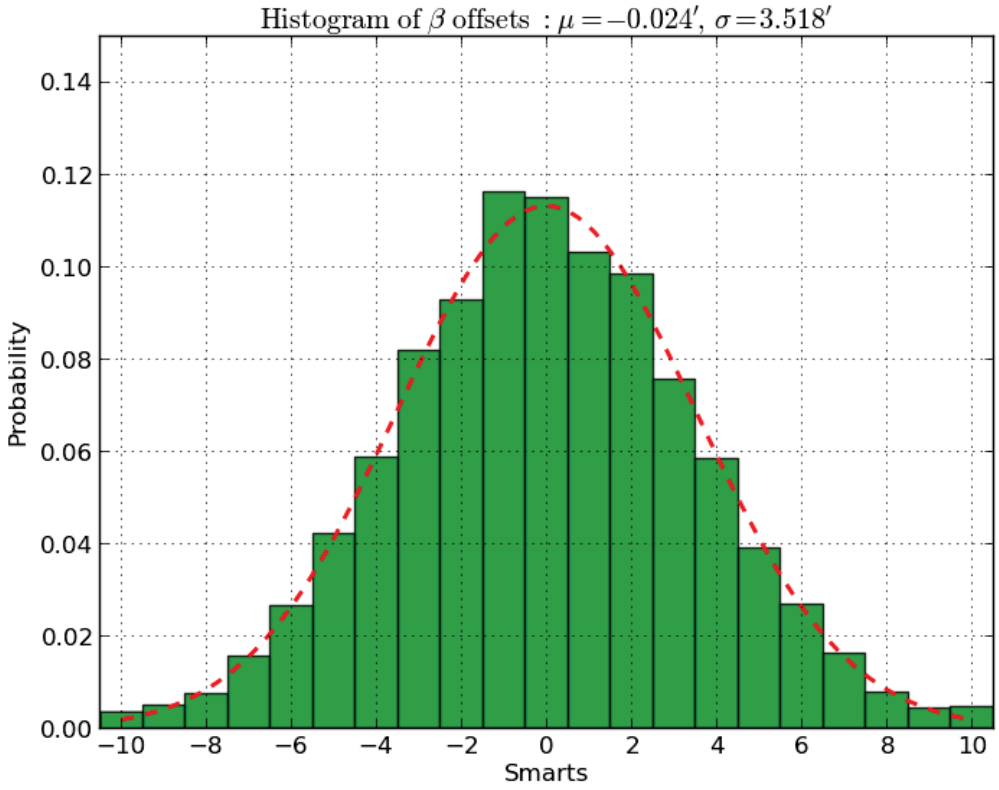


Figure 72: The Monte Carlo simulation with $1000$ runs, holding $\alpha = 0$ and $\gamma = 0$ fixed resulted in an estimated standard error of $7.9'$.

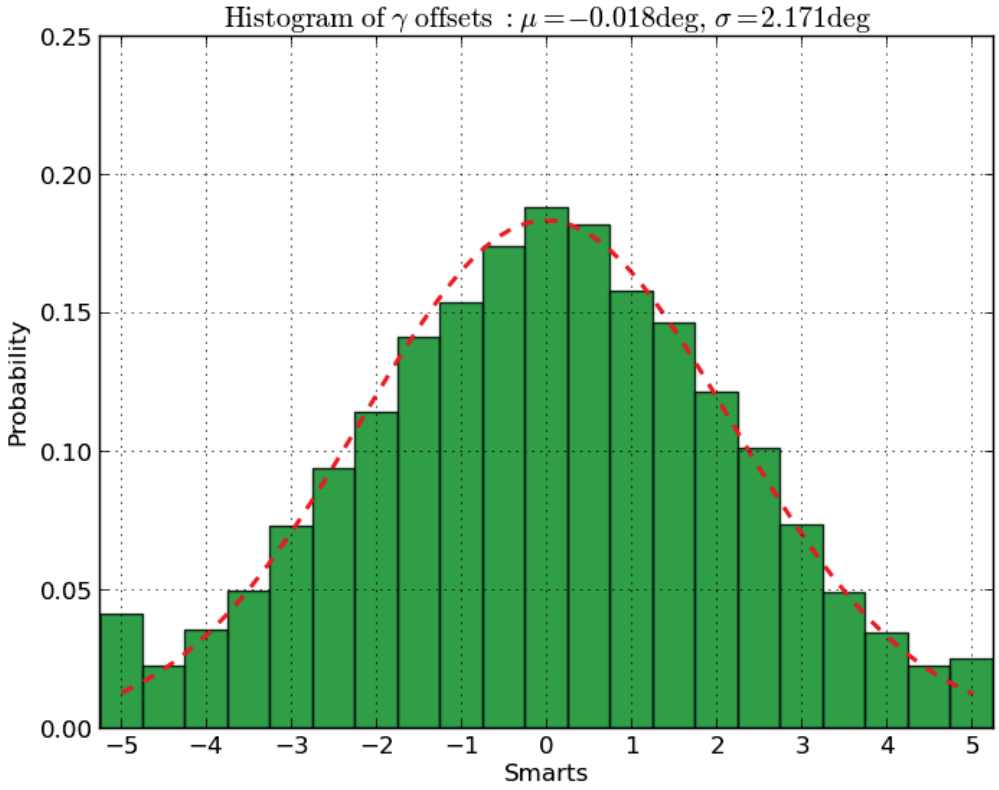


Figure 73: The Monte Carlo simulation with $1000$ runs, holding $\alpha = 0$ and $\gamma = 0$ fixed resulted in an estimated standard error of $40.232'$.

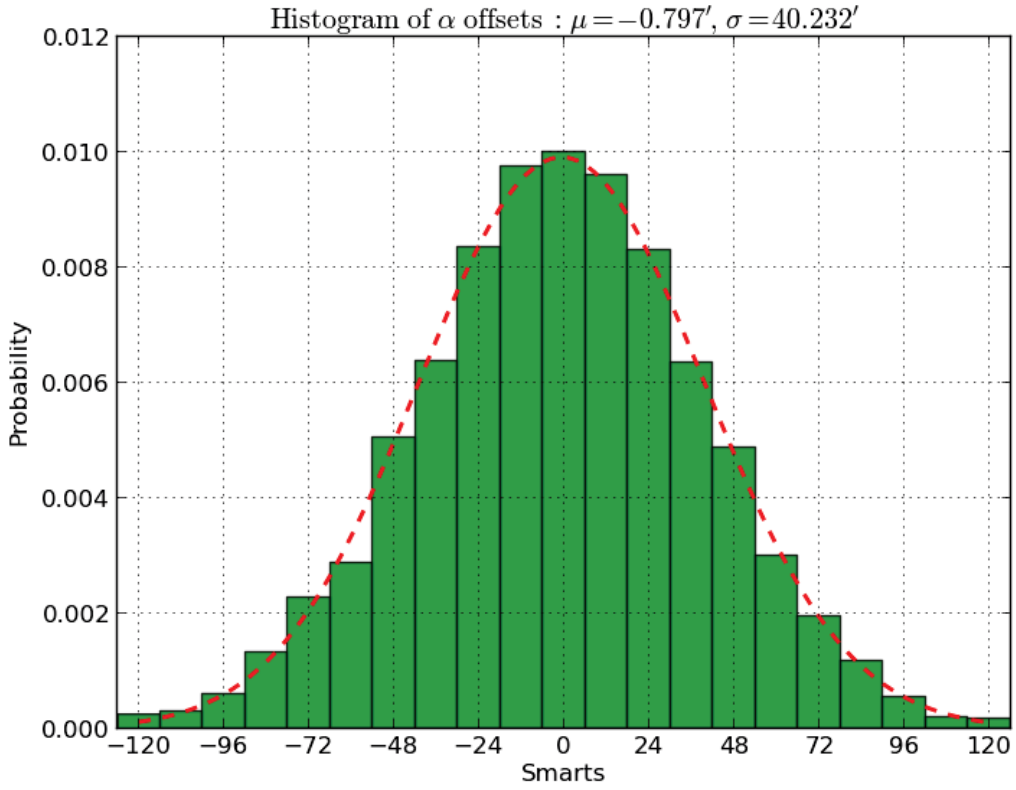


Figure 74: The Monte Carlo simulation with $10000$ runs, holding $\beta = .30'$ and $\gamma = 0$ fixed resulted in an estimated standard error of $20.894''$.

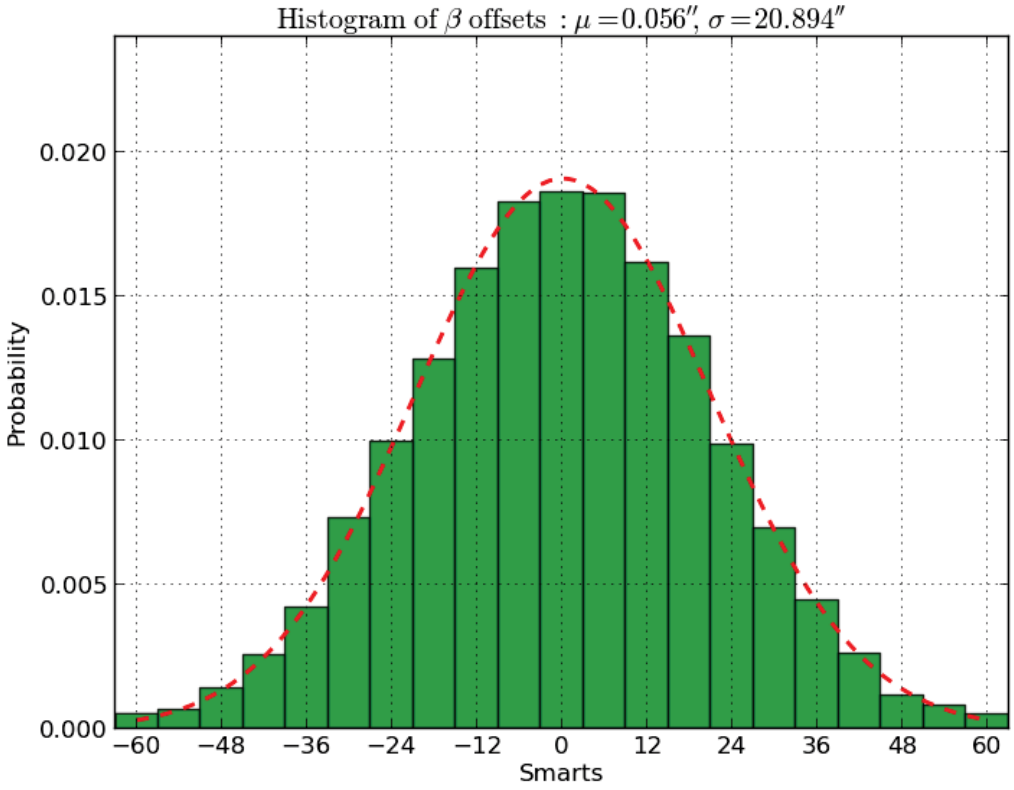


Figure 75: The Monte Carlo simulation with $10000$ runs, holding $\alpha = 0$ and $\gamma = 0$ fixed resulted in an estimated standard error of $7.9'$.

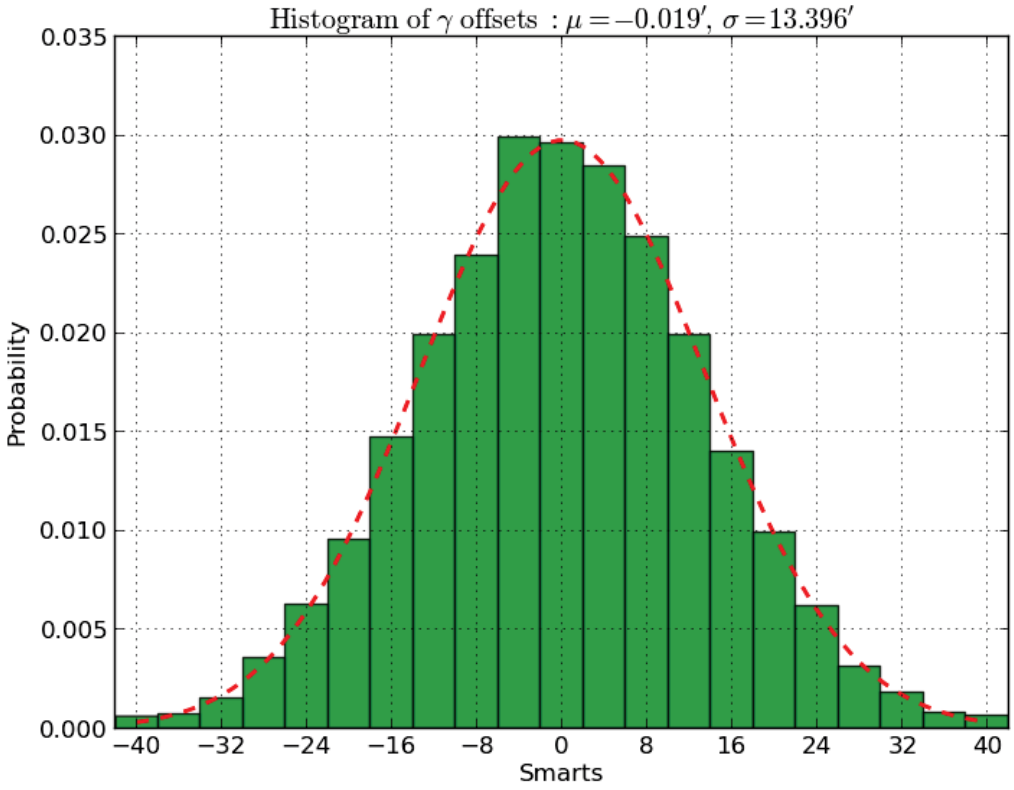


Figure 76: The Monte Carlo simulation with $10000$ runs, holding $\alpha = 0$ and $\gamma = 0$ fixed resulted in an estimated standard error of $13.396'$.

# References


[1] L. R. Abramo and T. S. Pereira. Testing Gaussianity, Homogeneity, and Isotropy with the Cosmic Microwave Background. *Advances in Astronomy*, 2010:70, 2010.

[2] V. Acquaviva, N. Bartolo, S. Matarrese, and A. Riotto. Gauge-invariant second-order perturbations and non-Gaussianity from inflation. *Nuclear Physics B*, 667:119–148, September 2003.

[3] R. Andrae, T. Schulze-Hartung, and P. Melchior. Dos and don'ts of reduced chi-squared. *ArXiv e-prints*, December 2010.

[4] J. W. Appel, A. Ali, M. Amiri, D. Araujo, C. L. Bennet, F. Boone, M. Chan, H.-M. Cho, D. T. Chuss, F. Colazo, E. Crowe, K. Denis, R. Dünner, J. Eimer, T. Essinger-Hileman, D. Gothe, M. Halpern, K. Harrington, G. Hilton, G. F. Hinshaw, C. Huang, K. Irwin, G. Jones, J. Karakula, A. J. Kogut, D. Larson, M. Limon, L. Lowry, T. Marriage, N. Mehrle, A. D. Miller, N. Miller, S. H. Moseley, G. Novak, C. Reintsema, K. Rostem, T. Stevenson, D. Towner, K. U-Yen, E. Wagner, D. Watts, E. Wollack, Z. Xu, and L. Zeng. The cosmology large angular scale surveyor (CLASS): 38-GHz detector array of bolometric polarimeters. In *Society of Photo-Optical Instrumentation Engineers (SPIE) Conference Series*, volume 9153 of *Society of Photo-Optical Instrumentation Engineers (SPIE) Conference Series*, page 1, July 2014.

[5] J. Aumont, L. Conversi, C. Thum, H. Wiesemeyer, E. Falgarone, J. F. Macías-Pérez, F. Piacentini, E. Pointecouteau, N. Ponthieu, J. L. Puget, C. Rosset, J. A. Tauber, and M. Tristram. Measurement of the Crab nebula polarization at 90 GHz as a calibrator for CMB experiments. *Astronomy and Astrophysics*, 514:A70, May 2010.

[6] B. A. Bassett and F. Viniegra. Massless metric preheating. *Physical Review D*, 62(4):043507, August 2000.

[7] D. Baumann, M. G. Jackson, P. Adshead, A. Amblard, A. Ashoorioon, N. Bartolo, R. Bean, M. Beltrán, F. de Bernardis, S. Bird, X. Chen, D. J. H. Chung, L. Colombo, A. Cooray, P. Creminelli, S. Dodelson, J. Dunkley, C. Dvorkin, R. Easther, F. Finelli, R. Flauger, M. P. Hertzberg, K. Jones-Smith, S. Kachru, K. Kadota, J. Khoury, W. H. Kinney, E. Komatsu, L. M. Krauss, J. Lesgourgues, A. Liddle, M. Liguori, E. Lim, A. Linde, S. Matarrese, H. Mathur, L. McAllister, A. Melchiorri, A. Nicolis, L. Pagano, H. V. Peiris, M. Peloso, L. Pogosian, E. Pierpaoli, A. Riotto, U. Seljak, L. Senatore, S. Shandera, E. Silverstein, T. Smith, P. Vaudrevange, L. Verde, B. Wandelt, D. Wands, S. Watson, M. Wyman, A. Yadav, W. Valkenburg, and M. Zaldarriaga. Probing Inflation with CMB Polarization. In S. Dodelson, D. Baumann, A. Cooray, J. Dunkley, A. Fraisse, M. G. Jackson, A. Kogut, L. Krauss, M. Zaldarriaga, and K. Smith, editors, *American Institute of Physics Conference Series*, volume 1141 of *American Institute of Physics Conference Series*, pages 10–120, June 2009.

[8] C. L. Bennett, D. Larson, J. L. Weiland, N. Jarosik, G. Hinshaw, N. Odegard, K. M.

Smith, R. S. Hill, B. Gold, M. Halpern, E. Komatsu, M. R. Nolta, L. Page, D. N. Spergel, E. Wollack, J. Dunkley, A. Kogut, M. Limon, S. S. Meyer, G. S. Tucker, and E. L. Wright. Nine-year Wilkinson Microwave Anisotropy Probe (WMAP) Observations: Final Maps and Results. *Astrophysical Journal*, 208:20, October 2013.

[9] A. Bernui and W. S. Hipólito-Ricaldi. Can a primordial magnetic field originate large-scale anomalies in WMAP data? *Monthly Notices of the Royal Astronomical Society*, 389:1453–1460, September 2008.

[10] E. Bertschinger. Cosmological Perturbation Theory and Structure Formation. *ArXiv Astrophysics e-prints*, December 2001.

[11] BICEP2/Keck, Planck Collaborations, :, P. A. R. Ade, N. Aghanim, Z. Ahmed, R. W. Aikin, K. D. Alexander, M. Arnaud, J. Aumont, and et al. A Joint Analysis of BICEP2/Keck Array and Planck Data. *ArXiv e-prints*, February 2015.

[12] N. D. Birrell and P. C. W. Davies. *Quantum fields in curved space*. 1982.

[13] C. Bischoff, L. Hyatt, J. J. McMahon, G. W. Nixon, D. Samtleben, K. M. Smith, K. Vanderlinde, D. Barkats, P. Farese, T. Gaier, J. O. Gundersen, M. M. Hedman, S. T. Staggs, B. Winstein, and CAPMAP Collaboration. New Measurements of Fine-Scale CMB Polarization Power Spectra from CAPMAP at Both 40 and 90 GHz. *The Astrophysical Journal*, 684:771–789, September 2008.

[14] J. R. Bond and G. Efstathiou. Cosmic background radiation anisotropies in universes dominated by nonbaryonic dark matter. *Astrophysical Journal Letters*, 285:L45–L48, October 1984.

[15] L. A. Boyle, P. J. Steinhardt, and N. Turok. Inflationary Predictions for Scalar and Tensor Fluctuations Reconsidered. *Physical Review Letters*, 96(11):111301, March 2006.

[16] R. H. Brandenberger. Lectures on the Theory of Cosmological Perturbations. In N. Bretón, J. L. Cervantes-Cota, and M. Salgad, editors, *The Early Universe and Observational Cosmology*, volume 646 of *Lecture Notes in Physics, Berlin Springer Verlag*, pages 127–167, 2004.

[17] M. L. Brown, P. Ade, J. Bock, M. Bowden, G. Cahill, P. G. Castro, S. Church, T. Culverhouse, R. B. Friedman, K. Ganga, W. K. Gear, S. Gupta, J. Hinderks, J. Kovac, A. E. Lange, E. Leitch, S. J. Melhuish, Y. Memari, J. A. Murphy, A. Orlando, C. O'Sullivan, L. Piccirillo, C. Pryke, N. Rajguru, B. Rusholme, R. Schwarz, A. N. Taylor, K. L. Thompson, A. H. Turner, E. Y. S. Wu, M. Zemcov, and QUa D Collaboration. Improved Measurements of the Temperature and Polarization of the Cosmic Microwave Background from QUaD. *The Astrophysical Journal*, 705:978–999, November 2009.

[18] L. Campanelli, P. Cea, and L. Tedesco. Cosmic microwave background quadrupole and ellipsoidal universe. *Physical Review D*, 76(6):063007, September 2007.

[19] Sean Carroll. *Spacetime and geometry : an introduction to general relativity*. Addison Wesley, San Francisco, 2004.

[20] S Chandrasekhar. *Radiative transfer*. Dover Publications, New York, 1960.

[21] D. T. Chuss, E. J. Wollack, R. Henry, H. Hui, A. J. Juarez, M. Krejny, S. H. Moseley, and G. Novak. Properties of a variable-delay polarization modulator. *Applied Optics*, 51:197, January 2012.

[22] D. T. Chuss, E. J. Wollack, S. H. Moseley, and G. Novak. Interferometric polarization control. *Applied Optics*, 45:5107–5117, July 2006.

[23] J. T. Dempsey, P. Friberg, T. Jenness, D. Bintley, and W. S. Holland. Extinction correction and on-sky calibration of SCUBA-2. In *Society of Photo-Optical Instrumentation Engineers (SPIE) Conference Series*, volume 7741 of *Society of Photo-Optical Instrumentation Engineers (SPIE) Conference Series*, page 1, July 2010.

[24] Scott Dodelson. *Modern cosmology*. Academic Press, An Imprint of Elsevier, San Diego, California, 2003.

[25] A. D. Dolgov. Breaking of conformal invariance and electromagnetic field generation in the Universe. *Physical Review D*, 48:2499–2501, September 1993.

[26] J. R. Eimer, C. L. Bennett, D. T. Chuss, T. Marriage, E. J. Wollack, and L. Zeng. The cosmology large angular scale surveyor (CLASS): 40 GHz optical design. In

*Society of Photo-Optical Instrumentation Engineers (SPIE) Conference Series*, volume 8452 of *Society of Photo-Optical Instrumentation Engineers (SPIE) Conference Series*, page 20, September 2012.

[27] D. J. Eisenstein and C. L. Bennett. Cosmic sound waves rule. *Physics Today*, 61(4):44, 2008.

[28] Johanna Erdmenger. *String cosmology modern string theory concepts from the big bang to cosmic structure*. Wiley-VCH, Weinheim, 2009.

[29] A. L. Erickcek, M. Kamionkowski, and S. M. Carroll. A hemispherical power asymmetry from inflation. *Physical Review D*, 78(12):123520, December 2008.

[30] T. Essinger-Hileman, A. Ali, M. Amiri, J. W. Appel, D. Araujo, C. L. Bennett, F. Boone, M. Chan, H.-M. Cho, D. T. Chuss, F. Colazo, E. Crowe, K. Denis, R. Dünner, J. Eimer, D. Gothe, M. Halpern, K. Harrington, G. C. Hilton, G. F. Hinshaw, C. Huang, K. Irwin, G. Jones, J. Karakla, A. J. Kogut, D. Larson, M. Limon, L. Lowry, T. Marriage, N. Mehrle, A. D. Miller, N. Miller, S. H. Moseley, G. Novak, C. Reintsema, K. Rostem, T. Stevenson, D. Towner, K. U-Yen, E. Wagner, D. Watts, E. J. Wollack, Z. Xu, and L. Zeng. CLASS: the cosmology large angular scale surveyor. In *Society of Photo-Optical Instrumentation Engineers (SPIE) Conference Series*, volume 9153 of *Society of Photo-Optical Instrumentation Engineers (SPIE) Conference Series*, page 1, July 2014.

[31] G. Fabbian, S. Spinelli, M. Gervasi, A. Tartari, and M. Zannoni. A template of atmospheric molecular oxygen circularly polarized emission for CMB experiments. *ArXiv e-prints*, June 2012.

[32] V. L. Ginzburg and S. I. Syrovatskii. Cosmic Magnetobremsstrahlung (synchrotron Radiation). *Annual Review of Astronomy and Astrophysics*, 3:297, 1965.

[33] V. L. Ginzburg and S. I. Syrovatskii. Developments in the Theory of Synchrotron Radiation and its Reabsorption. *Annual Review of Astronomy and Astrophysics*, 7:375, 1969.

[34] C. Gordon, W. Hu, D. Huterer, and T. Crawford. Spontaneous isotropy breaking: A mechanism for CMB multipole alignments. *Physical Review D*, 72(10):103002, November 2005.

[35] A. H. Guth. Inflationary universe: A possible solution to the horizon and flatness problems. *Physical Review D*, 23:347–356, January 1981.

[36] A. H. Guth and S.-Y. Pi. Fluctuations in the new inflationary universe. *Physical Review Letters*, 49:1110–1113, October 1982.

[37] S. Hanany and P. Rosenkranz. Polarization of the atmosphere as a foreground for cosmic microwave background polarization experiments. *New Astronomy Reviews*, 47:1159–1165, December 2003.

[38] A. Heavens, R. Jimenez, and L. Verde. Standard Rulers, Candles, and Clocks from the Low-Redshift Universe. *Physical Review Letters*, 113(24):241302, December 2014.

[39] W. Hu. CMB Anisotropies: A Decadal Survey. In K. Sato and M. Kawasaki, editors, *Birth and Evolution of the Universe*, page 131, 2001.

[40] W. Hu. CMB temperature and polarization anisotropy fundamentals. *Annals of Physics*, 303:203–225, January 2003.

[41] W. Hu. Lecture Notes on CMB Theory: From Nucleosynthesis to Recombination. *ArXiv e-prints*, February 2008.

[42] W. Hu and M. White. A CMB polarization primer. *New Astronomy*, 2:323–344, October 1997.

[43] E. Hubble. A Relation between Distance and Radial Velocity among Extra-Galactic Nebulae. *Proceedings of the National Academy of Science*, 15:168–173, March 1929.

[44] K. Ichiki. CMB foreground: A concise review. *Progress of Theoretical and Experimental Physics*, 2014(6):060000, June 2014.

[45] Theophilus Britt Griswold Joe Sugarman, Will Kirk. In a class by itself. http://krieger.jhu.edu/magazine/v11n2/a-class-by-itself/, mar 2014.

[46] T. Kahniashvili, G. Lavrelashvili, and B. Ratra. CMB temperature anisotropy from broken spatial isotropy due to a homogeneous cosmological magnetic field. *Physical Review D*, 78(6):063012, September 2008.

[47] M. Kamionkowski, A. Kosowsky, and A. Stebbins. Statistics of cosmic microwave background polarization. *Physical Review D*, 55:7368–7388, June 1997.

[48] C. Kiefer, I. Lohmar, D. Polarski, and A. A. Starobinsky. Pointer states for primordial fluctuations in inflationary cosmology. *Classical and Quantum Gravity*, 24:1699–1718, April 2007.

[49] L. M. Krauss, S. Dodelson, and S. Meyer. Primordial Gravitational Waves and Cosmology. *Science*, 328:989–, May 2010.

[50] A. Lazarian. Understanding Polarized Foreground from Dust: Towards Reliable Measurements of CMB Polarization. In *astro2010: The Astronomy and Astrophysics Decadal Survey*, volume 2010 of *Astronomy*, page 174, 2009.

[51] S. M. Leach and A. R. Liddle. Constraining slow-roll inflation with WMAP and 2dF. *Physical Review D*, 68(12):123508, December 2003.

[52] S. M. Leach and A. R. Liddle. Microwave background constraints on inflationary parameters. *Monthly Notice of the Royal Astronomical Society*, 341:1151–1156, June 2003.

[53] E. M. Leitch, J. M. Kovac, N. W. Halverson, J. E. Carlstrom, C. Pryke, and M. W. E. Smith. Degree Angular Scale Interferometer 3 Year Cosmic Microwave Background Polarization Results. *The Astrophysical Journal*, 624:10–20, May 2005.

[54] G. Lemaître. Un Univers homogène de masse constante et de rayon croissant rendant compte de la vitesse radiale des nébuleuses extra-galactiques. *Annales de la Société Scientifique de Bruxelles*, 47:49–59, 1927.

[55] J. Lesgourgues, A. A. Starobinsky, and W. Valkenburg. What do WMAP and SDSS really tell us about inflation? *Journal of Cosmology and Astroparticle Physics*, 1:10, January 2008.

[56] A. R. Liddle and D. H. Lyth. COBE, gravitational waves, inflation and extended inflation. *Physics Letters B*, 291:391–398, October 1992.

[57] E. M. Lifshitz. On the gravitational stability of the expanding universe. *Zhurnal Eksperimentalnoi i Teoreticheskoi Fiziki*, 16:587–602, 1946.

[58] A. Linde. Inflationary Cosmology after Planck 2013. *ArXiv e-prints*, February 2014.

[59] J. Maldacena. Non-gaussian features of primordial fluctuations in single field inflationary models. *Journal of High Energy Physics*, 5:13, May 2003.

[60] P. Martineau. On the decoherence of primordial fluctuations during inflation. *Classical and Quantum Gravity*, 24:5817–5834, December 2007.

[61] J. C. Mather, E. S. Cheng, D. A. Cottingham, R. E. Eplee, Jr., D. J. Fixsen, T. Hewagama, R. B. Isaacman, K. A. Jensen, S. S. Meyer, P. D. Noerdlinger, S. M. Read, L. P. Rosen, R. A. Shafer, E. L. Wright, C. L. Bennett, N. W. Boggess, M. G. Hauser, T. Kelsall, S. H. Moseley, Jr., R. F. Silverberg, G. F. Smoot, R. Weiss, and

D. T. Wilkinson. Measurement of the cosmic microwave background spectrum by the COBE FIRAS instrument. *Astrophysical Journal*, 420:439–444, January 1994.

[62] T. E. Montroy, P. A. R. Ade, J. J. Bock, J. R. Bond, J. Borrill, A. Boscaleri, P. Cabella, C. R. Contaldi, B. P. Crill, P. de Bernardis, G. De Gasperis, A. de Oliveira-Costa, G. De Troia, G. di Stefano, E. Hivon, A. H. Jaffe, T. S. Kisner, W. C. Jones, A. E. Lange, S. Masi, P. D. Mauskopf, C. J. MacTavish, A. Melchiorri, P. Natoli, C. B. Netterfield, E. Pascale, F. Piacentini, D. Pogosyan, G. Polenta, S. Prunet, S. Ricciardi, G. Romeo, J. E. Ruhl, P. Santini, M. Tegmark, M. Veneziani, and N. Vittorio. A Measurement of the CMB EE Spectrum from the 2003 Flight of BOOMERANG. *The Astrophysical Journal*, 647:813–822, August 2006.

[63] V. F. Mukhanov. *Physical foundations of cosmology*. Cambridge University Press, Cambridge, UK New York, 2005.

[64] V. F. Mukhanov, H. A. Feldman, and R. H. Brandenberger. Theory of cosmological perturbations. *Physics Reports*, 215:203–333, June 1992.

[65] H. V. Peiris and R. Easther. Recovering the inflationary potential and primordial power spectrum with a slow roll prior: methodology and application to WMAP three year data. *Journal of Cosmology and Astroparticle Physics*, 7:2, July 2006.

[66] A. A. Penzias and R. W. Wilson. A Measurement of Excess Antenna Temperature at 4080 Mc/s. *Astrophysical Journal*, 142:419–421, July 1965.

[67] Planck Collaboration, R. Adam, P. A. R. Ade, N. Aghanim, Y. Akrami, M. I. R. Alves, M. Arnaud, F. Arroja, J. Aumont, C. Baccigalupi, and et al. Planck 2015 results. I. Overview of products and scientific results. *ArXiv e-prints*, February 2015.

[68] Planck Collaboration, R. Adam, P. A. R. Ade, N. Aghanim, Y. Akrami, M. I. R. Alves, M. Arnaud, F. Arroja, J. Aumont, C. Baccigalupi, and et al. Planck 2015 results. I. Overview of products and scientific results. *ArXiv e-prints*, February 2015.

[69] Planck Collaboration, P. A. R. Ade, N. Aghanim, M. I. R. Alves, C. Armitage-Caplan, M. Arnaud, M. Ashdown, F. Atrio-Barandela, J. Aumont, H. Aussel, and et al. Planck 2013 results. I. Overview of products and scientific results. *Astronomy and Astrophysics*, 571:A1, November 2014.

[70] Planck Collaboration, P. A. R. Ade, N. Aghanim, M. Arnaud, F. Arroja, M. Ashdown, J. Aumont, C. Baccigalupi, M. Ballardini, A. J. Banday, and et al. Planck 2015 results. XVII. Constraints on primordial non-Gaussianity. *ArXiv e-prints*, February 2015.

[71] QUIET Collaboration, C. Bischoff, A. Brizius, I. Buder, Y. Chinone, K. Cleary, R. N. Dumoulin, A. Kusaka, R. Monsalve, S. K. Næss, L. B. Newburgh, R. Reeves, K. M. Smith, I. K. Wehus, J. A. Zuntz, J. T. L. Zwart, L. Bronfman, R. Bustos, S. E. Church, C. Dickinson, H. K. Eriksen, P. G. Ferreira, T. Gaier, J. O. Gundersen, M. Hasegawa, M. Hazumi, K. M. Huffenberger, M. E. Jones, P. Kangaslahti, D. J. Kapner, C. R. Lawrence, M. Limon, J. May, J. J. McMahon, A. D. Miller, H. Nguyen, G. W. Nixon, T. J. Pearson, L. Piccirillo, S. J. E. Radford, A. C. S. Readhead, J. L. Richards,

D. Samtleben, M. Seiffert, M. C. Shepherd, S. T. Staggs, O. Tajima, K. L. Thompson, K. Vanderlinde, R. Williamson, and B. Winstein. First Season QUIET Observations: Measurements of Cosmic Microwave Background Polarization Power Spectra at 43 GHz in the Multipole Range. *The Astrophysical Journal*, 741:111, November 2011.

[72] B. Ratra. Cosmological 'seed' magnetic field from inflation. *Astrophysical Journal Letters*, 391:L1–L4, May 1992.

[73] Barbara Ryden. *Introduction to cosmology*. Addison-Wesley, San Francisco, 2003.

[74] D. T. Son. Classical Preheating and Decoherence. *ArXiv High Energy Physics - Phenomenology e-prints*, January 1996.

[75] S. Spinelli, G. Fabbian, A. Tartari, M. Zannoni, and M. Gervasi. A template of atmospheric $O_2$ circularly polarized emission for cosmic microwave background experiments. *Monthly Notices of the Royal Astronomical Society*, 414:3272–3280, July 2011.

[76] A. A. Starobinskiĭ. Spectrum of relict gravitational radiation and the early state of the universe. *Soviet Journal of Experimental and Theoretical Physics Letters*, 30:682, December 1979.

[77] M. S. Turner, M. White, and J. E. Lidsey. Tensor perturbations in inflationary models as a probe of cosmology. *Physical Review D*, 48:4613–4622, November 1993.

[78] Steven Weinberg. *Cosmology*. Oxford University Press, Oxford New York, 2008.

[79] K. C. Westfold. The Polarization of Synchrotron Radiation. *Astrophysical Journal*, 130:241, July 1959.

[80] M. White and W. Hu. The Sachs-Wolfe effect. *Astronomy and Astrophysics*, 321:8–9, May 1997.

[81] A. P. S. Yadav and B. D. Wandelt. Primordial Non-Gaussianity in the Cosmic Microwave Background. *Advances in Astronomy*, 2010:71, 2010.

[82] L. Zeng, C. L. Bennett, D. T. Chuss, and E. J. Wollack. A wide-band smooth-walled feedhorn with low cross polarization for millimeter astronomy. In *Society of Photo-Optical Instrumentation Engineers (SPIE) Conference Series*, volume 7741 of *Society of Photo-Optical Instrumentation Engineers (SPIE) Conference Series*, page 29, July 2010.

## Biographical Statement

Dominik Gothe began his PhD studies at the Johns Hopkins Henry A. Rowland Department of Physics & Astronomy in the fall semester of 2010. His course work was consistent with the requirements for a degree in physics while taking additional astronomy classes. He completed his program under Prof. Bennett and focused his research on instrumentation.